UNIVERSITÀ DEGLI STUDI DI MILANO
FACOLTÀ DI SCIENZE E TECNOLOGIE

Scuola di Dottorato in Fisica, Astrofisica e Fisica Applicata
Dipartimento di Fisica

Corso di Dottorato in Fisica, Astrofisica e Fisica Applicata
Ciclo XXVI

Fabrication and characterization of nanocomposite-based elastomeric optical devices

Settore Scientifico Disciplinare FIS/03

Supervisor: Professor Paolo MILANI

Coordinator: Professor Marco BERSANELLI

PhD Candidate:
Cristian Ghisleri

Academic Year 2013/2014

Commission of the final examination:

External Referee:
Herbert Shea

External Member:
Giovanni Mattei

Internal Member:
Paolo Milani

Final examination:

21 January 2014

Università degli Studi di Milano, Dipartimento di Fisica, Milano, Italy

To my parents, to Gabriele

MIUR subjects:

FIS/03

PACS:

78.67.Sc
42.79.-e
78.67.Bf

Contents

Introduction vii

I Deformable optical devices and nanocomposites 1

1 Adaptive and Tunable Optics 3
- 1.1 Deformable optical devices for adaptive and tunable optics 5
  - 1.1.1 Deformable mirros 5
  - 1.1.2 Tunable gratings 6
- 1.2 Applications of Adaptive Optics 7
  - 1.2.1 Astronomy 8
  - 1.2.2 Ophthalmology 9
  - 1.2.3 Microscopy 10
  - 1.2.4 Photonics 11

2 Nanocomposite-based elastomeric optics 13
- 2.1 Elastomeric optics 13
  - 2.1.1 Transparent elastomeric optics 13
  - 2.1.2 Reflective elastomeric optics 14
- 2.2 Requirements for reflective elastomeric optics 15
  - 2.2.1 Reflectivity 15
  - 2.2.2 Surface morphology 16
- 2.3 Resilience and stretchability 17
- 2.4 Metallization of elastomeric optical devices 19
  - 2.4.1 Liquid metals 19
  - 2.4.2 Physical Vapor Deposition 20
- 2.5 Metal-elastomer nanocomposites 22
  - 2.5.1 Chemical synthesis of nanocomposites 23
  - 2.5.2 Ion Implantation 24
  - 2.5.3 Supersonic Cluster Beam Implantation (SCBI) 26

3 Supersonic Cluster Beam Implanted nanocomposites **27**
3.1 Supersonic Cluster Beam Deposition (SCBD) and SCBI 27
3.2 Working principle of Supersonic Cluster Beam Implantation 28
3.2.1 Supersonic Expansion 28
3.2.2 Implantation in soft polymers 30
3.2.3 Equivalent thickness and filler volume fraction 31
3.2.4 Molecular dynamics simulations of SCBI in PDMS 32
3.3 Supersonic Cluster Beam Implantation setup 33
3.3.1 Pulsed Microplasma Cluster Source (PMCS) 35
3.4.1 Size distribution of metal nanoparticles 37
3.4 Morphological and mechanical characterization of SCBI Ag/PDMS nanocomposites 37
3.4.2 Penetration depth of metal nanoparticles 37
3.4.3 Elasticity of SCBI nanocomposites 38
3.4.4 Surface roughness 39

II Reflective stretchable optics **57**

4 Fabrication and characterization of elastomeric optical devices **59**
4.1 Fabrication of the devices 59
4.2 Morphological characterization 59
4.3 Optical properties 60
4.3.1 Reflectance 60
4.3.2 Spot size and linearity 61
4.4 Focusing properties 62

5 A simple scanning spectrometer based on a stretchable reflective grating **71**
5.1 Grating fabrication 71
5.2 Optical setup 72
5.3 Calibration 73
5.4 Spectra acquisition 73

III Plasmonics **77**

6 Surface Plasmon Resonance (SPR) **79**
6.1 Theoretical models 80
6.1.1 Drude model 80
6.1.2 Mie theory 84
6.1.3 Maxwell-Garnett theory 86
6.1.4 Shell-core model 88
6.2 Bergman model 91

7 SPR in SCBI metal-polymer nanocomosites **95**
7.1 Absorption with different equivalent thicknesses 95
7.2 Time evolution of the nanocomposite at RT 98
7.3 Thermal annealing 99
7.4 Effect of passivation on SPR 102
7.5 Stretching measurements 103

Conclusions and perspectives **108**

Bibliography **109**

List of Publications **122**

Introduction

Motivation

Adaptive and tunable optics, consisting in the correction of perturbed light wavefronts by means of deformable optical devices, was first introduced in the 50's by Babcock [1] and developed in the 70's by Buffington [2, 3] and Hardy [4] independentely. Nowadays it represents a well established technology mainly exploited in astronomy in order to reduce the effects of atmospheric perturbations limiting the attainable resolution of large astrophysical telescopes [5]. Adaptive and tunable optics is exploited in ophthalmology, microscopy and photonics as well for the improvement of imaging performances. However exploitation of adaptive and tunable optics is nowadays limited to high-level or prototype-level instrumentation because of the high complexity and fabrication costs of the deformable optical devices, responsible for the correction of aberrations in light wavefronts. The fabrication of functional, simpler and cheaper deformable optical devices is fundamental in order to apply adaptive and tunable optics in more commonly available instrumentation.

Such deformable optical devices typically consist in deformable mirrors or gratings, able to change their optical properties (shape, focal length or pitch) dynamically, according to the perturbations of the wavefront or the wanted outgoing optical features. The technologies on which such deformable optical devices rely (for example segmented mirrors [6, 7, 8], reflective thin membrane [9], MEMS tunable gratings [10, 11]) suffer of several drawbacks in terms of high weight and complexity or low deformability and tunability of the optical properties. New technologies are required, aiming to overcome these issues.

The fabrication of non planar diffraction gratings, required in a number of optical mounts for the correction of spherical or higher order aberrations affecting the diffracted beam or to add focusing to diffractive capabilities, is of concern as well for the necessary high fabrication costs. The possibility to easily fabricate low-cost arbitrarily shaped reflective diffraction gratings would be a breakthrough for example in monochromoators or spectral imaging techniques.

Elastomeric optics represents a promising technology for the fabrication of optical devices on highly deformable and conformable elastomeric substrates [12]. Reflective elastomeric optics, obtained by metallization of elastomeric substrates, is particularly interesting because of the possibility to limit the dimensions of elastomeric device based optical instruments [13] respect to devices working in transmission. However the metallization of elastomeric substrates by classic coating techniques is problematic because of

the low adhesion and resilience of the reflective metal layer deposited *on* the elastomer surface [14, 15, 16].

Metal-elastomer nanocomposites may represent an alternative and effective approach for the fabrication of reflective elastomeric optical devices since the reflective metal is embedded *in* the elastomeric matrix and does not consist in a continuous rigid metal layer, solving adhesion and resilience problems of coating techniques. However currently available nanocomposites synthesis techniques (chemical [17, 18] or metal ion implantation [19, 20] approaches) do not guarantee the achievement of *reflectivity* and *surface smoothness* required for deformable optical devices.

Driven by the motivations described above, the present thesis is devoted to the fabrication, characterization and exploitation of metal-elastomer nanocomposite based deformable optical components (mirrors and diffraction gratings) obtained by means of Supersonic Cluster Beam Implantation (SCBI) [21]. SCBI allows implanting electrically neutral metal nanoparticles (silver in this work) with low kinetic energy in elastomeric substrates like Polydimethylsiloxane (PDMS). The optical and morphological characterization of the Ag/PDMS nanocomposite will demonstrate that the issues encountered for the fabrication of reflective elastomeric optical components by currently available nanocomposite synthesis techniques can be overcome by using SCBI.

In particular optical properties of reflective elastomeric optical components synthesized by SCBI are affected by Surface Plasmon Resonance (SPR) characterizing silver particles of nanometric size implanted in the elastomeric matrix. A characterization of SPR in light of the theoretical model describing the optical behavior of metal nanoparticles embedded in a dielectric matrix and upon applied strain is necessary for a better understanding and control of the optical properties of the devices during the fabrication process.

Thesis overview

This thesis consists of three parts, for a total of seven chapters. The introductory Part I, composed by the first three chapters, describes the technology on which adaptive optics systems are based and introduces nanocomposite-based elastomeric optics as a possible solution for the replacement of existing deformable optical devices. This section ends with the description of the Supersonic Cluster Beam Implantation (SCBI) technique used in this thesis work for the effective fabrication of the metal-polymer nanocomposite based stretchable optical devices, overcoming the issues typical of nanocomposites obtained by classical techniques. Part II, composed by chapter 4 and chapter 5, is dedicated to the description of the results obtained in the field of stretchable reflective optics. In part III, composed by chapter 6 and chapter 7, a theoretical overview of Surface Plasmon Resonance and our preliminary experimental results on the uv-vis absorption of metal-polymer nanocomposites are presented.

Substantial fractions of this thesis appeared as refereed publications in scientific journals and resulted in the filling of a patent.

Chapter 1. Adaptive and Tunable Optics: applications, working principles and current techniques used in tunable and adaptive optics are presented, followed by a detailed analysis of the drawbacks characterizing the currently used deformable optical devices.

Chapter 2. Nanocomposite-based elastomeric optics: elastomeric optics represents a possible solution to the fabrication of optical devices, specifically designed

to be deformable. However optical elements working in reflection require the metallization of the elastomeric surface. Among different available metallization technologies, nanocomposites represent the ideal solution, matching all the requirements needed from both an optical and a mechanical point of view.

Chapter 3. Supersonic Cluster Beam Implanted nanocomposites: Supersonic Cluster Beam Implantation (SCBI) of metal nanoparticles in elastomeric substrates is introduced in details, in light of the optical and mechanical requirements needed by elastomeric optical elements working in reflection. The state of the art on supersonic cluster beam implanted elastomer is reported in a paper published on *Advanced Materials* [21], while the morphological characterization of the implanted elastomer in a paper published on *Journal of Physics D: Applied Physics* [22].

Chapter 4. Fabrication and characterization of elastomeric optical devices: the characterization of the optical properties of nanocomposite-based reflective stretchable mirrors and diffraction gratings fabricated by SCBI is presented. In particular we show that it is possible to apply the stretchable grating to non-optical grade curved surfaces to add focusing properties to diffractive power. The results of the characterization are the subject of a paper published on *Laser and Photonics Reviews* ([23]).

Chapter 5. A simple scanning spectrometer based on a stretchable reflective grating: stretchable gratings can be used in actual optical mounts and the spectrum of a dye acquired and compared with tabulated data and with spectra acquired with commercial spectrophotometers. This chapter is based on a paper submitted to *Applied Physics Letters* ([24]).

Chapter 6. Surface Plasmon Resonance (SPR): metal nanoparticles are characterized by Surface Plasmon Resonance (SPR), theoretically described by various models. A brief overview of these models is reported in this chapter.

Chapter 7. SPR in SCBI metal-polymer nanocomosites: the experimental evidences and analyses of the Surface Plasmon Resonance of the gold and silver implanted nanocomposites undergoing different treatments are reported. Preliminary SPR characterization of stretched nanocomposites is particularly interesting and promising for a better understanding of the nanoparticles dynamics and topology inside the polymer.

Part I

Deformable optical devices and nanocomposites

CHAPTER 1

Adaptive and Tunable Optics

Adaptive optics is a technology used for the improvement of the performance of optical systems by reducing the effect of wavefront distortions, first proposed in 1953 by Babcock [1] for astronomical applications. The first realization of a working adaptive optics system dates back to 1977, thanks to the availability and improvement of automatic processing power needed for the real-time elaboration of the wavefront shape and control of the correction system, by Buffington [2, 3] and Hardy [4] independentely. From then on adaptive optics was exploited in different other applicative fields requiring the correction of wavefront distortions, in addition to astronomy.

The working principle of an adaptive optics system is depicted in Figure1.1a. Wavefront distortions can be corrected by using *deformable optical devices* (usually *deformable mirrors*), able to dynamically change their optical properties according to the perturbation of the incoming light. A *wavefront sensor*, typically a Shack-Hartmann mask consisting of an array of lenses (also called lenslets) of the same focal length, and a CCD camera or a segmented photodiode [26], reads the perturbation of the incoming light. The local tilt of the wavefront across each lens can be then calculated from the displacement of the focal spot on the sensor respect to the expected position for an unperturbed wavefront. By sampling an array of lenslets, all of these tilts can be measured and the whole wavefront distortion approximated (Figure1.1b). A computer elaborates the information obtained by the wavefront detector and subsequently controls mechanical or electrostatic *actuators* applying proper distortions to the deformable optical device. The interaction of the distorted wavefront with the deformed optical device results in an outgoing planar unperturbed wavefront.

Deformable mirrors are typically used as corrective devices in adaptive optics, but other devices able to dynamically change their optical properties were also developed. Among them tunable diffraction gratings and lenses represent interesting devices. The modification of the grating grooves spacing or height leads to a change in the diffraction resolution and wavelength diffracted at a given angle or in the efficiency of the diffraction orders. Like the crystalline in eyes, the focal length of tunable lenses can be changed by applying deformations to the device that modify the curvature of the lens. In these cases we talk about *tunable*, rather than adaptive, *optics*.

Deformable optical devices and their complex actuation mechanisms represent the main contribution to the high costs still characterizing adaptive optics systems. This limits the exploitation of adaptive and tunable optics to niche applications like large astrophysical telescopes, ophthalmology, high-level laser systems and optical microscopy. The use of cheaper, more reliable devices and simpler actuation systems could represents a breakthrough in these fields, making adaptive and tunable optics commonly available on wider markets.

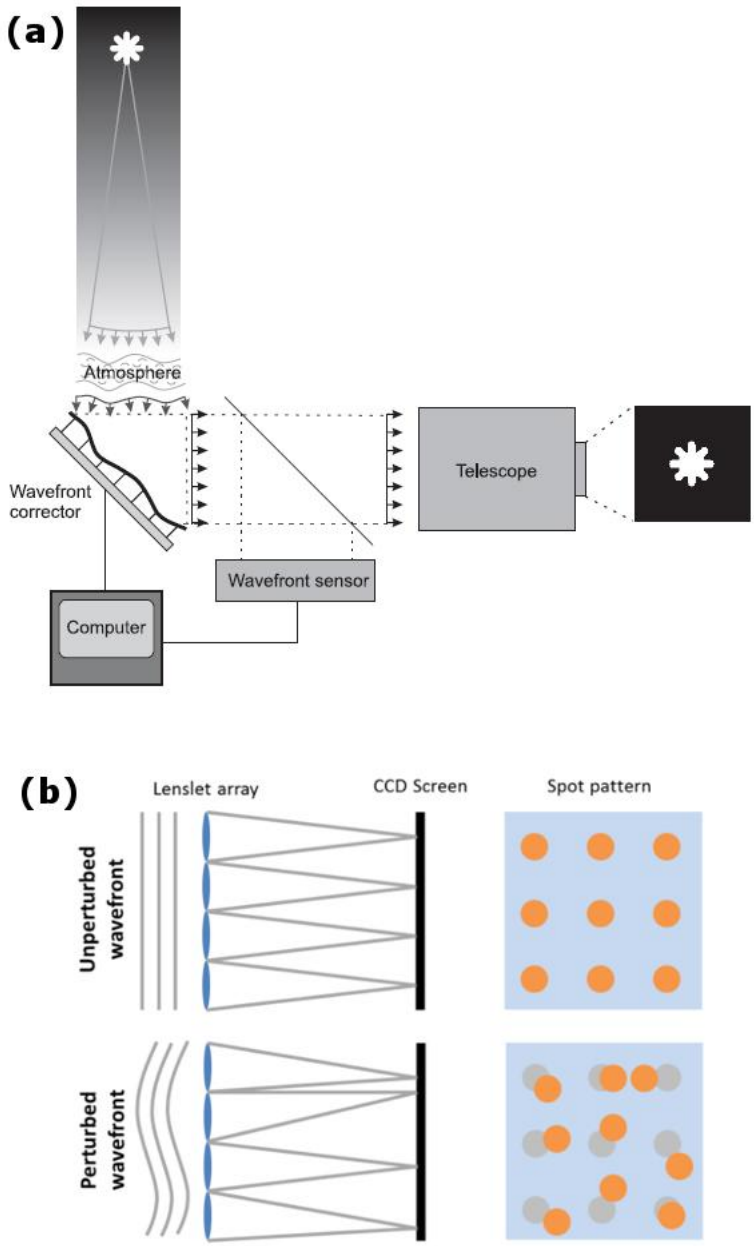

Figure 1.1: (a) Schematics of an adaptive optics system where the aberrated wavefront is reflected off the deformable mirror resulting in a corrected diffraction limited wavefront passed on to a downstream camera. The beamsplitter takes a sample of the corrected wavefront to monitor the phase and send updates to the control electronics to *close the loop* to the deformable mirror. (from [25]). (b) Schematic working principle of a Shack-Hartmannn wavefront sensor. The displacement of the position of the perturbed wavefront focused by the lenslet array respect to the expected position on the photon sensor (typically a CCD camera) gives the information on the distortion affecting the wavefront.

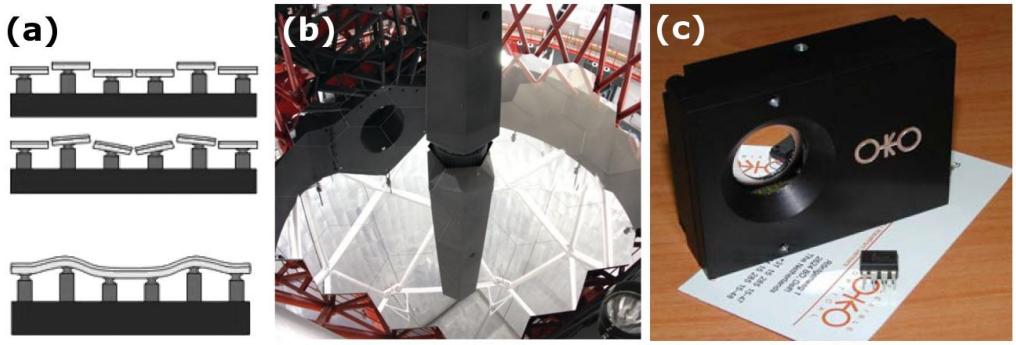

Figure 1.2: (a) The two most common approaches for the actuation of deformable mirrors: working scheme of segmented mirrors (top) and reflective membranes (bottom) [26]. (b) The 10.4m segmented mirror of Gran Telescopio Canarias [28]. (c) MEMS based deformable mirror based on a continuous faceplate (OKO® Technologies) [25].

1.1 Deformable optical devices for adaptive and tunable optics

A fundamental part of adaptive or tunable optics systems is represented by *deformable optical devices*, typically consisting in deformable mirrors or diffraction gratings. Here an overview of the main current technologies on which deformable mirrors or gratings are based will be given.

1.1.1 Deformable mirros

Segmented mirrors, reflective *thin metal membranes*, and *ferrofluids* are the three main solutions for the fabrication of deformable mirrors for adaptive optics [27].

Segmented mirrors [6, 7, 8] represent the most commonly followed approach for its simplicity and the possibility to exploit existent technologies for the fabrication of each segment. A segmented mirror consists in an array of small rigid hexagonal mirrors each actuated by hydraulic or electric pistons for their orientation according to the perturbation of the incoming wavefront (see Figure1.2a for the working scheme and Figure1.2b for an example of a large segmented mirror). The number of segments can vary from few units to few tens and its increase requires an exponential increase of the computing power needed for the actuation. The maximum number of segments for a single segmented mirror was achieved by Hulburd in 1989 [29] with an array of 512 mirrors and over than 10000 constituting elements. Despite their simple concept, segmented mirrors suffer of some drawbacks: they require a high number of expensive actuators and the software needed for the reading of the wavefront and their control is complex. Moreover the high weight of the elements needed for the mirror actuation requires robust supporting structures. Additionally the gap between the segments is of concern because of light losses, extra infrared thermal emission and diffraction of light [27]. This last issue is of particular importance when very high resolutions must be achieved, as in the case of ophthalmology (blood capillaries or single cone cells) [30] and it can be overcome by the use of continuous faceplate mirrors.

Continuous faceplate mirrors are typically based on reflective membranes (e.g. aluminized polymeric membranes) whose shape is modified by push-pull actuators based on piezoelectric materials [9] (Figure1.2a). The spatial continuous deformation of the membrane and the absence of gaps, typical of segmented mirrors, represent the main ad-

Figure 1.3: (a) Ferrofluids without (left) and with (right) an applied external magnetic field: controlling the magnetic field the mirror can assume the wanted shape (images from University of Laval). (b) Actuating mechanism of a ferrofluid based mirror: the magnetic field is modulated by a series of coils [33].

vantages of this class of deformable mirrors. However very thin membranes are required for proper shape modification and wavefront correction, making these deformable mirrors highly fragile [27]. Thicker reflective membranes can be used and bent for the correction of low-order aberrations. MEMS based continuous faceplate mirrors are already available on the market (Figure1.2c [25]) at a very high cost.

Novel techniques are emerging in the field of deformable mirrors: among them the use of liquid mirrors is particularly attractive in terms of simplicity and fabrication costs. Two approaches are followed: in the first a simple liquid metal like Mercury is used. A perfect parabolic shape is assumed by the liquid metal contained in a vessel rotating at a given angular speed. By changing the rotation speed the curvature, and thus the focal length of the paraboloid, can be changed dynamically. A first telescope based on a 4m diameter liquid mirror is under construction in India (International Liquid Mirror Telescope, ILMT [31]). Despite the advantages in term of easy of fabrication and low fabrication costs, issues concerning the toxicity and the weight of the liquid metals limit their practical use.

Ferrofluids, whose shape can be modified by applying magnetic fields (Figure1.3) represent the second approach for the fabrication of liquid deformable mirrors. [32, 33, 34, 35]. Ferrofluids consists in a ferromagnetic nanoparticles layer (size of approximately 10nm) in suspension on a supporting liquid. Differently than liquid metals, ferrofluid based mirrors can correct higher order aberrations with a precision dependant on the dimensions of the coils immersed in the liquid (Figure1.3). The difficulty of using both liquid metals and ferrofluids based mirrors out of the horizontal plane represents the main limitation for the exploitation of such systems in many applicative fields.

From this brief overview on the field of adaptive optics, it is evident the need of new technologies for the fabrication of deformable mirrors, able to overcome the issues presented above. In particular efforts are required in order to make adaptive optics systems cheaper and available also for mass-market products. In certain applicative fields a particular concern consists in the dimensions of deformable mirrors (and thus to the compactness of the instrumentation [30]). In this context MEMS mirrors seems to be the way to follow toward miniaturization of optical apparatus [13] but such devices are still highly expensive.

1.1.2 Tunable gratings

Tunable gratings are currently based on MEMS micromachined on silicon substrates. The first attempt to fabricate a deformable grating modulator dates back to 1992 by Solgaard et al. [10]. The device consisted in a suspended silicon nitride/silicon membrane

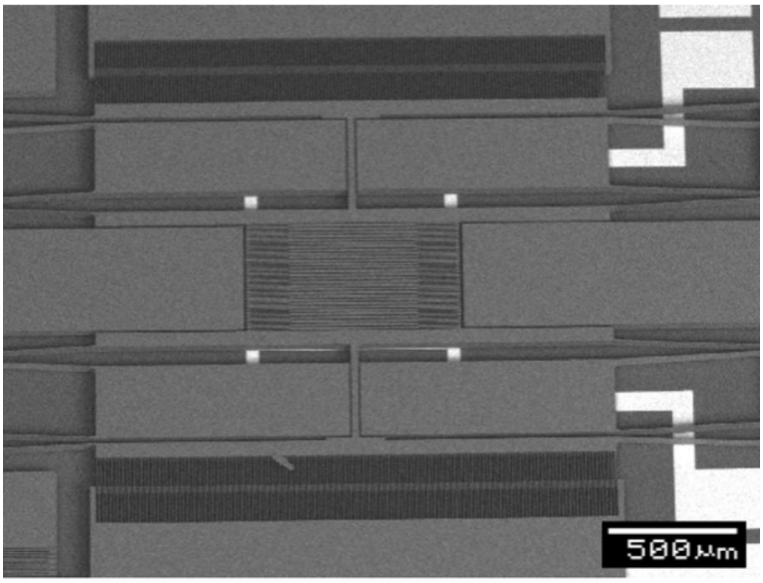

Figure 1.4: Scanning electron microscopy (SEM) picture of a fabricated micromechanical pitch-tunable grating. In the central part of the image the grating beams [11].

and a voltage can be applied between the membrane and the substrate. When no voltage is applied the membrane behaves as a mirror, while when the voltage is turned on the membrane is attracted by the substrate because of the electrostatic force and a depression is created; if depressions are periodic, the three dimensional structure of a grating arises. It is thus possible to switch from mirror to grating behaviors by applying voltages of the order of few Volts, however the control of the efficiency and of the pitch of the grating is not possible.

Recently the control of the grating pitch in MEMS based devices was added, for example, by Yu et al. in 2010 [11]. The grating consists in a sequence of connected silicon bars with dimensions 500μm x 10μm and 5μm spaced. The bars are anchored to two comb drives on the two opposite sides, able to increase the spacing between the bars and thus to change the angle toward which the diffracted beam is directed. This pitch-tunable diffraction grating can work both in reflection and in transmission since the optically active area of the device is free standing. The tunability is quite limited (less than 4%) due to the stiffness of the silicon connection between the bars.

The well-established fabrication process, compatible with micromachining used in microelectronics, and the limited size of the devices, ideal for the fabrication of compact optical instrumentation, represent the main advantages of MEMS tunable gratings. Nevertheless the range of tunability is highly limited by the stiffness of the materials used, not designed to be deformable, and to the poor movement capability proper of the actuation mechanisms currently employed.

1.2 Applications of Adaptive Optics

As already discussed at the beginning of this chapter, adaptive and tunable optics are currently exploited in niche applicative fields. Here an overview of the applications of

adaptive and tunable optics in astronomy, ophthalmology, photonics and microscopy will be given. Disadvantages, open issues and requirements still not achieved by deformable optical devices will be highlighted.

1.2.1 Astronomy

Adaptive optics was first introduced in Astronomy [1] in order to increase the resolving power attainable with optical telescopes on Earth. Since their invention by Galileo Galilei in 1609 and the development of theory of optics by Isaac Newton in 1704, the increase of the resolving power of optical telescopes has been a driving force in the development and design of new instruments. As known from basic optical theory, the resolving power R of a telescope is related to the wavelength λ of the light observed and the aperture diameter D of the instrument, as described by equation 1.1 for circular apertures:

$$R = 1.22\frac{\lambda}{D} \tag{1.1}$$

Since the wavelength is fixed, attempts to build telescopes with larger apertures during the last three centuries have been made. The 102cm refractive telescope placed at the Yerkes Observatory in Wisconsis, USA (1897) represents the largest refractive telescope even built, but larger aperture diameters can be achieved following a mirror-based approach. In this direction it became soon evident that the attainable theoretical resolution, due to the diameter of the aperture of the tube, is strongly limited by *atmospheric turbulence*, even in the best sky conditions.

Assuming the atmosphere as steady and optically neutral, the planar wavefronts coming from outer space would not be affected and could be focalized in just one single point by an ideal optical focusing device, like an infinitely large lens or mirror. However Earth atmosphere is not homogeneous: its density, temperature and composition vary continuosly on a millisecond time scale. As a consequence, the wavefront coming from space is perturbed accordingly and therefore is not focalized in a single point anymore. The angular dimension of the light spot caused by atmospheric turbulence represents the effective resolution attainable. This phenomenon limits the details observable in astronomical objects and makes the construction of even larger telescopes unuseful.

The problem of atmospheric turbulence (also referred as *seeing*) in astronomical observations can be overcome by eliminating the atmosphere and sending telescopes in space. This solution gathers the advantages of eliminating the problem of seeing and increasing the wavelength window observable by instruments. With this aim, Hubble Space Telescope (HST) was designed, built and launched, and in the last twenty years provided us images unattainable with optical telescopes on Earth. Space telescopes are an effective solution but they are highly costly: the construction and launch of HST required an expense of approximately 2.5 billion dollars, while its successor, James Webb Space Telescope, estimated cost should be around 6.5 billion dollars [36].

An alternative cheaper solution consists in *Adaptive Optics*: the theoretical resolving power of optical instruments can be achieved by removing the effects of atmospheric turbulence from the wavefronts arriving on Earth by using deformable optical devices, according to the scheme presented in Figure1.1. Atmospheric perturbations typically occur on a millisecond timescale, thus deformable mirrors must be actuated at frequencies ranging between few tens and few hundreds Hertz [27].

Nowadays adaptive optics is exploited in all the largest astronomical observatories of the world [5] as an effective solution for the problem of seeing. This technology led to the design and construction of huge telescopes, up to 10.4m of diameter (Gran Telescopio

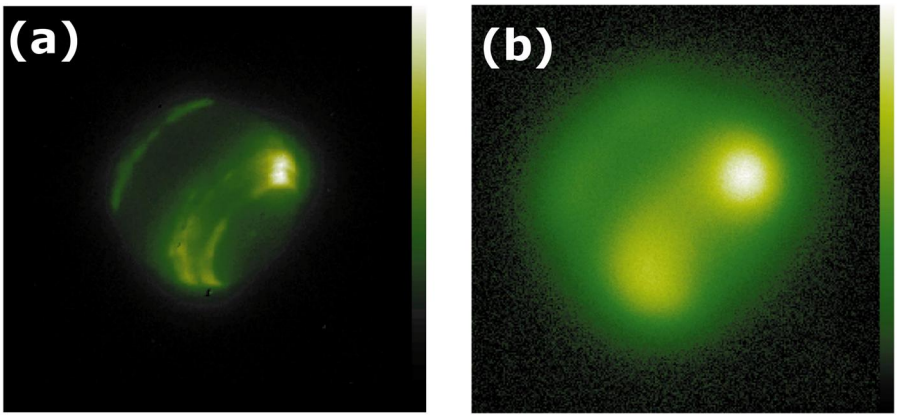

Figure 1.5: (a) Neptune observed with Keck II telescope equipped with adaptive optics. (b) The same image of Neptune without the use of adaptive optics. (from [5]).

Canarias, GTC) with much lower required costs than space telescopes (130 million euros needed for GTC [28]). The difference between an image acquired by Keck II telescope with and without adaptive optics is shown in Figure1.5.

1.2.2 Ophthalmology

Spectacles for correcting eyes aberrations are used since thirteenth century but only in the nineteenth century a full theoretical study of defects like defocusing and astigmatism in eye vision were given by Young [37]. Higher order aberrations, referred as *irregular astigmatism*, were later discovered by Helmoltz [38]. Such high-order aberrations are caused by imperfections in the retina and can not be corrected by simple cylindrical lenses. *Retinal imaging* is necessary for the detection of irregular astigmatism: the aberrated wavefront of light reflected by the retina is mapped [39] by measuring the phase shift of light coming from different points of the retina. In the last two decades the technology on which retinal imaging is based underwent a rapid improvement thanks to the application of adaptive optics in ophthalmoscopy [40] and of the Shack-Hartmann mask sensor for the detection of the perturbed wavefront coming from the eye [41, 42]. Retinal imaging became an easy task requiring only some milliseconds for a complete scan [26], thanks to the development of faster computing systems able to quickly elaborate huge amounts of data. These progresses opened the way to closed-loop adaptive optics systems for the eye and enabling the measurement of the time-dependant microfluctuations in the eye's wave aberration [43].

Closed-loop adaptive optics in ophthalmology is nowadays largely used both in therapy and diagnostics. Retinal imaging can be highly improved: the wavefront reflected by the retina can be corrected and aberrations up to the 10th order can be detected through the analysis of the corrections imposed by the adaptive optics system [42]. This represents a breakthrough in wavefront-guided refractive surgery for the permanent improvement of eye's vision of a patient. For example an excimer laser, treating the affected area of the retina and correcting defocusing, astigmatism and high-order aberrations, can be controlled by the real-time measure of the retina-reflected wave aberration.

Adaptive optics applied to ophthalmology can serve also for the diagnosis of a number of diseases (see Figure1.6). For example accurate measurements of the blood vessels

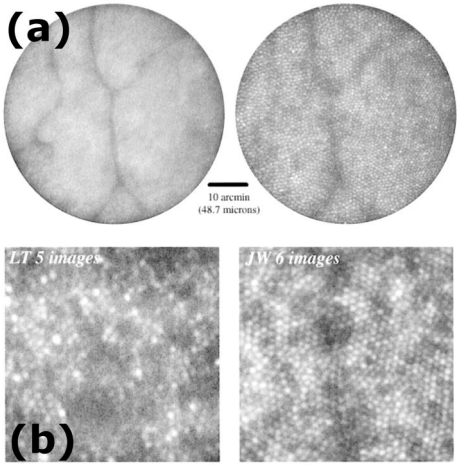

Figure 1.6: (a) 1 degree images of the same retinal location at two different focal planes in the right eye of a living human subject taken by exploiting adaptive optics. In the left image, capillaries as small as 6μm are resolved. By focusing deeper into the retina, the underlying photoreceptors are resolved and the capillaries appear as faint shadows. (b) The left slide shows a sum of 5 images of a patient with retinal dystrophy. The photoreceptor array is patchy compared with a set of 6 images from a healthy eye (from [30]).

structure and functionality are important for the detection and monitoring of some retinal diseases like diabetic retinopathy, and are commonly done with injected contrast agents or doppler methods, affected by a low lateral resolution and toxicity of the fluorescein agent [26]. Adaptive optics provides non-invasive and high resolution imaging of blood flow in vessels, avoiding the use of contrast agents [44].

The correction of eye's aberrations also improves the imaging of the cone mosaic [30]), the study of the arrangement of S, L and M cones [45] and the detection of individual cone diseases. The high resolution attained with this technology will allow to test the effectiveness of treatment interventions and learning more about the mechanism of retinal diseases. Nevertheless some improvements are likely: deformable mirrors are the most effective technology for adaptive optics, but they are usually characterized by large dimensions and high fabrication costs.

1.2.3 Microscopy

Imaging capabilities of optical microscopes are often affected by aberrations, compromising the resolution and the contrast achievable by the observer, particularly with high resolution instruments like confocal or two-photon microscopes [46]

The sample and the optical setup represent the two main causes for aberrations in microscopy. In particular the large numerical aperture and the mismatch of the refraction index between the lenses and the sample are the causes for the strong spherical aberration often present in microscopes. These low-order aberrations can be easily corrected by applying field curvature correctors or by imaging with immersed objective in order to create a continuum between the refractive indexes of the lens and of the sample. Nevertheless high-order or time-dependant aberrations are present, mainly when dealing with living tissues, whose refractive index can be highly inohomogeneous in the vertical direction and in time. In order to overcome these problems, adaptive optics in microscopy

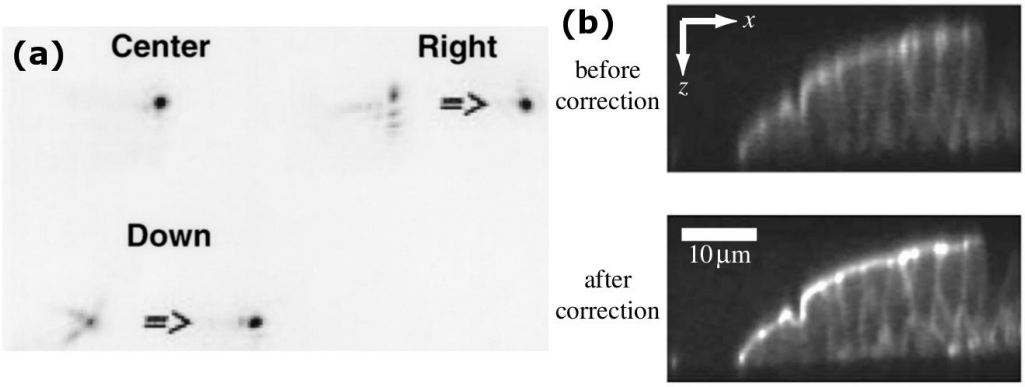

Figure 1.7: (a) Confocal microscopy inverted images of the focus spot on axis, for a right scanning of 70 mm and a down scanning of 50 mm (top left). The off-axis spots are displayed uncorrected and corrected (top right and bottom). All the corrected spots and the centered one correspond to Airy patterns (from [47]). (b) Adaptive confocal fluorescence microscope images of labelled mouse intestine. Aberrations were determined using sequential modal wavefront sensing (from [48]).

was introduced [47], allowing for high resolution dynamic imaging of living tissues or reliable 3D scanning of semi-transparent biological samples. Figure1.7 shows the differences between the images obtained with a classic and an adaptive optics equipped confocal microscope.

Moreover while confocal microscopy allows obtaining a 3D reconstruction of the sample, with two-photon microscopy only a bi-dimensional image can be acquired. This issue can be overcome with the use of *deformable lenses*, able to change their curvature, and thus their focal length, upon the application of an electric field or mechanical stress, literally *squeezing* the lens in the plane orthogonal to the optical axis [49]. Deformable lenses able to change their focal length in a range of up to 1mm, allows investigating quite thick samples with the high resolution proper of two-photon microscopy.

1.2.4 Photonics

Photonics can take advantage of adaptive optics as well, in particular for the correction of perturbed wavefronts inside laser cavities. Efforts in improving the intensity of exiting light have been concentrated on increasing the energy through the reduction of the pulses duration and their temporal coherence. Moreover wavefront distortions of the beam are often neglected, even if they play a fundamental role in the beam intensity. Distortions in the wavefront affect the spatial quality and thus the beam ability to be focused, reducing the attainable focused intensity [50].

More interesting, tunable optics may allow to adjust the wavelength of a laser system. Usually laser cavities consists in a couple of mirrors continuously reflecting the light passing through a gain medium, and are only able to provide monochromatic light beams, with a wavelength depending on the design of the optical cavity. The high intensity, collimation and coherence of laser light suggest its exploitation, for example, in gas sensing application, since gases are commonly characterized by a strong absorption at given wavelengths ranging from 700nm to 3000nm [51]. Tunable lasers, typically Distributed Feedback lasers (DFB), represent an effective solution for such applications, avoiding the use of multiple monochromatic light sources. Mirrors of DFB lasers optical

cavity are replaced with tunable gratings able to select a given wavelength resonating in the cavity by changing their pitch. Fabrication techniques and costs of such tunable gratings currently represent a limiting factor for the development and diffuse use of DFB lasers.

CHAPTER 2

Nanocomposite-based elastomeric optics

The widespread exploitation of adaptive and tunable optics system is mainly limited by the high fabrication costs and technical issues of the deformable optical devices and by the complexity of their actuation systems as well. The main technological issues of currently available deformable optical devices are related to the stiffness of the materials used and the poor tunability and reliability of the devices.

2.1 Elastomeric optics

The introduction of the concept of Elastomeric Optics by Whitesides' group in 1996 [12] represented an important breakthrough in the deformable optical elements fabrication technology. Elastomeric optical devices consist in optical components prepared using elastomers, defined by IUPAC as *polymers that display rubber-like elasticity* [52], and designed to be reversibly deformable. A low Young modulus and a high failure strain in comparison with other materials make elastomers the ideal choice as substrates for the fabrication of deformable optical devices. Among them Polydimethylsiloxane (PDMS) is one of the most popular because of its low cost, nontoxicity and biocompatibility. PDMS is easy to process using standard microfabrication techniques, in particular replica molding of existing masters on a scale suitable for optical applications (0.1-10μm size features) with high fidelity is possible, as it will be demonstrated in this thesis work.

Low fabrication costs, *large* tuning capabilities of the optical properties, durability and, in some instances, new types of performances generally characterize elastomeric optical devices. Such optical elements may not be comparable with existing rigid optical devices in terms of attainable optical quality, but the advantages due to their deformable nature overcome these possible limitations [12].

2.1.1 Transparent elastomeric optics

Elastomeric materials are usually highly transparent in the UV-vis range (300-800nm for PDMS). This property makes elastomers the ideal choice for the easy fabrication of transparent deformable optical devices such as lenses or diffraction gratings working in transmission. As already discussed in the previous section, deformable lenses can be exploited in those applications where a tuning of the focal length is needed, for example in a 3D scan of biological samples with a two-photon microscope. Lenses are not the only obtainable transparent optical elastomer-based components: light valves [53], Fresnel lenses [54], and transmission deformable gratings, both for scanning [55, 56, 57] (even embedded in MEMS [58]) and sensing [59, 60] purposes, can be easily found in literature.

2.1.2 Reflective elastomeric optics

Deformable optical elements such as mirrors or reflective diffraction gratings can be fabricated with elastomers, however *metallization of the elastomer surface* is required in order to reach a sufficient reflectivity. Reflective elastomer-based optical devices potentially represent an effective solution for the drawbacks affecting deformable optical devices needed in adaptive optics, opening new opportunities for different technologies.

Elastomeric mirrors may represent a simpler, cheaper, more compact and reliable alternative to currently available deformable mirrors. The continuity of faceplate mirrors, the robustness of segmented mirrors together with a low weight, a high degree of deformability and a low fabrication cost in a single elastomeric component may open the way to the exploitation of adaptive optics in a wider range of applicative fields. High-level amateur telescopes to novel optical components for satellites, where the weight of each single component is matter of concern, or the production of more compact ophthalmoscopes [13] or portable and dynamic eye vision correcting instruments [61] represent just few examples of applicative fields in which elastomeric mirrors can be exploited. Moreover the high elasticity and conformability allow elastomeric mirrors to be applied to arbitrarily shaped surfaces for the permanent correction of both low- and high-order aberrations as well. In particular the problems of astigmatism, spherical aberration and coma caused by off-axis alignment of optical components, typical of several optical mounts [62, 63] can be solved by applying elastomeric mirrors to properly designed curved surfaces. In addition elastomeric optical devices can be characterized by an extremely smooth surface, as it will demonstrated in Section 3.4.4. This represents a main breakthrough in the optical instrumentation fabrication process since an optical grade supporting curved surface is not required, considerately reducing the device machining cost and complexity respect to the state of the art.

Similarly to elastomeric mirrors, reflective elastomeric gratings could represent a breakthrough in the downscaling of optical analytical instrumentation in terms of dimensions and price as well. Reflective diffraction gratings are much more commonly used in commercial optical mounts than transmission grating systems: the dimension of optical systems can be reduced by *folding* the optical paths using reflecting devices. Moreover, reflective gratings are not limited by the transmission properties of the transparent substrate and can operate at much higher diffraction angles [63].

Elastomeric reflective diffraction gratings [12] represent the typical example of elastomeric optical devices. In classic rigid gratings, currently available on the market, the diffracted wavelength λ at a given angle θ_o is selected by rotating the grating. The change of the incidence angle θ_i of the impinging light selects the wavelength diffracted at the angle θ_o, according to the well-known law of planar gratings:

$$\lambda = d\frac{\sin\theta_o - \sin\theta_i}{m} \tag{2.1}$$

where d is the pitch of the grating and m is the diffraction order considered. This approach, commonly used in most of monochromators and spectrometers, requires a highly precise rotation mechanism, increasing the cost of the optical instrumentation. Elastomeric gratings allow to keep the angle of incidence of the impinging light θ_i fixed. The diffracted wavelength λ at a given angle θ_o is selected exploiting the change of the grating pitch d when the device is *stretched*, as shown in Figure2.1, requiring cheaper and easier mechanisms.

The most appealing property of these devices consists in the possibility to easily and conveniently add optical power to diffractive elements by applying elastomeric gratings

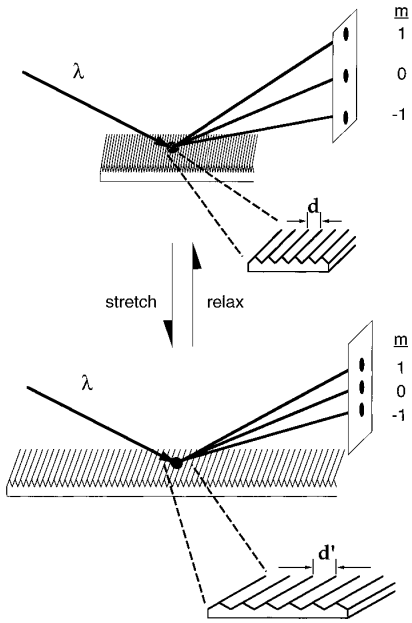

Figure 2.1: Strain applied to an elastomeric diffraction grating changes its grooves periodicity and alters the spacing of the diffraction pattern [12].

to arbitrarily shaped non-optical grade surfaces, as in the case of elastomeric mirrors. The limited number of focusing and correcting components needed in optical mounts and the aberration-free imaging capability of such devices would open the way to the design, for example, of cheaper, smaller, and portable spectrographs available on a wider market and applicable to a wider range of fields.

Despite the clear advantages elastomeric optical elements working in reflection would bring in the design of optical mounts, this technology was poorly developed since their first appearance in 1996 [12]. The lack of an effective technique for the metallization of the elastomeric surfaces meeting the strict requirements needed for reliable reflective elastomeric optical devices can be considered the main cause for this lack of development of the technology.

2.2 Requirements for reflective elastomeric optics

2.2.1 Reflectivity

Reflective optical devices are usually designed to work in a given wavelength range according to the application in which are supposed to be exploited. Commercially available mirrors or gratings are usually characterized by a reflectivity between 90% and 100% and by a uniform reflectance spectrum. The same performances in terms of reflectivity are not strictly required by deformable optical devices since their high deformability represents the real added value of such devices [12]. Although no reference data are present in literature for the reflectivity required in elastomeric optical devices, we can assume that a reflectivity greater than 60% should be sufficient for most of the applications mentioned in the previous chapter.

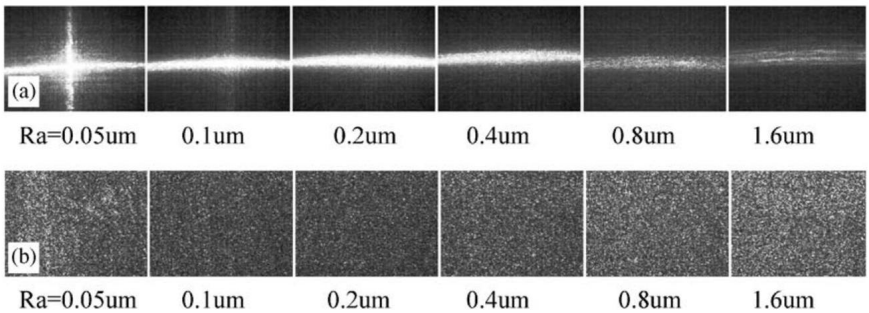

Figure 2.2: Scattered light patterns vs. surface roughness. (a) Light scattering pattern vs. roughness. (b) light speckle pattern vs. roughness. Here Ra represents the *arithmetic average of absolute values* roughness, defined as $Ra = \frac{1}{n}\sum_{i=1}^{n}|y_i|$ (from [64]).

2.2.2 Surface morphology

Surface smoothness is a fundamental property of each optical component, working both in reflection and in transmission, and is quantified by the surface roughness Rq (in this context only *the root mean squared roughness* will be considered) defined as:

$$Rq = \sqrt{\frac{1}{n}\sum_{i=1}^{n} y_i^2} \tag{2.2}$$

where y_i represents the deviation of the measured vertical profile of the surface from the mean vertical level and n the number of points measured for the real profile. Surface roughness is responsible for the *scattering* of the incident light by the surface of the optical device, as can be seen in Figure2.2.

Scattering consists in a random diffusion of the impinging light intensity by a rough surface. Surface roughness must be therefore finely controlled and minimized. In 1961 Bennett and Porteus came up with a theoretical model describing the relationship between the reflectance of a surface and its RMS roughness [65]. Beckmann and Spizzichino in 1965 introduced the concept of *Total Integrated Scatter* (TIS, the total power of light scattered into the hemisphere above the surface divided by the power incident upon the surface) in optics [66] and found an analytical relationship between TIS and surface roughness:

$$TIS\,(Rq) = 1 - \frac{R}{R_0} = 1 - e^{-\left(\frac{4\pi Rq\cos\theta_i}{\lambda}\right)^2} \tag{2.3}$$

where R is the reflectance of the scattering surface, R_0 is the reflectance of the ideally flat surface, θ_i is the angle of incidence respect to the normal of the surface and λ the wavelength of light. As can be seen from equation 2.3, the fraction of scattered light depends on the surface roughness, as expected, and on the angle of incidence of light as well. Figure2.3 shows the trend of the TIS function as a function of both RMS roughness Rq and the incidence angle θ_i. Optical devices working in reflection should be characterized by a TIS not larger than 5% in order to achieve a good optical quality. Extremely low RMS roughnesses are thus required, especially for light impinging normally or with low angles of incidence to the surface (Figure2.3a). Moreover, deformable optical devices applied to highly curved surfaces and used in off-axis configurations requires a

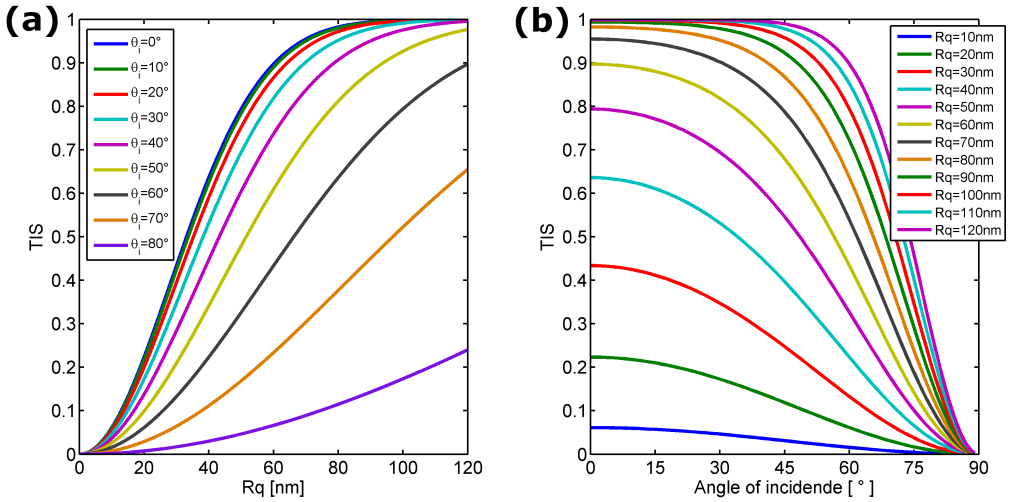

Figure 2.3: (a) Trend of the TIS function (fraction of light scattered by a rough surface) as a function of the surface roughness for different angles of incidence. (b) Trend of the TIS function as a function of the incident angle for different surface rougnesses.

uniform and limited (below 5%) scattering percentage for a wide range of light incident angles. This requirement is again guaranteed by an extremely low surface roughness. As reported in Figure2.3b, the scattering relative to a roughness of 10nm is below 6% (upper limit with normal incident light) and is constantly below 5% for incident angles larger or equal to 26°.

2.3 Resilience and stretchability

Reflectivity and surface smoothness are fundamental requirements easily satisfied by classic coating techniques currently exploited for the metallization of reflective optical elements. However the optical response of reflective elastomeric optical components strongly depends on additional properties required for such devices and related to reflectivity and surface morphology: *resilience* and *stretchability*.

Elastomeric optical devices are designed to be deformable, thus to change their shape and/or dimensions. Each deformation, even simple bending, can be led back to a stretching of the material, strictly related to the adhesion of the rigid reflective metal layers to the polymer surface by means of the Young modulus mismatch between the two materials. Generally when a thin metal film on a polymer substrate is stretched, the rigid metal film is not able to follow the deformations of the underlying elastomer and encounters rupture and delamination at strains ranging from few percents up to few tens percents in best cases [67]. This range of variability of the rupture threshold depends on the adhesion of the metal thin film to the polymeric substrate. In the case of no adhesion, the maximum strain achievable by a freestanding thin metal film without encountering breakage is less than 1-2% [68, 69, 70]. The delamination mechanism of the metallic film when mechanically stressed is schematically shown in Figure2.4. When a strain is applied dislocations in the metal lattice arise leading to the formation of necks on the metal layer [68, 71, 67], where all the stress caused by the applied strain concentrates. The neck gets thinner and thinner yielding to the rupture of the metal layer where the neck arose.

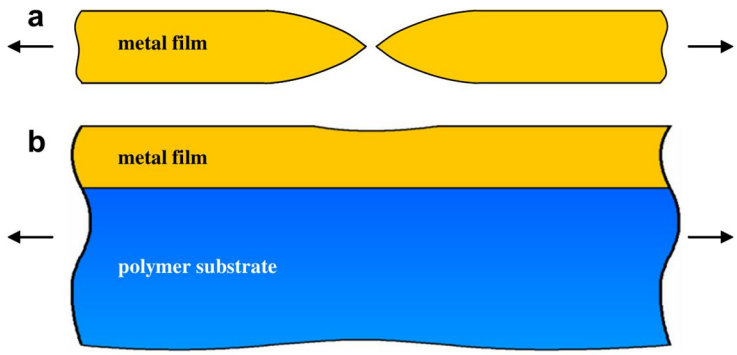

Figure 2.4: (a) Free-standing thin metal film breakage takes place where the neck is formed, due to the arising of dislocations in the metal lattice caused by the stress. (b) If the metal layer is well adherent to the polymer surface, the stress on the metal layer is dissipated by the polymer, increasing the stretchability of the former (image from [67]).

If the metal film is well adherent to the polymer surface, the stress accumulated on the neck is partially dissipated by the subtending polymer (see Figure2.4b), increasing the breakage threshold. However the formation of the neck gives rise to a point in which the metal film is detached from the polymer surface and here *delamination* takes place. The control on the formation of microcracks in metal layers on top of polymeric surfaces [14, 72] can be useful in order to limit and improve the stretchability of such systems [73, 74]. However microcracking and delamination dramatically increase the surface roughness of the metallized polymer, thus affecting the optical quality of the device. An optimal adhesion of the metal reflective layer is of fundamental importance in order to avoid the formation of microcracks, preserving the optical quality of the elastomeric reflective component when subjected to mechanical stress.

The breakage threshold of the rigid metal layer can be increased by improving its adhesion with the elastomeric surface [71] thanks to deposition of a thin chromium or titanium film between the polymer and the reflective coating [72, 75, 76, 77]. The better affinity of Cr or Ti with the elastomer helps in avoiding delamination, while cracking remains an issue since it causes a dramatic increase of the surface roughness on the microscale, leading to scattering and other detrimental effects in the optical response of the device [78]. The mismatch between the Young moduli of the elastomeric surface and the rigid metal layer deposited on it also causes the formation of buckles and wrinkles on the surface of the device [79, 80], independently on the adhesion between the two layers. For example Guerrero et al. [81] observed the arising of unexpected diffracted beams orthogonal to those due to the grooves of the grating. The formation of large periodic cracks or buckles in the stretching direction is supposed to be the cause for the appearance of such secondary diffracted spots. Thinner metal layers show a better adhesion as well, and larger maximum stretching thresholds (up to 32%) [82].

Stability under stretching is also important: the optical response must be reliable and stable in time and with the increase of the number of stretching cycles. A constant behavior of the reflected or diffracted spots shape or angular dimension during a single or after a certain number of stretching cycles is fundamental in order to ensure the optical quality of the device and to avoid continuous calibration procedures. Elastomeric substrates and reflective layers must be then chosen accordingly.

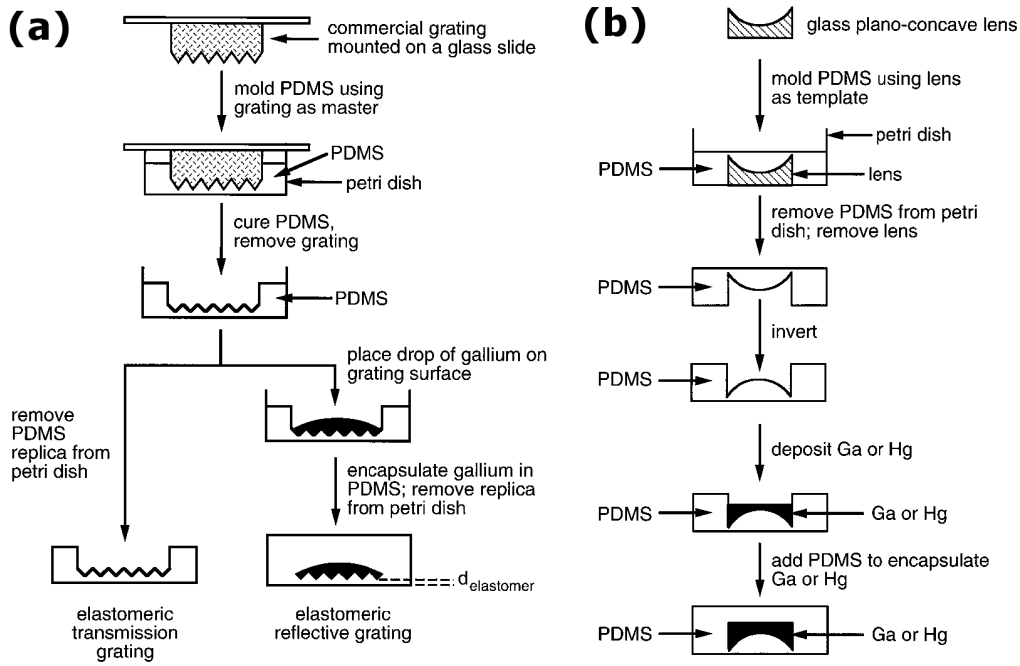

Figure 2.5: Fabrication process of (a) elastomeric gratings and (b) elastomeric mirrors with liquid metals [12].

2.4 Metallization of elastomeric optical devices

2.4.1 Liquid metals

The first attempt to fabricate reflective elastomeric mirrors or gratings dates back to 1996 by Wilbur et al. [12]. The problems of cracking and delamination of reflective thin metal films *on* or *in* elastomeric substrates were overcome by the use of *liquid metals* (mercury or gallium) embedded in the elastomer. The fabrication process is similar for reflective elastomeric gratings and mirrors as shown in Figure2.5.

The basic idea consists in replicating an existing rigid commercial grating or mirror with PDMS (in particular Dow Corning Sylgard 184) by molding technique, covering the optically active molded surface of the elastomer with mercury or gallium and finally encapsulating the liquid metal by a second elastomeric layer. This technique completely overcome the problems of metal adhesion and roughness of the reflective layer, however liquid metals have a considerable weight (the densities of mercury and gallium are $13.546g \cdot ml^{-1}$ and $5.907g \cdot ml^{-1}$ respectively) and a macroscopic thickness is needed to ensure the complete coating of the surface, leading to deformations of the elastomeric structure. These deformations affect the optical response of the device, as can be seen in Figure2.6. The elastomeric structure of the device can be reinforced by increasing the PDMS thickness, however thicknesses larger than 2mm are detrimental for the optical quality of the components, introducing a considerable light scattering, as stated by the same authors [12].

In the fabrication process discussed above, molding is generally a fundamental step for the fabrication of elastomeric optical devices, however the metallization of the elas-

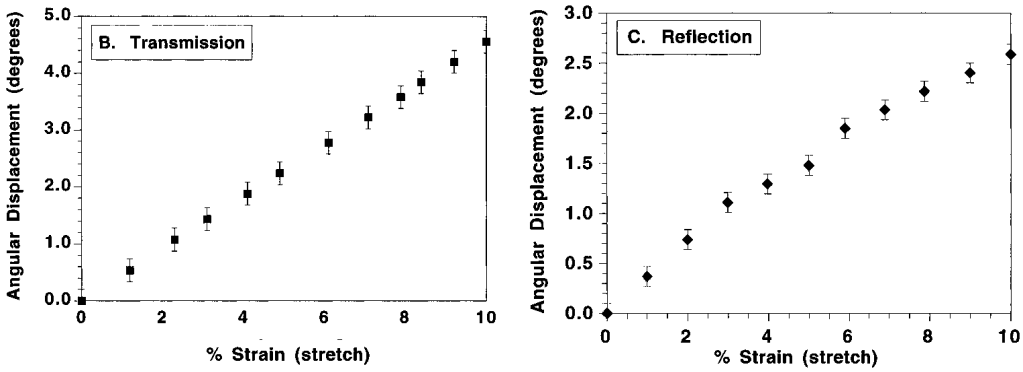

Figure 2.6: Optical response of an elastomeric grating working in transmission (left) and in reflection (b) with an encapsulated liquid metal (gallium) when subjected to stretching up to 10%. It is worth noting the slightly non-linearity of the metallized grating due to the deformations imposed by the weight of the liquid metal [12].

tomers surface for reflective purposes remains an open issue. In the following sections an overview of the commonly available elastomer metallization techniques is given, with a detailed analysis of the main advantages and drawbacks.

2.4.2 Physical Vapor Deposition

One of the most common and widely used techniques in elastomeric optics is *physical vapor deposition* (PVD) of metal atoms on the top of polymeric surfaces [82, 83, 81, 78]. A liquid or solid metallic material is vaporized in atoms or molecules and transported through a vacuum or low pressure gaseous environment, to the substrates where it condenses. PVD is usually characterized by a high deposition rate (tenths of nanometers per second), allowing to deposit few nanometers up to few micrometers thick rigid and continuous metal films *on* the elastomer surface.

PVD techniques differentiate according to the method use for the evaporation of the metal:

- **Thermal evaporation**: Powders, pellets or wires of the metallic material are melted in a tungsten or molybdenum crucible, whose evaporation temperature is much higher than the metal to deposit, and heated by Joule effect by means of the high current (tens of amperes) flowing in the crucible (Figure2.7a). Evaporated metal atoms travel in vacuum toward the substrate to coat with an energy of approximately 0.1eV, thus not causing any damage to the polymeric substrate. The heat generated by the crucible is of concern for the physical-chemical properties of the elastomer, especially for substrates with a low melting point (100-120°C) and for long deposition times.

- **E-beam evaporation**: An energetic electron beam (up to 15keV) is directed toward the metal target that is locally heated beyond its evaporation temperature by the high energy of the electrons (Figure2.7b). Changing the electrons energy the deposition rate can be controlled (from tenths to some nanometers per second) while the evaporated metal atoms energy is comparable to thermal evaporation. The local heating of the metal target, and thus its reduced influence on the polymeric substrate, represents the main advantage of this technique.

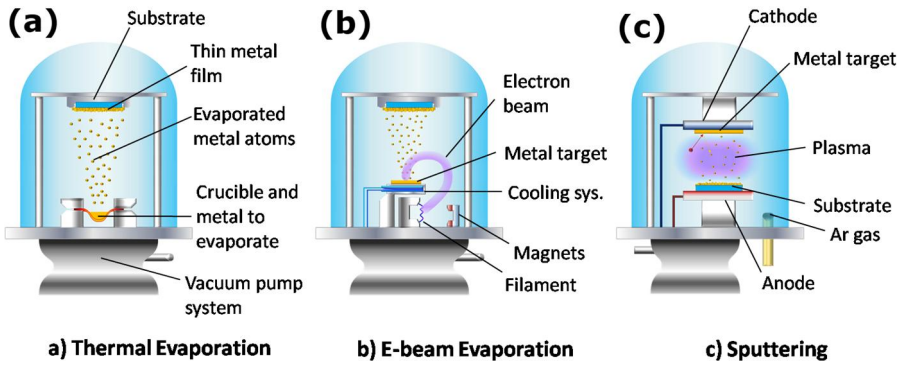

Figure 2.7: The three PVD processes: (a) Thermal evaporation, (b) E-beam evaporation, (c) Sputtering.

- **Sputtering**: Ions are accelerated toward a metal target and the sufficiently high ions energy (typically Ar^+, with energies of some keV) extracts metal atoms from the target (Figure2.7c). Metal atoms reaching the elastomeric surface are characterized by energies higher than the previous methods, between 1 and 100eV, leading to a better adhesion to the polymeric substrate [84]. However the deposition rate is lower than thermal or e-beam evaporation.

The high deposition rate represents the main advantage of coating techniques like evaporation, allowing reaching considerable thick metal layers on large areas in a reasonable amount of time, as required for the scalability of the fabrication process. A good reflectivity (0.7-0.8) can be achieved [85] with reasonable thin metal layers, however many are the drawbacks.

The *stiffness* of the continuous metal layer *on* the soft elastomer surface and the *low adhesion* between the metal layer and the polymer are matter of concern because of its cracking and delamination when mechanically stressed [14, 72]. The maximum stretching percentage after which cracking or plastic deformations of the metal layer take place is limited to 7-8% of its original dimensions. Cracking arises even by using sputtering [75, 15, 14], involving higher impinging energies and so better adhesion between the metal and the polymer.

Condensation of metal atoms on the surface of elastomers and the subsequent formation of a continuous metal layer induces a stress on the polymeric surface, leading to the formation of microwrinkles [79, 16] for deposition on prestretched substrates (in order to improve the stretchability of the material) [76, 86] even without externally mechanical deformations. Despite the attempts to exploit these ordered spontaneous structures as stretchable optical devices (e.g. tunable diffraction gratings [87]), tunabilities larger than 3.6% are not achieved. Moreover the control over the formation of microwrinkles is not trivial and their dimension and periodicity may negatively affect the optical response of the evaporated elastomeric optical device.

In the end the high divergence and inhomogeneity of the atomic beam cause a strong *shadowing effect*, representing a limiting factor for the uniform coating of three-dimensional structures like gratings grooves. The highly irregular profile of an evaporated elastomeric grating caused by cracking, wrinkling and shadowing, will be presented in the next chapter.

From this extensive discussion it is clear that rigid thin metal layers deposited *on* the

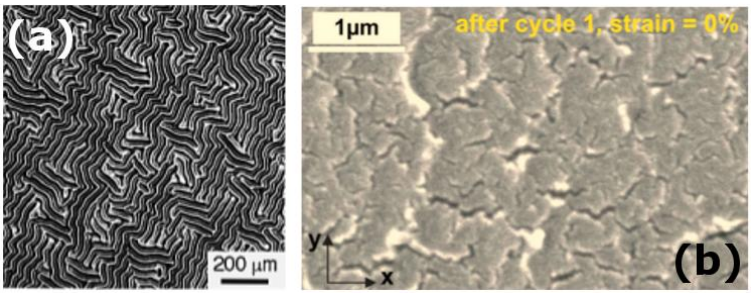

Figure 2.8: (a) Optical microscopy images of wrinkles on a thermally evaporated PDMS surface with 5nm of Chromium and 50nm of Gold [79]. (b) SEM micrograph of evaporated PDMS surface. It is worth noting the formation of cracks even without mechanical solicitations applied to the sample. PDMS was e-beam evaporated with 5nm of Chromium and 25nm of Gold [72].

polymer surface do not represent an effective solution for the fabrication of reflective elastomeric optical devices. The obtained material does not match the optical quality required for functional and reliable deformable optical device. Adhesion and delamination can be improved by *embedding* a pre-formed metal layer *inside* the polymeric matrix, however cracking remains an issue.

2.5 Metal-elastomer nanocomposites

Nanocomposite materials can represent an effective solution for the fabrication of reliable elastomeric optical devices overcoming the limitations of metal-polymer bi-layers in terms of resilience of the reflective layer [21]. A metal-polymer nanocomposite is a composite material consisting of metallic particles with nanometric size *embedded* in a polymeric matrix. They were exploited in order to overcome the issues related to adhesion, cracking and delamination due to the presence of two layers with different stiffness in metal-coated elastomers in different fields like stretchable electronics. In nanocomposites the metallic material consists in single metal nanoparticles able to slightly move far away each other and re-arrange when a mechanical deformation is applied to the device, and to restore their original position when the material is released.

Despite the several advantages related to resilience and mechanical properties nanocomposite materials could bring, no literature can be found in the field of nanocomposite-based elastomeric optics. This lack is due to the different synthesis techniques, not allowing to obtain nanocomposites characterized by appropriate optical properties in terms of reflectivity and surface smoothness required for the fabrication of functional elastomeric optical devices. In particular reflectivity and elasticity of metal-polymer nanocomposites represent critical issues: in order to achieve reflectivities mentioned in the requirements for elastomeric reflective optics, the polymer must be highly loaded with metal nanoparticles. Such a high nanoparticle concentration is difficult to obtain with nanocomposite synthesis techniques described below, and strongly affect the elasticity of the obtained material. The Young modulus of metal-elastomer nanocomposites increases with the nanoparticles concentration (or *filling factor*) according to Guth equation [88, 89], as shown in Figure2.9. A trade-off between a high loading of the polymeric matrix, needed in order to achieve a good reflectivity of the nanocomposite, and the elasticity of the obtained material, fundamental for deformable and stretchable applications, must be found.

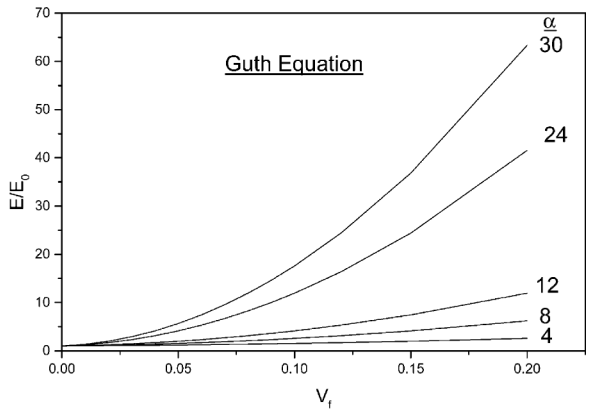

Figure 2.9: Increase of nanocomposites Young modulus as a function of the concentration of the metal filler for different filler aspect ratios (α represents the ratio between the length and the breadth of the filler particles) [89].

The main nanocomposites synthesis approaches are described in the following sections.

2.5.1 Chemical synthesis of nanocomposites

Chemical synthesis represents the most common and simple technique for the formation of metal-polymer nanocomposites and can be divided in two different approaches depending on the way the nanoparticles are synthesized.

1. *In-situ* approach consists in the the simultaneous synthesis of metal nanoparticles and the polymer by means of precipitation of polymer and nanoparticles starting from metal salts [17], thermal decomposition of metal precursors dissolved in the polymer [90, 91], coevaporation or copsputtering of polymers and metal atoms condensating in metal nanoparticles [92, 93] or CVD and PVD with thermal treatments for particles aggregation [94].

2. In *ex-situ* methods nanoparticles are first prepared by a controlled precipitation of a colloidal precursor [90, 95, 96] or by other chemical or physical methods, and then embedded in the polymer liquid monomer precursor by means of sol-gel methods [18, 97, 98, 99]. The mix of monomers and metal nanoparticles is then polymerized. Chemically synthesized nanoparticles often present an inert shell (usually metal oxide o functional groups) aiming to avoid clusters aggregation and deactivation [91].

In both cases a uniformly filled bulk nanocomposite is obtained.

Three dimensional structures, like gratings grooves, can be easily obtained by molding technique of existing masters, the only requirement being the nanoparticles size smaller than the features to replicate. The surface roughness of the nanocomposite coincides with the roughness of the elastomeric substrate (that in case of untreated PDMS is few nanometers) and depends on the polishing of the surface on which the mirror or grating is molded. In such a way light scattering can be easily controlled by choosing the appropriate polymer and by a proper machining of the molding master.

The granular nature of the reflective layer may also give rise to light scattering or absorption, depending on the nanoparticles size. Light scattering can be limited by using nanoparticles with a diameter d much lower than the light wavelength λ. Nanometric sized metal particles also present a strong absorption in the visible range due to Surface Plasmon Resonance (SPR) [100], whose wavelength peak depends on the size and concentration of the nanoparticles.

The main drawbacks of the use of chemically synthesized nanocomposites consist in the use of chemicals for the production of metal nanoparticles and the poor reflectivity of the obtained nanocomposites. Many polymers, in particular elastomers, suffer of chemical-physical degradation when exposed to acids, bases or other chemicals, also used in the metal nanoparticles synthesis [101]. Some elastomers are also well known for their considerable swelling following solvent absorption [102]: this can alter the physical properties and affect the geometry of the elastomeric substrate.

Chemical synthesis (both-in situ or ex-situ) allows obtaining nanocomposites uniformly filled with metal nanoparticles and, for in-situ approaches, the wanted cluster concentration can be reached with a proper concentration of metal precursor. The precursors must then be absorbed by the preformed elastomeric matrix, making thus very difficult the achievement of filling factors larger than 30-50% [103]. If mixed with the liquid pre-polymer, the high precursor solvents concentration may impede the elastomer polymerization. Ex-situ techniques present similar problems: the high concentration of metal nanoparticles inside the liquid monomers solution avoids the monomer polymerization because of the interaction between the polymer chains and the nanoparticles surface [104, 105]. As a proof for the difficulty of obtaining highly loaded nanocomposites by chemical synthesis, no works on elastomeric optical devices are reported in literature.

In conclusion, the advantages of the nanocomposite approach in the fabrication of elastomeric reflective devices remains however superior to classic coating techniques in terms of stretchability and resilience of the reflective layer to the elastomeric substrate. A *physical* technique enabling the fabrication of metal-polymer nanocomposite characterized by higher particles concentrations, and thus reflectivities, is likely to be used.

2.5.2 Ion Implantation

Ion implantation, widely used in the microelectronic industry for the doping of silicon substrates, represents also an effective technique for the fabrication of metal-polymer nanocomposites by means of implantation of metal ions or nanoparticles inside polymeric matrices. The working principle of this technique is schematically represented in Figure2.10. An electric field accelerates metal ions or particles extracted from a source and ionized with different methods (electronic ionization, electric discharges, radioactive ion sources among them). Before a further acceleration and implantation in the substrate, a magnetic field deflects the ion beam toward a slit thanks to the Lorentz law. The exiting ions mass can be selected by tuning the intensity of the magnetic field. The selected ions than undergo a second acceleration by a second electric field and get collimated by a series of magnetic quadrupoles. Finally two couples of scanning electrodes address the ions to the point of the polymer to implant.

The penetration depth of the ions in the polymer depends i) on the ions energy and ii) on the polymer *stopping power*. The latter can be modeled by considering the processes involved in the ions energy loss during the interaction with the polymer. The two main contributions to the ions energy loss are represented by the *electronic stopping* and the *nuclear stopping*. The dominant contribution depends on the acceleration voltage of the

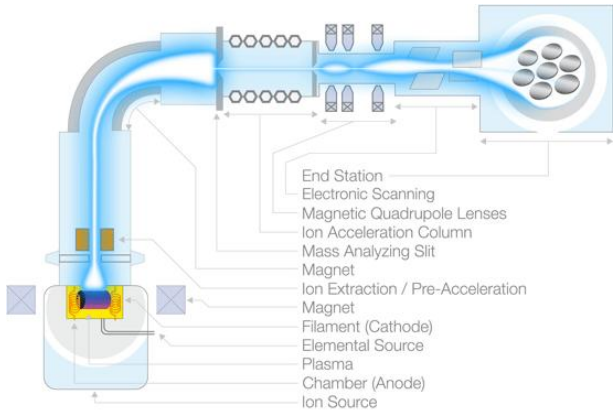

Figure 2.10: Schematic of a typical Ion Implanter

ions. The main contribution for energies below 1-2MeV is due to the inelastic interaction of the ions with the atoms of the polymeric substrate (nuclear stopping), while for larger ion energies, excitation and ionization of the atoms of the substrate take place, leading to electronic stopping. Implantation in elastomers can be achieved for very low ion energies, in the range between 2keV and 10keV [106] obtaining penetration depths between few nanometers up to few tens of nanometers. In this regime nuclear stopping is the main responsible for the ions energy loss.

Ion implantation in elastomers is extensively studied and exploited for the fabrication of electrodes for elastomeric actuators [107, 108, 57, 106]. A Filtered Cathodic Vacuum Arc (FCVA) in which a metal target is vaporized by high-voltage pulses, produces a plasma containing metal ions, undesired nanoparticles and electrons. Metal ions are selected by a magnetic field and accelerated towards the polymeric substrate where they get implanted with doses ranging between $0.9 \cdot 10^{16}$ and $7 \cdot 10^{16} at/cm^2$ in order to reach a good conductivity [108]. It is worth noting that electrically charged atoms are implanted in a polymeric substrate behaving like an insulator, leading to a polymer charging, mainly in the first stages of the implantation process, and causing deformations in the nanocomposite material. Polymer charging is limited by dissipation of electrical charges across the sample once the conductive percolation threshold is reached (at a minimum dose of $1.5 \cdot 10^{15} at/cm^2$ [106]). Metal ions inside the elastomer diffuse and aggregate, forming metal nanoparticles whose size can not be directly controlled.

Reflectivity in ion implanted materials is not widely studied and only few works [109, 110] consider the problem of ion implanted glasses. In these works reflectivities up to 40% are achieved with doses larger than $4 \cdot 10^{16} at/cm^2$, insufficient for the fabrication of reflective optical devices. Also Rosset et al. [19, 111] considered the optical properties of ion implanted PDMS for the fabbrication of arrays of tunable lenses, obtaining a transmittance not below 60% (and thus reflectivities not larger than 40%, as in the previous case).

The main limitation for the achievement of higher reflectivities in ion implanted elastomers is the dramatic increase of the surface roughness following the implantation process. The nuclear interaction of ions with the polymer atoms during nuclear stopping leads to sputtering, local stress modification, charging and heating of the polymer itself [20, 108]. PDMS surface is extremely smooth (RMS roughness below 2nm [112]) but increases up to approximately 100nm after Titanium or Palladium ion implantation at low

energies (5keV) [107]. As seen in the requirements needed for reflective elastomeric optical devices, roughness is a fundamental parameter that must be controlled in order to avoid light scattering. As shown in Figure2.3, the scattered light fraction ranges between 50% and 60% for incident angles up to 30° in the case of a roughness of 40nm.

Furthermore a much larger increase of the nanocomposite stiffness (more than two orders of magnitude) is observed respect to chemically synthesized nanocomposites and Guth's theoretical expectations. The high energies involved in ion implantation, dissipated by the polymer nuclear stopping, cause the breakage and carbonization of the elastomeric chains. Carbonization consists in the breakage of bonds between hydrogen and carbon of the PDMS methyl groups, leading to an increase of carbon atoms concentration in the whole nanocomposite material. As a consequence, the chemical modification of the polymeric chains leads to a deterioration of the physical and mechanical properties of the polymer itself. This hypothesis is supported by the *molecular theory of rubber elasticity* [113] stating that the elasticity of a rubber-like polymer does not depend on the polymeric chains interactions or arrangement, but only on the molecular composition of the chains.

From these considerations it is clear that ion implanted elastomers do not represent optimal materials for the fabrication of reflective optical devices and imaging purposes, as stated in [19], because of issues concerning both the optical quality of resulting materials (reflectivity and light scattering) and mechanical properties.

2.5.3 Supersonic Cluster Beam Implantation (SCBI)

Recently *Supersonic Cluster Beam Implantation* (SCBI) of low energy electrically neutral metal nanoparticles in soft polymers was developed by our group [114, 115] and exploited for the effective fabrication of highly deformable and stretchable nanocomposite-based electrodes [21]. Successful results obtained in the field of stretchable electronics suggest the exploitation of SCBI as effective nanocomposite synthesis technique for elastomeric optical devices as well.

As it will be extensively described in the next chapter, nanoparticles energies involved in this process ranges between tenths and few eV/atom, thus avoiding the polymeric chains breakage occurring for ion implantation because of nuclear stopping. As a result SCBI overcome the drawbacks of ion implanted elastomeric optical devices in terms of polymer deterioration, surface roughness and thus optical quality of the nanocomposite surface, while achieving reflectivities required for elastomeric optical devices, not obtainable by chemical synthesis approaches. The increase of the Young modulus due to the loading of the elastomeric matrix typical of nanocomposites synthesized by chemical techniques is here overcome by concentrating the implanted nanoparticles in an extremely thin superficial layer, not considerably affecting the elasticity of the whole material.

CHAPTER 3

Supersonic Cluster Beam Implanted nanocomposites

3.1 Supersonic Cluster Beam Deposition (SCBD) and SCBI

SCBI derives from a technology developed in the last decade for the deposition of nanostructured thin films on rigid substrates and called *Supersonic Cluster Beam Deposition* (SCBD) [116]. The low nanoparticles kinetic energy and the substrate properties play a fundamental role in the production of porous nanostructured metal thin films. According to molecular dynamics simulations [117] if the ratio between kinetic energy per atom of the metal cluster E_k^{at} and the cohesive energy between the cluster and the surface E_{coh}^{cl} is much lower than unity, the metal nanoparticles are not fragmented upon impact with the rigid surface and the nanostructure preserved, as shown in Figure3.1

The low deposition energy proper of SCBD and the consequent maintaining of the nanostructure upon deposition on hard substrates have effects, for example, on the electric properties of porous deposited thin films [119, 120] and exploited in different applicative fields: electrodes for supercapacitors [121, 122], humidity [123] and gas sensors

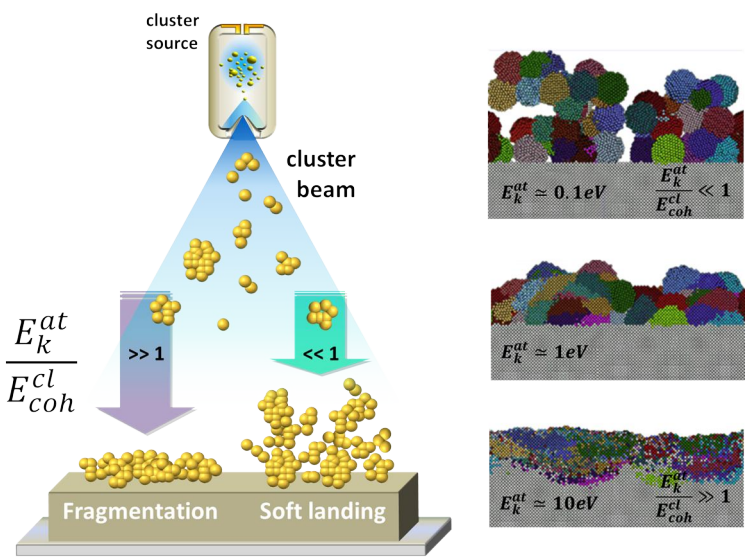

Figure 3.1: Left: schematic representation of the two different (high and low-energy deposition) regimes related to clusters impact on a rigid substrate substrate [118]. Right: molecular-dynamics simulations of thin-film growth by cluster impact at different energies [117].

[124] among them. Porosity of metallic nanostructured thin films also affects the wettability of deposited substrates [125] and helps in improving cell adhesion [126], useful for the fabrication of systems for diagnostics.

Recently *softer* substrates such as SU-8 or PMMA were used and penetration of metal nanoparticles observed. In particular electrical transport properties were analyzed and exploited for the fabrication of deformable electronic devices [114, 115]. More interesting are the results of Supersonic Cluster Beam Implantation of metal nanoparticles in PDMS [21] for the fabrication of highly stretchable elastomeric electrodes. The excellent resilience properties obatined by SCBI metal-elastomer nanocomposites represent a breakthrough in the field of stretchable electronics. Moreover the biocompatibility of PDMS is preserved by the low-energy implantation process and makes SCBI an ideal technique for the fabrication of implantable soft electrodes for neurostimulation. The results on stretchable electrodes fabricated by SCBI are published in the paper *Highly Deformable Nanostructured Elastomeric Electrodes With Improving Conductivity Upon Cyclical Stretching* reported at the end of this chapter.

3.2 Working principle of Supersonic Cluster Beam Implantation

Supersonic Cluster Beam Implantation (SCBI) is a novel technique for the implantation of low-energy electrically neutral nanoparticles in soft polymers [21]. The electrical nature and low kinetic energy (approximately four orders of magnitude lower than ion implantation) of the nanoparticles avoid charging, carbonization and heating of the elastomer. Supersonic Cluster Beam Implantation is a high vacuum process comprising three main steps:

1. Metal nanoparticles are synthesized by a cluster source.

2. The flow of an inert gas (also called *carrier gas*), drags the nanoparticles out of the source and passes through a set of *aerodynamical lenses* aiming to collimate the cluster beam.

3. The energy gained by the nanoparticles in the previous step is sufficient for their penetration inside a polymeric matrix, kept on a sample holder inside a second differentially pumped vacuum chamber (*deposition chamber*), separated from the expansion chamber by an electroformed *skimmer*.

A schematic view of the SCBI apparatus is reported in Figure3.2.

3.2.1 Supersonic Expansion

The mix of inert gas and neutral metal nanoparticles produced by the cluster source is extracted by a difference of pressure between the source and the vacuum pumped in the expansion chamber to which the source is attached. The high vacuum is necessary for the achievement of the *molecular regime* in which the gas and cluster beam velocity behave according to the kinetic theory of gases without further approximations. In particular in a Supersonic Cluster Beam Implantation apparatus the difference between the gas pressures in the expansion chamber P_{exp} and in the source P_{source} is such to satisfy the following condition:

$$\frac{P_{exp}}{P_{source}} \leq 0.478 \tag{3.1}$$

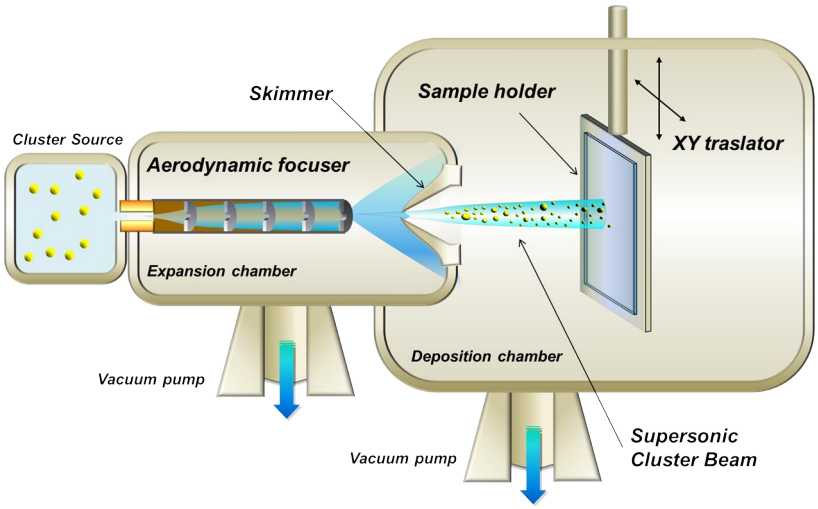

Figure 3.2: Schematic view of a SCBI apparatus

under this condition the gas expansion is *supersonic* [116]. The term *supersonic* relative to gas atoms or metal clusters in vacuum is critical and requires further clarification. A particles beam is said *supersonic* when the particles velocity in the direction of propagation of the carrier gas is greater than the speed sound would have in the gas carrier itself. In a supersonic beam the particles kinetic energy is all concentrated in the propagation direction, avoiding brownian motion of the particles due to thermal energy and thus further cluster aggregation. The clusters extracted from the source thus maintain their properties until the implantation in the polymeric substrate [127].

Nanoparticles undergoing supersonic expansion are characterized by an increase of the distribution of their radial velocity from the center of the beam (where it is null) to the outer regions, and thus by a high divergence. As already seen for coating techniques in section 2.4.2 the divergence of the metal clusters is critical for the patterning of the polymeric substrate or the homogeneous metallization of three dimensional structures, like the grating grooves, because of the so-called *shadowing effect*. The divergence of a cluster beam can be reduced by exploiting the different behavior of particles with different size (and so with different *inertia*) when subjected to an aerodynamical expansion. Small nanoparticles having a sufficiently small inertia are able to accurately follow the gas stream, while large particles trajectories are poorly affected by the gas expansion. This behavior is exploited in the *aerodynamic focuser*, installed between the cluster source and the expansion chamber and through which the mix of carrier gas and nanoparticles expands. Its working principle is schematically presented in Figure3.5.

The aerodynamic focuser consists in a set of steel disks, called *aerodynamic lenses*, through which the gas passes, undergoing subsequent expansions and compressions. The large curvature of the gas streamlines strongly affect the trajectories of the nanoparticles with different inertia. Small nanoparticles follow the gas stream and are expanded with a large divergence at the exit of the focuser, large particles are not able to follow the gas and are trapped in the focuser while intermediate particles deviate from the gas streamlines and concentrate on the focuser axis, resulting in a highly focused beam. The discriminant parameter quantifying the effect of particles inertia is the *Stokes number*,

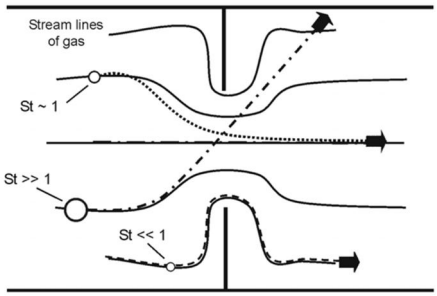

Figure 3.3: Detailed scheme of the effect of nanoparticles inertia when dragged through a small aperture by the carrier gas expansion.

defined as [128, 129]:

$$St = \tau \frac{v}{d} \tag{3.2}$$

where v is the clusters mean speed, d the diameter of the drill in the aerodynamic lens and τ the *relaxation time*, representing the characteristic time the particle takes to change its trajectory and calculated as:

$$\tau = \frac{d_p^2 \rho_p C_c}{18\eta} \tag{3.3}$$

where d_p is the diameter of the nanoparticle, ρ_p its density, η the viscosity of the gas. the Cunningham factor C_c corrects the formula for sub-micrometric particles and depends on the free mean path of the gas atoms and on the particle diameter. The cluster beam exiting the aerodynamic focuser is characterized by unitary Stokes number particles at the center and by particles with decreasing Stokes number towards the borders. So the aerodynamic focuser acts also as a particles size selector, filtering only the particles with a given size and speed. The high collimation (divergence lower than 1 degree) of the cluster beam exiting the aerodynamic focuser allows the use of *stencil masks*, not in direct contact with the polymer surface, for the micropatterning of the elastomeric substrate with a high lateral resolution [116, 22], avoiding the use of chemicals needed for the development of lift-off masks and the shadowing effect typical of traditional coating techniques like PVD.

3.2.2 Implantation in soft polymers

Clusters accelerated in a supersonic regime by the carrier gas expansion gain an energy of approximately 0.5-2.0eV/atom, sufficient for their implantation inside the polymeric matrix but not in hard substrates like glass or silicon. The local decrease of the polymer density upon implantation of the first nanoparticles suggest an easier implantation of further nanoparticles at higher penetration depths thanks to the *clearing the way* effect already observed for ion implantation in hard substrates [130, 131, 132] and can be considered one of the key ingredients of the implantation mechanism in SCBI.

The low kinetic energy gained by the nanoparticles during the supersonic expansion guarantees their implantation in elastomers while maintaining the chemical and physical properties of the elastomeric substrate unaltered. Considering the number of atoms N_{at} reaching the polymer surface per second, the surface power density P_{surf} for cluster implantation can be calculated as $P_{surf} = N_{at} \cdot E_k$, where E_k is the kinetic energy of the

atoms. The power density is of the order of some $\mu W \cdot cm^{-2}$ in the case of SCBI, not sufficient for a detectable heating of the elastomeric substrate above RT. As a comparison, the power density for ion implantation is much larger than SCBI, of the order of tenths of W [133].

3.2.3 Equivalent thickness and filler volume fraction

The determination of the amount of nanoparticles implanted in the polymer by SCBI is not trivial. In PVD or ion implantation directly measurable parameters like the deposition thickness or the implanted atoms dose are respectively used. In SCBI however metal is implanted in the polymer, thus the concept of deposited thickness has no sense. The measure of the *equivalent thickness* represents an effective way for the determination of the amount of implanted nanoparticles in the polymeric matrix. A half-masked hard substrate (silicon or glass) is placed next to the polymeric substrate to implant, intercepting the same amount of nanoparticles implanted in the elastomer. Nanoparticles reaching the hard substrate are deposited on its surface instead of getting implanted, leading to a two-dimensional growth of a nanostructured layer on the non-masked free substrate surface. The difference of height between the deposited and the masked hard substrate regions, measured with a profilometer or an AFM, defines the *equivalent thickness* t_{eq}. Equivalent thickness can be also monitored *in situ* by a quartz microbalance, useful for the live control of the implantation process but whose measured value does not directly coincide with the equivalent thickness measured *after* the implantation process on the rigid substrate, because of the porosity typical of nanostructured deposited films, as further discussed in section 3.1.

From the measure of the equivalent thickness and the penetration depth obtainable by TEM images the *filler volume fraction* f of the nanocomposite can be obtained, defined as the ratio between the total volume of the metal clusters implanted (the filler) $V_{cluster}$ and the total volume of the nanocomposite V_{nc}:

$$f = \frac{V_{cluster}}{V_{nc}} \tag{3.4}$$

The non-trivial distribution of the nanoparticles inside the nanocomposite makes the filler volume fraction difficult to measure. If a uniform nanoparticles distribution inside the nanocomposite is assumed, the filler volume fraction can be rewritten, in first approximation, as follows:

$$f = \frac{t_{eq}}{d_{nc}} \tag{3.5}$$

where d_{nc} represents the maximum penetration depth of the nanoparticles in the polymer matrix.

The filler volume fraction is important in determining the macroscopic physical properties of the whole nanocomposite. Considering the electrical properties,the knowledge of the volume fraction is important in order to model the *percolation curves* and so to extract physical parameters describing the electrical behavior of the metal-polymer nanocomposite [21, 118]. The volume fraction also represents a critical parameter for the description of the light absorption response of the nanocomposite, as it will be shown in part III of the present work.

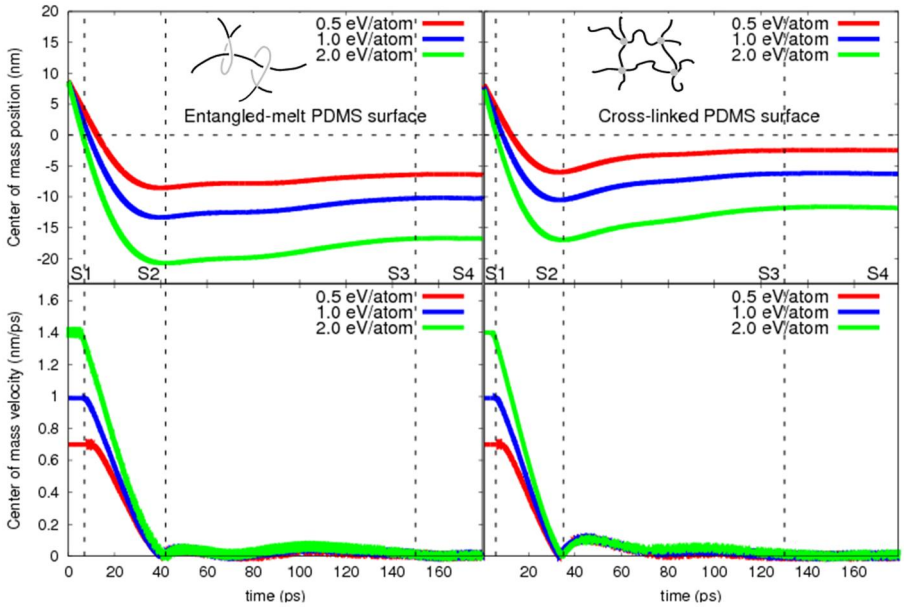

Figure 3.4: Vertical trajectories (top graphs) and velocity (bottom graphs) of the nanoparticles with different kinetic energies in the entangled melt (left) and cross-linked (right) polymeric substrates (from [134]).

3.2.4 Molecular dynamics simulations of SCBI in PDMS

The implantation mechanism of electrically neutral metal nanoparticles by SCBI in Polydimethylsiloxane (PDMS) was theoretically and extensively studied by means of molecular dynamics simulations [134]. The PDMS substrate was simulated with a force field accounting for all the possible vibrational and rotational modes of the PDMS molecules subjected to a 9-6 Lennard-Jones potential and in two different configurations: *entangled melt* and *cross-linked*. Entangled melt polymer consists in 100 monomers chains reciprocally twisted to form the polymeric matrix, while the cross-linked polymer consists in polymeric chains covalently bonded by means of cross-linking molecules (Tetrakis (dimethylsiloxy) silane in the case of PDMS). The simulated PDMS substrates were sufficiently large for an efficient dissipation of the pressure waves generated upon the cluster impact and stabilization of the cluster position inside the substrate. The substrate was fixed at the bottom and thermalized with a Nosé-Hoover thermostat at 300K.

Metal clusters, with a diameter of 3nm, are shot toward the polymer at energies of 0.5eV/atom, 1eV/atom and 2eV/atom, in order to study the effect of the cluster energy on the implantation process. The trajectories and velocities of the particle along the vertical direction were recorded and plotted in Figure3.4.

Four phases in the cluster implantation process, named S_1, S_2, S_3 and S_4, can be well distinguished. The response of the polymer after the implantation, both in the entangled melt and the crosslinked substrate, dominate the behavior of the metal particle after its implantation. During step S_1 the cluster moves freely in vacuum with a linear uniform velocity, depending on the implantation energy, before reaching the polymer surface. During step S_2 the cluster impacts on the polymeric surface and gets implanted, loosing its kinetic energy because of the friction forces between the nanoparticle and the

PDMS matrix (the penetration depth reaches its maximum and the velocity decreases to zero). In step S_3 the response of the PDMS takes place: the PDMS is compressed upon the cluster impact, the pressure wave reaches the fixed polymer atoms at the bottom of the simulation cell and is reflected back to the surface. The nanoparticle undergoing the reflected pressure wave is pushed upward toward the surface and the penetration depth slightly decreases. A stable configuration in which the penetration depth remains unchanged and the cluster velocity reaches a null value is achieved in step S_4.

The effect of the implantation energy is clear in Figure3.4: by increasing the cluster energy the penetration depth increases as well and the S_2 and S_3 steps are longer, as expected. More interesting the differences between the entangled melt and the crosslinked substrates. In the latter case the penetration depth is smaller and the polymer response after implantation stronger. This is compatible with the breakage of bonds between the polymeric chains in the case of the crosslinked substrate or their untwisting in the entangled melt polymer. The bonds in crosslinked polymers are mainly covalent and 8% more than the entangled melt configuration, in which the polymeric chains are dispersed and the bonds are due to much weaker electrostatic forces. The penetration depth vs. implantation energy follows a linear trend both in the case of entangled melt and the crosslinked configurations, with a slope of 7nm/eV and 6nm/eV respectively. Moreover a *swelling* of the polymer surface is observed in both cases and for all the implantation energies. In the case of the crosslinked matrix the swelling is approximately 3nm independently of the implantation energy, larger than in the case of the entangled melt polymer, because of the larger amount of broken covalent bonds and to a stronger elastic response of the substrate.

The formation of pressure waves and the breakage of bonds between the polymer chains are not the only effects due to cluster implantation in soft polymers. A local heating of the polymer around the implanted particles and of the particle itself is observed. Polymer atoms next to the particle are subjected to an increase of temperature from 300K up to 600K but the mean temperature increase in the the first superficial 50nm thick slab of the polymer is approximately 30-50K, not affecting its global physical properties.

Cluster implantation in soft polymers also creates a crater, slowly recovered in time due to chains rearrangement. Surface morphology of the implanted polymer is affected by the formation of these craters. Experimental measures of the surface roughness were compared with the depth of the craters and the roughness measured by simulated AFM experiments, as explained in [22].

In molecular dynamics simulations only a single particle implantation is considered. A multiparticles implantation simulation requires a much heavier computing effort (for the simulations analyzed 65536 CPU hours were required for each impact). However the implantation of the first nanoparticles facilitates the implantation of further particles thanks to the clearing the way effect previously discussed.

3.3 Supersonic Cluster Beam Implantation setup

In section 3.2 a general description of the working principle and main advantages of the SCBI respect to other nanocomposite synthesis techniques were given, without any detail on the cluster source, since SCBI is compatible with different available sources, and of the SCBI apparatus.

The SCBI apparatus used in this thesis work is equipped with a *Pulsed Microplasma Cluster Source* (PMCS) [135, 116] for the synthesis of metal nanoparticles. Metal atoms are sputtered by a metal rod through ionized inert gas atoms, and aggregate inside the same gas forming electrically neutral metal nanoparticles. A more detailed description

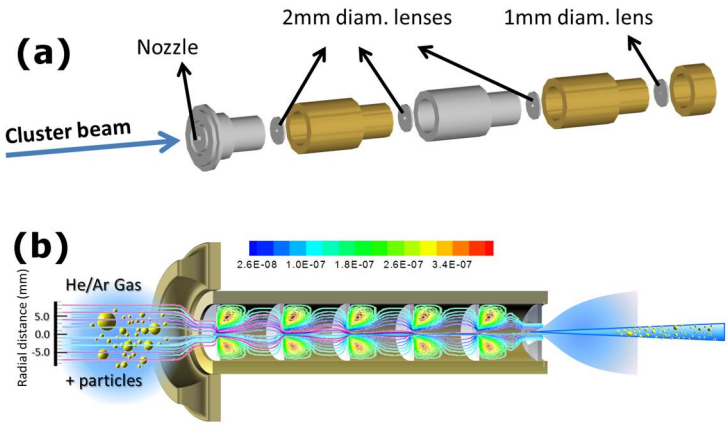

Figure 3.5: (a) Exploded view of the aerodynamical focuser used in the SCBI apparatus. (b) Scheme of the streamlines of nanoparticles with $St \simeq 1$ through subsequent focuser stages.

of PMCS will be given in the following. The mix of gas and nanoparticles then expands in the expansion chamber, to which the PMCS is connected, through the aerodynamical focuser. The high vacuum kept in the expansion chamber (approximately $10^{-6} torr$) by a turbomolecular pump having a flow rate of $1900 l \cdot s^{-1}$, is responsible for the extraction and supersonic acceleration of metal nanoparticles toward the elastomeric substrate. The aerodynamical focuser, schematically reported in Figure3.5 is made of a series of cylinders (the focuser *stages*) separated by *aerodynamical lenses*. These lenses consist in steel disks with a central 2mm diameter drill (1mm diameter for the last lens). The abrupt changes of direction of the gas-nanoparticles mixture expanding through each aerodynamical lens allow both a selection of the nanoparticles with a certain size (in particular nanoparticles characterized by $St < 1$, as extensively discussed in section 3.2.1) and their collimation on the axis of the focuser.

The central part of the collimated cluster beam is intercepted by a 2mm small aperture for the further spatial filtering of the nanoparticles. This device, called *skimmer* is characterized by a low conductance and a swallow tail shape in order to keep a differential vacuum between the expansion and the deposition chambers, and limits the supersonic shock waves caused by the supersonic expansion respectively. Supersonically accelerated gas atoms exiting the aerodynamical focuser expand with a high divergence, dragging metal nanoparticles with $St \ll 1$. As a consequence only the central part of the beam, consisting of metal nanoparticles with $St \simeq 1$ is able to pass through the skimmer and to enter the deposition chamber.

Deposition chamber is kept at high vacuum (approximately $10^{-5} torr$ by a second turbomolecular pump with a flow rate of $500 l \cdot s^{-1}$. Here nanoparticles get implanted in the elastomer, kept on a sample holder connected to a computer-controlled manipulator and able to move orthogonally to the cluster beam direction for the implantation on large areas. The sample holder is equipped with a quartz microbalance for the real-time monitoring of the implantation rate and, if needed, with a heater for the controlled heating of the sample during the implantation process.

The section of the nanoparticles beam intercepted by the sample holder in the deposition chamber consists in a circle with a diameter of few centimeters. This circular spot is inhomogeneous, since the nanoparticles density decreases from the center to the

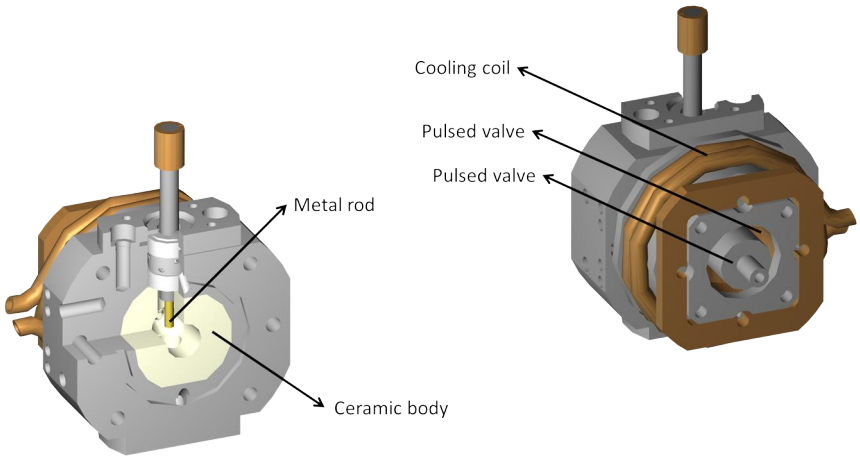

Figure 3.6: Front and rear schematic representation of the sectioned PMCS.

borders. The movable sample holder on which the elastomeric substrate is mounted guarantees a homogenous implantation on larger areas, up to 20x20cm^2. The relative path followed by the nanoparticles beam through the movement of the substrate is repeated many times until the achievement of the wanted equivalent thickness throughout the entire sample.

3.3.1 Pulsed Microplasma Cluster Source (PMCS)

The source (depicted in Figure3.6) consists in a ceramic body with a cylindrical cavity and two openings at the opposite sides of the cavity. At the entrance a solenoidal pulsed valve allows the injection of an inert gas, expanding and concentrating around a rod composed of the wanted nanoparticles material (a conductive metal or metal alloy) inserted in the source through a third aperture. Immediately after the valve, a drilled copper disk acts as counter electrode in the functioning mechanism of the source. At the opposite opening of the ceramic body, a *nozzle* characterized by a low conductance is needed in order to maintain a differential pressure between the source and the vacuum chamber to which the source is applied. The whole system is inserted in an aluminum support electrically connected to the copper disk and grounded. A motorized mechanism is connected to the aluminum support for the rotation of the rod during the operation of the source.

Like most of the cluster sources, the working principle of the PMCS can be divided in four phases, as shown in Figure3.7: gas injection, vaporization of the metal target, nanoparticles condensation and nanoparticles extraction. The pulsed valve is opened for few hundreds microseconds, letting the inert gas (typically Argon at a pressure of 40-50 bar) entering the ceramic cavity and concentrating around the metal rod, because of aerodynamical effects due to the shape of the cavity and the rod diameter. After 80-100μs from the valve opening, an electrical discharge of about 800V between the rod (acting as a *cathode*) and the copper disk (the *anode*) with a duration of some hundreds microseconds takes place. The discharge ionizes the gas atoms that are thus attracted by the biased metal rod and gain sufficient energy to *sputter* metal atoms from the rod itself. Sputtered metal atoms thermalize and condensate in the gas forming *electrically*

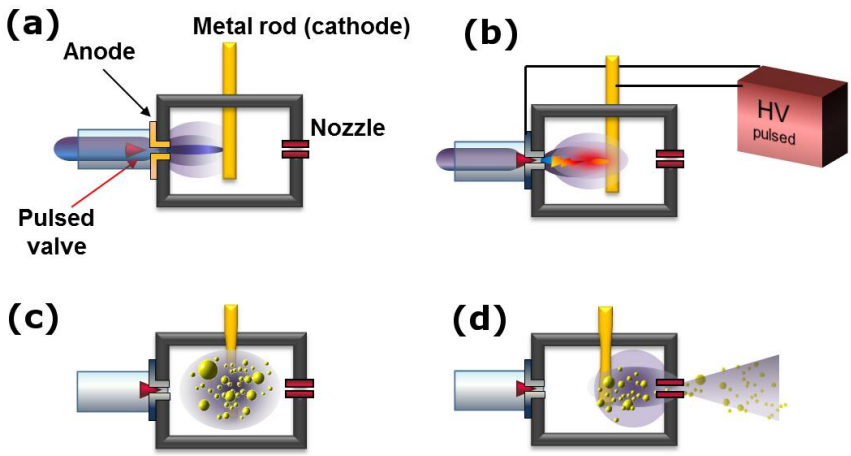

Figure 3.7: PMCS working principle. The inert carrier gas is injected in the source ceramic cavity (a) and concentrates around the metal rod. A high voltage is applied between the rod and the anode, and an electrical discharge sputters metal atoms from the rod (b). The metal atoms thermalize and aggregate in the gas forming electrically neutral metal nanoparticles (c) and the mix of gas and nanoparticles is extracted by a difference of pressure with the vacuum chamber to which the source is applied (d).

neutral metal nanoparticles, with sizes ranging from few up to tens nanometers, dispersed inside the high pressure inert gas. The source is applied to a high vacuum chamber and the difference of pressure, kept by the low conductive nozzle at the exit opening of the source, causes the expansion of the gas dragging the synthesized nanoparticles. The whole process is repeated at a frequency varying between 1 and 10Hz, producing high intensity nanoparticles pulses.

The working parameters of the source are extremely important and must be adjusted in order to control the nanoparticles sizes and extraction energy according to the rod material. During the source operations the rod is kept in rotation in order to guarantee a homogeneous erosion and a regular and constant functioning of the source, critical for synthesis of nanocomposites with optimal and repeatable properties.

Similar cluster sources are available, differentiating only in the metal vaporization mechanism. In Pulsed Laser Vaporization Sources (PLVS) [136, 137] a laser beam impinging on the metal target erodes metal atoms in a limited area, ensuring the time stability of the process. Intensity of the cluster beam is the major problem. In Pulsed Arc Cluster Ion Sources (PACIS) [138] metal atoms are extracted from the target by means of an arc discharge, allowing a larger intensity. The strong modification of the target geometry and gas dynamics affects the time stability (see [135] and references therein). In the PMCS the gas concentrated around the metal rod allows localizing the discharge in a well defined region of the target, aiming to achieve both intensity typical of electric arc based sources and the time stability of laser based sources.

3.4.1 Size distribution of metal nanoparticles

The size distribution of the nanoparticles passing through the skimmer and implanted in the sample was investigated by TEM. Metal nanoparticles (in particular silver nanoparticles used for the metallization of elastomeric optical devices in this work) were deposited on a Formvar-coated nickel TEM grid metallized with a Carbon submonolayer for three seconds in order to obtain isolated and uniformly dispersed nanoparticles on the grid. During the analysis of the images only particles with an eccentricity greater than 0.7 were considered, in order to exclude cluster aggregates. The results for silver, presented in Figure3.8, show a median nanoparticle size of $9.05 \pm 0.53nm$. A similar characterization was carried for gold nanoparticles in [22]. In both cases nanoparticles size distribution is small enough to avoid particles scattering phenomena.

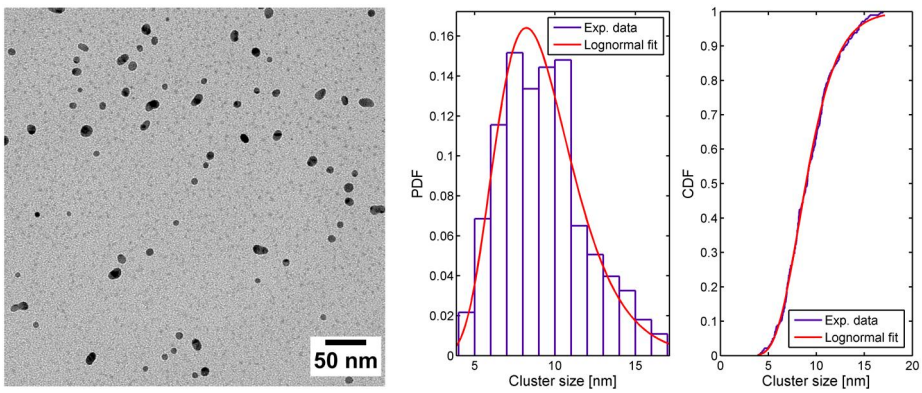

Figure 3.8: From left to right: TEM image of Ag nanoparticles deposited on the Formvar layer, Probability distribution function (PDF) of the nanoparticles count and the corresponding Cumulative Distribution Function.

3.4 Morphological and mechanical characterization of SCBI Ag/PDMS nanocomposites

Morphological and mechanical properties of metal-polymer nanocomposites synthesized by SCBI are analyzed in light of the requirements needed for elastomeric optical devices, mainly in terms of light scattering, surface roughness and stretchability (or elasticity).

3.4.2 Penetration depth of metal nanoparticles

The penetration depth of metal nanoparticles in PDMS can be investigated by TEM. PDMS substrates are implanted for few seconds by SCBI, then cut by Cryoultramicrotomy in approximately 100nm thick slices and laid on a Formvar-coated TEM grid. Silver nanoparticles, used in the following of this work for elastomeric optical devices, are well visible in the TEM images (like, for example the one shown in Figure3.9) and are implanted up to a penetration depth of approximately 100nm. A similar characterization for gold nanoparticles was presented in [22]: here a penetration depth of approximately 180nm was observed, independently on the implanted equivalent thickness. The attainable penetration depth is thus similar for different metal nanoparticles and of the order of tens of nanometer.

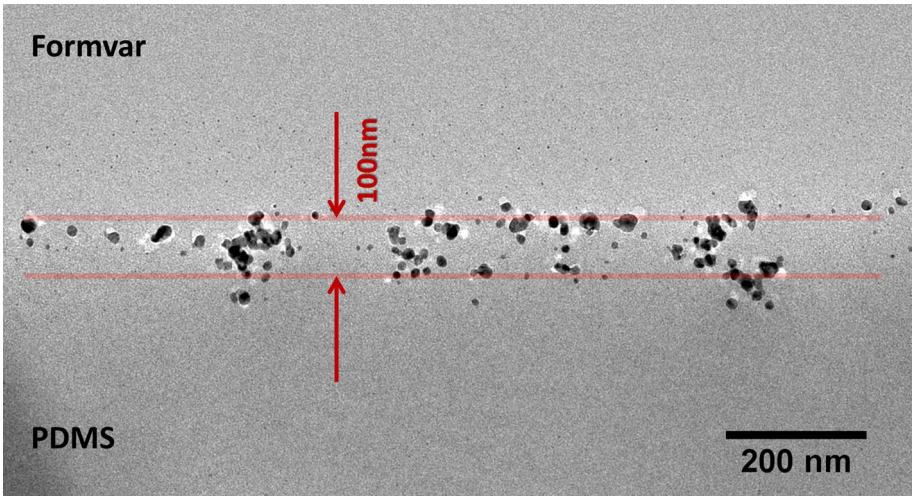

Figure 3.9: TEM image of the Ag/PDMS nanocomposite

3.4.3 Elasticity of SCBI nanocomposites

Preliminary results on the surface Young modulus of the SCBI nanocomposite were obtained by AFM nanoindentation experiments on a nanocomposites library characterized by different equivalent thicknesses (and thus volume fraction) and reported in Figure3.10. The contact region of AFM indentation curves on the nanocomposite surface, acquired with proper spherical micrometric colloidal probes, were analyzed exploiting the Hertz contact model describing the interaction mechanism between a rigid sphere and an elastic surface. The measured Young modulus varies from 2.5MPa of the bare PDMS up to approximately 12MPa for a gold implanted equivalent thickness of 100nm (corresponding to a volume fraction of about 0.20 if the polymer swelling upon implantation is considered), two orders of magnitude lower than in the case of ion implantation. These nanoindentation measurements involve the first hundreds nanometers of the implanted polymer, not considering the remaining part of the PDMS substrate that extends for tens of micrometers. Very preliminary results of the Young modulus obtained by stress-strain simulated experiments on nanocomposite samples (nanocomposite plus supporting PDMS) prepared by molecular dynamics are comparable to the results obtained by AFM mesurements.

The much lower increase of Young modulus achieved by SCBI respect to other higher energy implantation techniques can be explained again with the implantation mechanism occurring in the two cases. SCBI only causes a slight local increase of the temperature of the polymer, leading to *debonding* of the polymeric network. Unlike ion implantation, low energies involved in the SCBI process do not alter the structure and chemical composition of the polymeric chains and thus their elasticity, as predicted by [113]. Therefore the increase of the stiffness observed for SCBI could be explained just by considering the effect of the filler in the polymer, as predicted by Guth equation [88, 89]. As a proof of this hypothesis, preliminary experimental data follow the same trend reported in Figure2.9 and 3.10 for different aspect ratios, as expected because of the formation of aggregates.

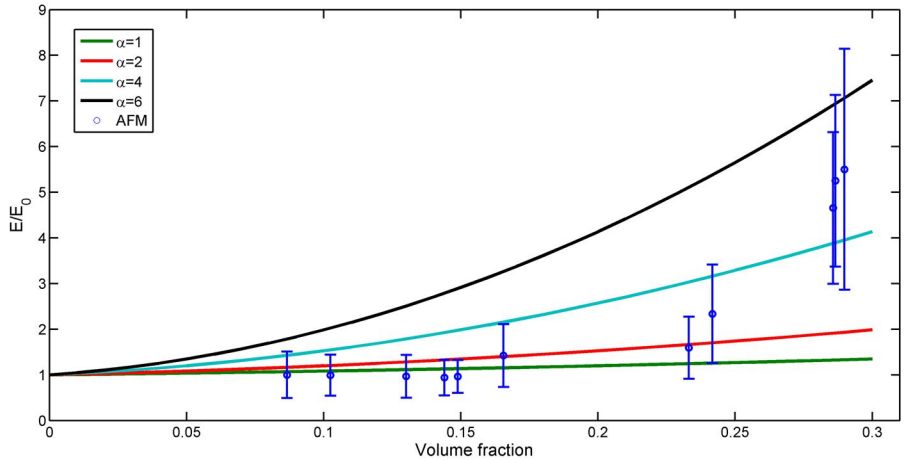

Figure 3.10: Comparison between AFM data and expected data from Guth equation [88, 89] for different filler aspect ratios α.

3.4.4 Surface roughness

Surface morphology is critical for the exploitation of metal-polymer nanocomposites for optical applications. Surface roughness is responsible for the scattering of the impinging light and must be therefore minimized and controlled. Moreover three dimensional sub-micrometric features like the grooves of a diffraction grating must be perfectly reproduced by the metallization process. The effect of SCBI of metal nanoparticles on the morphology of PDMS in which they are implanted was extensively studied in the paper [22] titled *Patterning of gold-polydimethylsiloxane (Au-PDMS) nanocomposites by supersonic cluster beam implantation*, published on *Journal of Physics D: Applied Physics*, entirely reported at the end of the chapter. In this paper PDMS was implanted with gold nanoparticles, however few differences are observed by implanting different metal nanoparticles. Morphological measurements on Ag/PDMS nanocomposites are presented as a comparison

Au/PDMS nanocomposites surface roughness characterized by different equivalent thicknesses was investigated by AFM investigation. The results show an increase of the surface roughness, up to approximately $10nm$ for an equivalent thickness of $100nm$. From an optical point of view this translates to a very low nanocomposite light scattering. Recalling the results of equation 2.3, reported in Figure2.3, a roughness of 10nm is responsible for a constant light scattering less than 6%, slowly decreasing with the light incident angle.

Moreover from the measure of the step between the bare PDMS and the nanocomposite, a swelling of the implanted polymer is observed, as reported by the molecular dynamics simulations. However the swelling phenomenon does not affect the lateral resolution of a patterned region, the gradient remaining less than 1μm in extension. Swelling is supposed to affect the geometry of implanted three-dimensional structures like, for example, the diffractive structure of a grating, but since the sample is homogeneously implanted, the profile remains unaltered, as it will be shown in the next chapter.

These results regard Au nanoparticles with a mean size of $3.9 \pm 1.4nm$ implanted in

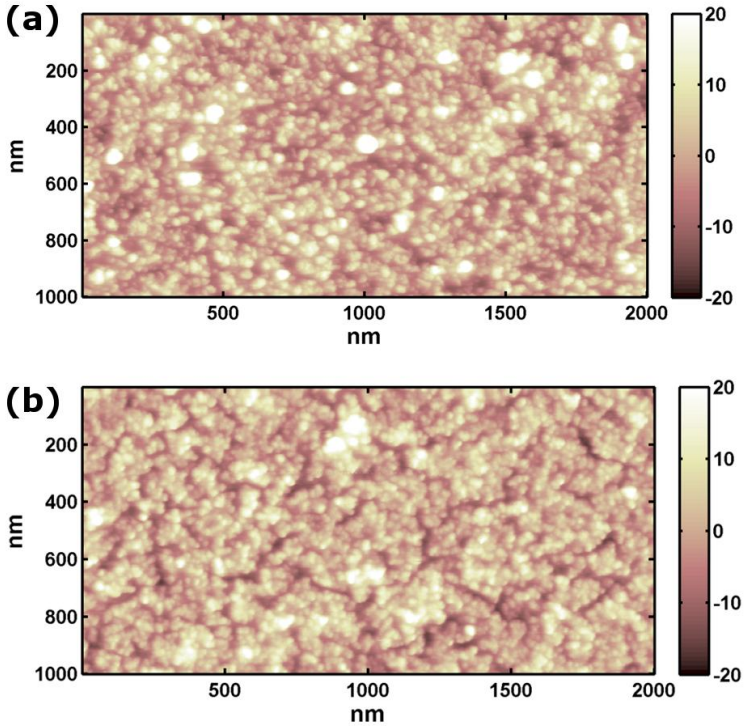

Figure 3.11: $2000\mu m$ x $1000\mu m$ AFM topographic maps of Ag/PDMS (a) and Au/PDMS (b) nanocomposites with comparable equivalent thicknesses (87nm and 96nm respectively).

PDMS. However optical devices considered in the following chapters of this work, are fabricated by implanting Ag nanoparticles, with a larger mean size, in the same polymer. Nevertheless the attainable RMS roughness is similar or *better* than Au/PDMS nanocomposites. The surface roughness of a Ag/PDMS nanocomposite implanted with an equivalent thickness of 87nm was measured by AFM and results in 6.6 ± 0.3nm, much lower than the surface roughness of a Au/PDMS nanocomposite implanted with a similar equivalent thickness ($t_{eq} = 96nm$, roughness 10.1 ± 0.4nm in the case of gold). The topographic maps of the two samples are reported in Figure3.11. According to these results the fraction of light scattered by the Ag/PDMS nanocomposite is even lower (few percents) than in the case of Au/PDMS.

ADVANCED MATERIALS
www.advmat.de

Materials Views
www.MaterialsViews.com

Highly Deformable Nanostructured Elastomeric Electrodes With Improving Conductivity Upon Cyclical Stretching

Gabriele Corbelli, Cristian Ghisleri, Mattia Marelli, Paolo Milani, and Luca Ravagnan**

Many applications in biomedicine, prosthetics, wearable electronics, and robotics require the integration of electronic, optical, and actuation capabilities on soft and conformable polymeric substrates.[1] Much progress has been made in this area, in particular in the fabrication of circuits and devices on flexible substrates[2] and those that utilize mass-production manufacturing processes to produce flexible solar cells,[3] flexible displays,[4] smart clothing,[5] sensors, and actuators.[6,7] For example, Rogers and co-workers recently reported a major achievement towards stretchable and high-performance microelectronics capable of tolerating very large levels of strain by integrating ultrathin silicon-based electronic circuits into elastomeric substrates.[8] This platform was used for the fabrication of smart surgical tools that featured enhanced performances.[9]

Despite these achievements, stretchable electrodes consisting of metallic paths on elastomeric susbtrates are still plagued by drawbacks and failures that prevent their use, especially for biomedical applications. Implantable devices for neurostimulation and neuroprosthetics[10] can strongly enhance their performances and enlarge their field of application by the possibility of printing metallic microcircuits on biocompatible and conformable substrates. Conceivably, the treatment of pathologies including Parkinson's disease, essential tremor, dystonia, chronic pain, treatment-resistant depression, cluster headaches, and epilepsy[11] could benefit significantly from the use of stretchable electrodes.

Efforts to fabricate stretchable metallic circuits and electrodes are concentrated on the direct metallization of polydimethylsiloxane (PDMS), which couples biocompatibility with mechanical properties and machinability suitable for rapid prototyping.[12] At present the metallization of PDMS to produce micrometric and well-defined conductive pathways is obtained by metal vapor deposition (e.g., Au, Ag, Pt, Pd)[13] or metal ion implantation.[14,15] These techniques are in principle quite straightforward, however, in practice, the use of conformable electrodes produced by the former approach is hampered by delamination of the conducting layers even at very low deformations. The use of adhesion layers such as Cr or Ti or the treatment of the PDMS surface with oxygen plasma improve the performance, however the resilience is not adequate for the majority of applications.[13,16] Several attempts have been made to overcome the deterioration of evaporated layers by the deposition of tortuous wave-shaped traces[17] or by the use of prestretched PDMS substrates,[18] but these solutions have considerable limitations in terms of maximum applicable strain, the direction of the tolerable strain, the density of attainable circuits, and scalability.

Better adhesion can be obtained by metal ion implantation where noble metal ions are implanted at 4–10 keV atom^{-1} into a polymeric substrate[14,15] forming a metal–polymer nanocomposite conductive layer below the substrate surface.[14] Stretchable electrodes fabricated by this technique show adhesion and electrical conductivity degradation rates upon cyclical stretching that are substantially superior to evaporated electrodes but, nevertheless, this technique has several drawbacks, since it induces charging and carbonization of the insulating polymeric substrate.

Here we demonstrate that stretchable and compliant electrodes on PDMS can be efficiently fabricated by the implantation in the elastomeric substrate of neutral metallic clusters aerodynamically accelerated by a supersonic expansion. Supersonic cluster beam implantation (SCBI) is an effective method for the microfabrication of conductive circuits on thermoplastic polymers,[19] it is applicable at room temperature (without any heating of the samples), and it does not induce any charging or carbonization of the polymeric substrate. Using SCBI, we fabricated deformable elastomeric electrodes that can withstand deformation of 40% for more than 10^5 cycles and that decrease their resistance upon cyclical stretching.

SCBI consists in directing a highly collimated beam of neutral (i.e., with zero electric charge) metallic clusters (**Figure 1**a) with a size distribution range of 3 nm to 10 nm and kinetic energy of about 0.5 eV atom^{-1} towards a polymeric substrate. Although the kinetic energy per atom of the clusters is four orders of magnitude lower than in the case of ion implantation, clusters (made of several thousand atoms) have sufficient inertia to penetrate into the polymeric target, which is kept at room temperature (RT), and to form a nanocomposite layer, while avoiding charging and carbonization of the polymeric substrate.[19]

Figure 1b,c show transmission electron microscopy (TEM) images of cross sections of a PDMS substrate implanted at RT with Au clusters at corresponding equivalent thicknesses[19] of 35 nm and 210 nm, respectively. Remarkably, the penetration depth of the Au clusters in PDMS (90–136 nm, Figure 1b,c) is approximately twice the penetration depth that was observed for a Pd cluster in poly(methyl methacrylate) (PMMA) at RT (approximately 50 nm[19]). This difference is expected because of the lower hardness of PDMS in comparison with PMMA

G. Corbelli, C. Ghisleri, M. Marelli, Prof. P. Milani
CIMAINA and Physics Department
Università degli Studi di Milano
Via Celoria 16, I-20133 Milano, Italy
E-mail: pmilani@mi.infn.it

Dr. L. Ravagnan
WISE s.r. l.
Via Boschetti 1, I-20121 Milano, Italy
E-mail: luca.ravagnan@wisebiotech.com

DOI: 10.1002/adma.201102463

© 2011 WILEY-VCH Verlag GmbH & Co. KGaA, Weinheim

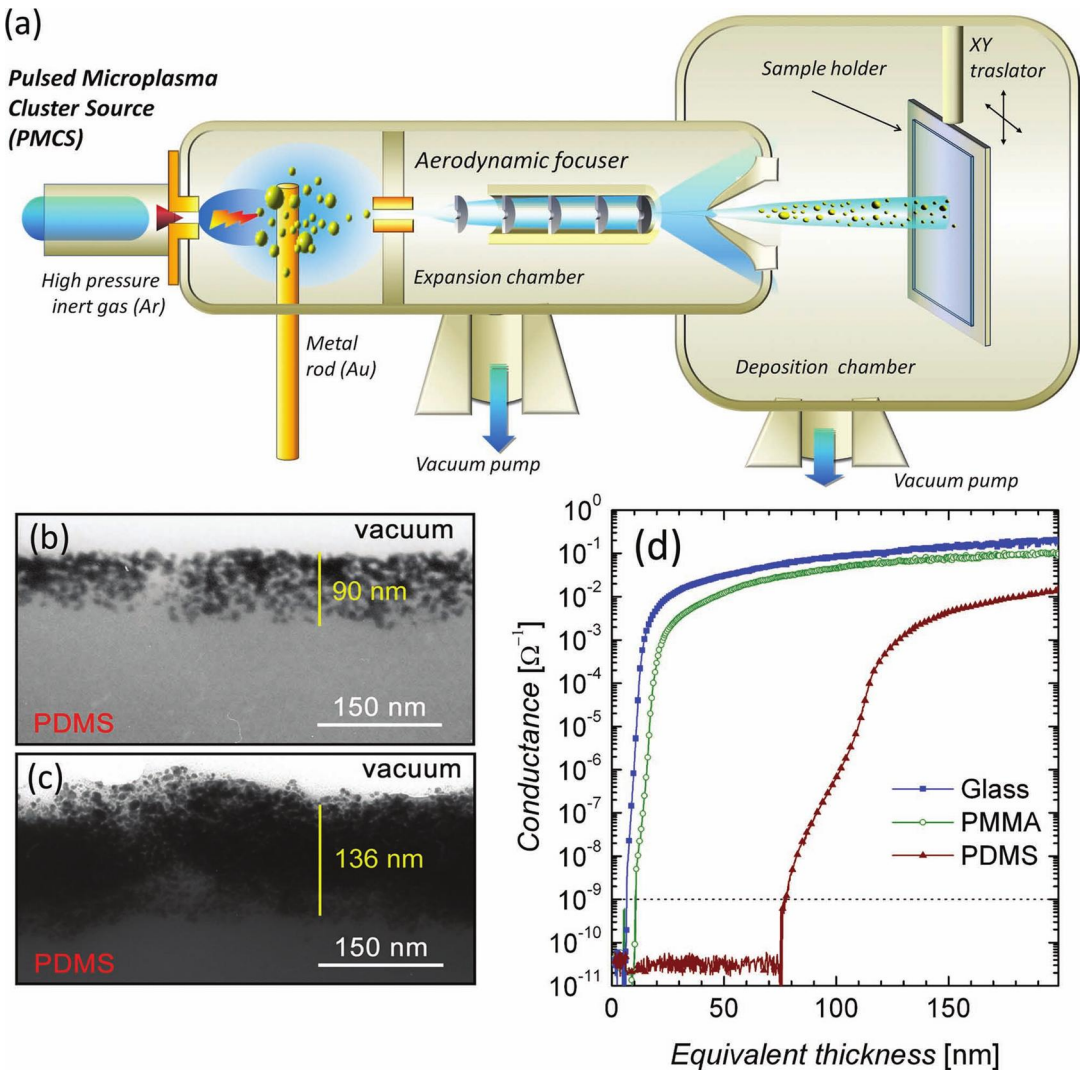

Figure 1. a) Schematic view of the apparatus used for SCBI (not to scale). The collimated supersonic beam of neutrally charged Au nanoparticles (produced by the cluster source, mean cluster size 8 nm) impact the PDMS substrate forming an Au/PDMS nanocomposite layer. b,c) TEM images of cross-sections (cut by cryo-ultramicrotomy, thickness 300 nm) of the produced Au/PDMS nanocomposite samples obtained at RT by implanting an equivalent thicknesses of clusters of 35 nm and 210 nm, respectively. d) Measurement of the evolution of the conductance on three substrates (glass, PMMA, and PDMS) simultaneously exposed to the cluster beam. Measurements are shown as a function of the equivalent thickness, which was measured by a quartz microbalance.[19]

and is furthermore supported by the characterization of the evolution of the electrical transport properties, i.e., the conductance, of the samples as a function of the amount of deposited clusters, i.e., the equivalent thickness. Figure 1d shows the percolating behaviors measured by depositing clusters on three different substrates simultaneously: glass (in which clusters are not implanted), PMMA, and PDMS. As can be clearly seen, on all three substrates the characteristic evolution from insulating to conductive behavior occurs beyond a critical percolation threshold s_c, which is defined here, operatively, as the equivalent thickness at which the sample conductance exceeds 10^{-10} Ω^{-1}.[19] On glass, s_c is about 5 nm, corresponding to a coverage of approximately 50% of the substrate by the clusters, which have a mean size of about 8 nm, and thus consistent with a growth of a cluster-assembled film on the surface of the substrate.[20] In PMMA the percolation is reached for s_c of about 10 nm, clearly indicating the penetration of the cluster in the polymer matrix, consistent with previous results.[19]

© 2011 WILEY-VCH Verlag GmbH & Co. KGaA, Weinheim

ADVANCED MATERIALS
www.advmat.de

Materials Views
www.MaterialsViews.com

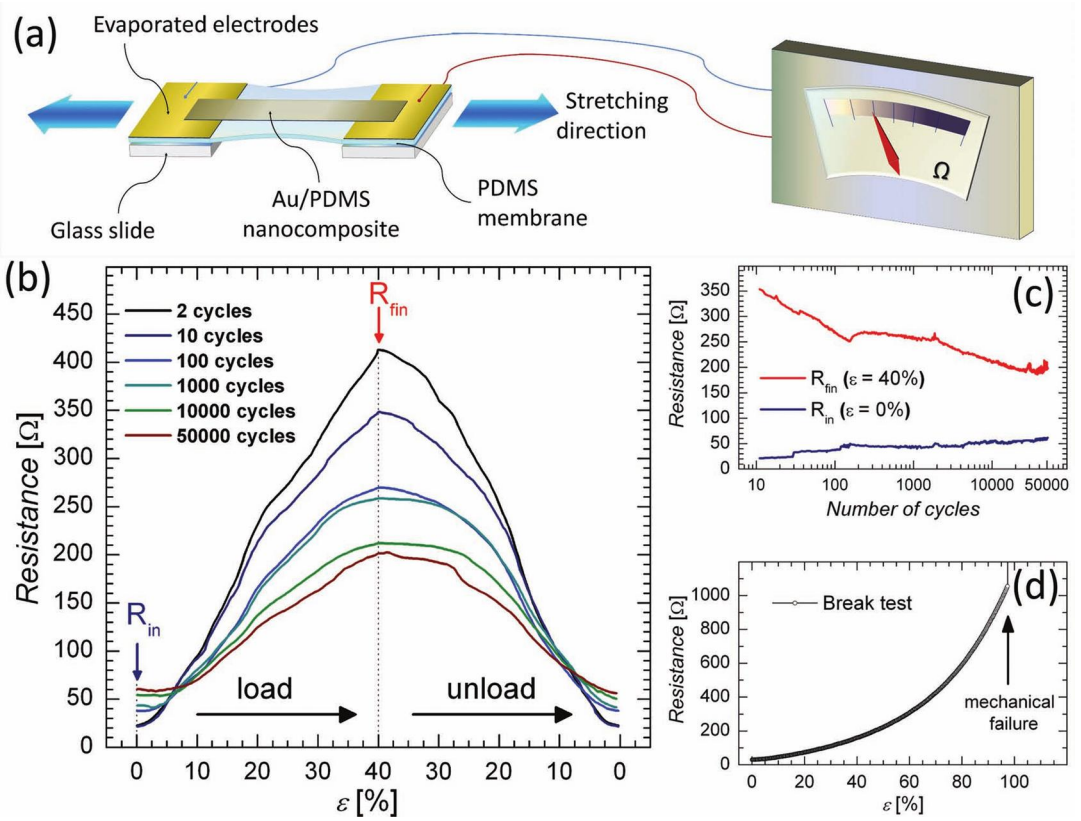

Figure 2. a) Schematic view of the experimental setup used for the characterization of the evolution of the transport properties during uniaxial strain cycles. b) Electrical resistance as a function of applied strain recorded on the Au/PDMS nanocomposite film (size of the suspended portion of the sample subjected to strain: 30 mm wide by 5 mm long) produced by SCBI, during cycle 2, 10, 100, 1000, 10 000, and 50 000 (maximum elongation: 40%). During measuring cycles the samples were stretched at an elongation rate of 20 μm s^{-1}. c) Electrical resistance at 0% strain (R_{in}) and at 40% strain (R_{fin}) as a function of the number of stretching cycle to 40% strain. d) Electrical resistance as a function of applied uniaxial strain. The failure at 97% strain is due to the PDMS substrate mechanically breaking.

Remarkably, on PDMS the film remains insulating up to a s_c value of 75 nm. Qualitatively, a value of s_c that is higher for PDMS compared with PMMA confirms the larger penetration of the gold clusters observed by using TEM. Nevertheless, quantitatively, the s_c value of 75 nm for PDMS would suggest a penetration depth much higher than the observed one. This discrepancy can be understood in light of the fact that at RT gold clusters have a low but not zero mobility in PDMS, which has a glass transition temperature of about –120 °C,[21] and this allows them to aggregate due to an Ostwald ripening process.[22] The same does not happen for PMMA because it has a glass transition temperature above RT. The substantial shift in the percolation threshold can therefore be ascribed to the formation, in the first stages of the nanocomposite growth, of dendritic aggregates of gold clusters in the PDMS matrix. Finally, it is worth noting that the conductance of the PDMS/gold nanocomposite is always lower, by at least one order of magnitude, than the conductance of the surface-deposited film (i.e., on glass), which is consistent with the nanocomposite nature of the material.

We tested the performance of a conductive PDMS/gold nanocomposite obtained by SCBI against extensive uniaxial strain cycles. To do this we produced the nanocomposite film across the gap between two evaporated electrodes on a PDMS membrane (**Figure 2**a, see details in the Experimental Section). The sample was then mounted on a custom-built, computer-controlled, motorized uniaxial stretcher, allowing automatic acquisition of the nanocomposite electrical resistance (R) with cyclic strain (ε). At each strain cycle, the maximum applied strain was 40%. The electrical resistance was recorded during "measuring" strain cycles at an elongation rate of 20 μm s^{-1}, alternating with a series of "fatigue" strain cycles, at a faster elongation rate (200 μm s^{-1}).

Figure 2b shows the resulting stretching cycles recorded during cycle 2, 10, 100, 1000, 10 000, and 50 000 on a representative sample. The same evolution was observed over multiple experiments on different samples.

 © 2011 WILEY-VCH Verlag GmbH & Co. KGaA, Weinheim

During cycle 2 the nanocomposite electrical resistance grew almost linearly from an initial value of 23 Ω (at 0% strain, R_{in}) up to 420 Ω when the maximum strain was reached, i.e., at 40% strain, R_{fin}, recovering its initial value when the strain was released. Remarkably, as the number of strain cycles grew, the increase of R with ε remained monotonous also after 50 000 cycles, maintaining an almost triangular response. This is the first significant departure from the typical behavior observed for evaporated metal films on polymers, where the formation of cracks in the rigid superficial film induces a non-monotonous increase in R with ε after a few thousand strain cycles with maximum applied strain much lower than 40%.[13] Furthermore, the value of R_{in} for the nanocomposite exhibited only a slow increase as the number of cycle increased and, most remarkably, the value of R_{fin} progressively decreased. As shown in Figure 2c, the value of R_{fin} became almost half the initial value after 50 000 strain cycles, which is completely at odds with the usual huge increase (by orders of magnitudes) of R_{fin} observed for evaporated metal films.[13] Those differences can be explained by the nanocomposite nature of the conductive film, where the increase of the R with strain application is mainly due to the increase in the mean distance between the metal nanoparticles, which causes the opening of several percolating paths.[14] Nevertheless, when strain is released the percolating paths are reformed and the electric conductivity is recovered. Moreover, the repetition of uniaxial strain cycles allows the nanoparticles embedded in the nanocomposite, which have a nonzero mobility in the polymer, to progressively reorganize themselves and aggregate, leading to a percolating network that is less affected by the strain and consequently to the decrease of R_{fin}. Furthermore, the nanocomposite is not characterized by the supervening of an abrupt electrical failure at a critical applied strain as is the case for evaporated metal films,[23] but to a progressive increase in R. This is shown in Figure 2d, where a "break test" is performed by subjecting the film to growing strain up to the electrical or mechanical failure of the sample, i.e., the breaking of the polymer membrane. For the tested film, the occurrence of an electrical failure before mechanical failure was never observed and the film could withstand up to 97% strain.

SCBI is not only an efficient method for the production of stretchable and durable metallic circuits but it also functions as a micropatterning tool. By exploiting the high collimation typical for supersonic cluster beams,[24] micrometric patterns can be easily obtained by interposing a stencil mask in front of the PDMS substrate (**Figure 3**a). Figure 3b shows an example of a gold micropattern obtained using a TEM grid that is not in contact with the substrate as a stencil mask. Figure 3c shows the same micropattern under stretching to 35% strain. No delamination is observed, although a few superficial microcracks are present. Scanning electron microscopy (SEM) images showing in detail the cracks formed after the uniaxial stretching of the sample are presented in the Supporting Information and show the superficial nature of the cracks, which influences the electrical conductivity of our material in a marginal way. The fabrication process consists of one step and it does not include any wet chemical treatment, thus avoiding surface contamination.

In summary we have demonstrated a novel fabrication process to obtain metallic electrodes and micropatterns on stretchable substrates. The approach is based on the acceleration of metallic clusters by a supersonic expansion and their implantation in PDMS substrates to form a conductive nanocomposite. The produced structures are characterized by their superior capability to sustain very large deformation with electrical conductance, which improves with cyclical deformation. This approach overcome the many limitations typical of standard metallization approaches, in terms of performances (delamination, etc.) and processing (sample heating, electrical charging, carbonization, use of solvents, and use of adhesion layers). Microfabrication of conductive nanocomposite patterns on elastomers provide new perspectives for stretchable and conformable electrodes for biomedicine and smart prosthetics.

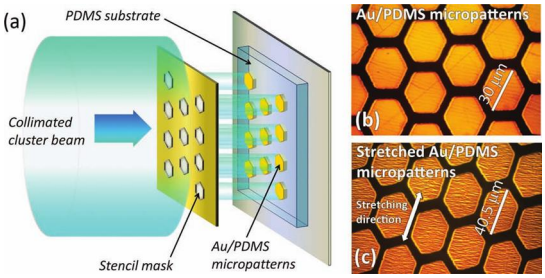

Figure 3. a) Schematic view of the process of stencil mask lithography: a TEM grid from Agar (G2760N) is interposed between the cluster beam and the PDMS substrate. b) A microscopy image of the obtained Au/PDMS nanocomposite micropatterns (the bright hexagons). c) A microscopy image of the same micropatterns stretched to 35% strain.

Experimental Section

The cluster beam used for the implantation was produced using a pulsed microplasma cluster source (PMCS)[25] equipped with a cavity in which a solid target made of the metals desired for the clusters (Au in the present case) was vaporized by a localized discharge supported by a pulsed injection of an inert gas (He or Ar) at high pressure (Figure 1a). The vaporized metal atoms aggregated in the cavity to form metal clusters, which were then driven out of the source cavity by the expansion of the inert gas through a nozzle to a vacuum chamber (expansion chamber, at a pressure of about 10^{-5} bar). Because of the high pressure difference between the source cavity and expansion chamber and the exploitation of aerodynamic focusing effects, the neutrally charged clusters were emitted from the source in the form of a highly collimated beam with a divergence lower than 1° and with the kinetic energy and mass distribution previously described.[25] The central part of the cluster beam was then allowed to enter a second vacuum chamber (deposition chamber) through a skimmer and it was intercepted by the polymeric substrate, which was supported by a motorized substrate holder. The holder allowed movement of the substrate in two directions orthogonal to the cluster beam axis (rastering), permitting the cluster implantation on an arbitrarily wide polymeric substrate. The substrates were exposed for ≈180 min at a deposition rate of 0.2 Å s^{-1}.

The Au targets (99.99% pure) were purchased from the 8853 S. p. a. company, and the PDMS substrates were prepared by spin-coating an ≈80 μm thick layer of the polymer precursor (Sylgard 184 Silicone Elastomer Kit from Dow Corning, mixed in a 10:1 ratio) on a glass slide covered by a thin layer of PMMA to reduce the adhesion of the elastomer film, at 1000 rpm for 60 s. After spin-coating, the polymer film was cured by heating at 100 °C for 35 min, as indicated by the producer.

© 2011 WILEY-VCH Verlag GmbH & Co. KGaA, Weinheim

In order to test the conductive performances of the samples during uniaxial strain cycles, the PDMS film, which was prepared as previously described, was cut in rectangular 3×8 cm^2 stripes and attached to two microscope glass slides, with the 5 mm long central portion of the membrane suspended between the slides (see Figure 2a). In the two extremities of the PDMS stripes, in the regions supported by the glass slides, two rectangular gold electrodes with resistances of $\approx 0.8\ \Omega$ were deposited by a standard evaporation process. The Au/PDMS nanocomposite film was implanted by SCBI across the electrodes and through the suspended portion of the membrane (see Figure 2a). The sample was then mounted on a custom-built motorized uniaxial stretcher by clamping only the glass-supported portion of the membrane to avoid the stretching of the gold-evaporated electrodes and to precisely define the membrane's portion subjected to strain as well as the percentage of strain. Clamping was also used to connect the evaporated electrodes to the contact pads, which, in turn, were connected to an Agilent 34410A multimeter. The stretcher and the multimeter were computer-controlled by LabVIEW software, allowing automatic acquisition of the nanocomposite electrical resistance with cyclic strain. The electrical resistance was recorded during measuring strain cycles at an elongation rate of 20 μm s^{-1} alternating with a series of fatigue strain cycles, at a faster elongation rate of 200 μm s^{-1}. Initially, subsequent measuring strain cycles were separated by a single fatigue strain cycle. As the total number of stretching cycles increased, the number of fatigue strain cycles between each measurement was progressively increased to 10, 50, 100, and 500.

Supporting Information

Supporting Information is available from the Wiley Online Library or from the author.

Acknowledgements

The authors thank Maura Francolini for her assistance with TEM characterization, Davide Marchesi and Gero Bongiorno for their assistance with SEM characterization, and Mary F. Ebeling for the syntactic revision of the manuscript.

Received: June 28, 2011
Revised: July 27, 2011
Published online: August 29, 2011

[1] J. A. Rogers, T. Someya, Y. Huang, *Science* **2010**, *327*, 1603.
[2] G. P. Collins, *Sci. Am.* **2004**, *291*, 74.
[3] K. Shiu, J. Zimmerman, H. Wang, S. R. Forrest, *Appl. Phys. Lett.* **2009**, *95*, 223503.
[4] S. R. Forrest, *Nature* **2004**, *428*, 911.
[5] M. B. Schubert, J. H. Werner, *Mater. Today* **2006**, *9*, 42.
[6] J. Engel, J. Chen, C. Liu, *Appl. Phys. Lett.* **2006**, *89*, 221907.
[7] S. Rosset, M. Niklaus, P. Dubois, H. Shea, *J. Microelectromech. Syst.* **2009**, *18*, 1300.
[8] D.-H. Kim, J. A. Rogers, *Adv. Mater.* **2008**, *20*, 4887.
[9] D.-H. Kim, N. Lu, R. Ghaffari, Y.-S. Kim, S. P. Lee, L. Xu, J. Wu, R.-H. Kim, J. Song, Z. Liu, J. Viventi, B. de Graff, B. Elolampi, M. Mansour, M. J. Slepian, S. Hwang, J. D. Moss, S.-M. Won, Y. Huang, B. Litt, J. A. Rogers, *Nat. Mater.* **2011**, *10*, 316.
[10] R. J. Coffey, *Artif. Organs* **2008**, *33*, 208.
[11] J. S. Perlmutter, J. W. Mink, *Annu. Rev. Neurosci.* **2006**, *29*, 229.
[12] G. M. Whitesides, *Nature* **2006**, *442*, 368.
[13] I. M. Graz, D. P. J. Cotton, S. P. Lacour, *Appl. Phys. Lett.* **2009**, *94*, 071902.
[14] S. Rosset, M. Niklaus, P. Dubois, H. R. Shea, *Adv. Funct. Mater.* **2009**, *19*, 470.
[15] G. Maggioni, A. Vomiero, S. Carturan, C. Scian, G. Mattei, M. Bazzan, C. de Julián Fernández, P. Mazzoldi, A. Quaranta, G. Della Mea, *Appl. Phys. Lett.* **2004**, *85*, 5712.
[16] O. Akogwu, D. Kwabi, A. Munhutu, T. Tong, W. O. Soboyejo, *J. Appl. Phys.* **2010**, *108*, 123509.
[17] D. S. Gray, J. Tien, C. S. Chen, *Adv. Mater.* **2004**, *16*, 393.
[18] J. Jones, S. P. Lacour, S. Wagner, Z. Suo, *J. Vac. Sci. Technol.* **2004**, *22*, 1723.
[19] L. Ravagnan, G. Divitini, S. Rebasti, M. Marelli, P. Piseri, P. Milani, *J. Phys. D: Appl. Phys.* **2009**, *42*, 082002.
[20] A. L. Barabasi, H. E. Stanley, *Fractal Concepts in Surface Growth*, Cambridge University Press, Cambridge, UK **1995**.
[21] P. D'Angelo, M. Barra, A. Cassinese, S. Guido, G. Tomaiuolo, *Macromol. Symp.* **2007**, *247*, 43.
[22] F. Faupel, R. Willecke, A. Thran, *Mater. Sci. Eng. R* **1998**, *22*, 1.
[23] T. Adrega, S. P. Lacour, *J. Micromech. Microeng.* **2010**, *20*, 055025.
[24] E. Barborini, S. Vinati, M. Leccardi, P. Repetto, G. Bertolini, O. Rorato, L. Lorenzelli, M. Decarli, V. Guarnieri, C. Ducati, P. Milani, *J. Micromech. Microeng.* **2008**, *18*, 055015.
[25] K. Wegner, P. Piseri, H. V. Tafreshi, P. Milani, *J. Phys. D: Appl. Phys.* **2006**, *39*, R439.

© 2011 WILEY-VCH Verlag GmbH & Co. KGaA, Weinheim

IOP Publishing Journal of Physics D: Applied Physics
J. Phys. D: Appl. Phys. **47** (2014) 015301 (10pp) doi:10.1088/0022-3727/47/1/015301

Patterning of gold–polydimethylsiloxane (Au–PDMS) nanocomposites by supersonic cluster beam implantation

C Ghisleri[1,2], F Borghi[1], L Ravagnan[2], A Podestà[1], C Melis[3], L Colombo[3] and P Milani[1,2]

[1] CIMAINA and Dipartimento di Fisica, Università degli Studi di Milano, via Celoria 16, 20133 Milano, Italy
[2] WISE srl, Piazza Duse 2, 20122 Milano, Italy
[3] Dipartimento di Fisica, Università di Cagliari, Cittadella Universitaria, 09042 Monserrato (Ca), Italy

E-mail: pmilani@mi.infn.it

Received 19 August 2013, revised 10 October 2013
Accepted for publication 24 October 2013
Published 3 December 2013

Abstract
Patterned gold–polydimethylsiloxane (Au–PDMS) nanocomposites were fabricated by supersonic cluster beam implantation (SCBI) of neutral gold nanoparticles in PDMS through stencil masks. The influence of nanoparticle dose on the surface roughness and morphology of the micropatterned regions of the nanocomposite was characterized. Nanoparticle implantation causes the swelling of PDMS without affecting substantially the lateral resolution of the patterns. In order to have an insight on the mechanism and the influence of nanoparticle implantation on the polymeric matrix, large-scale molecular dynamics simulations of the implantation process have been performed. The simulations show that even a single cluster impact on PDMS substrate strongly affects the polymer local temperature and density. Our results show that SCBI is a promising methodology for the efficient fabrication of nanocomposite microstructures on polymers with interesting morphological, structural and functional properties.

Keywords: nanocomposites, nanoparticles, stretchable polymers, micropatterning, AFM

(Some figures may appear in colour only in the online journal)

1. Introduction

Stretchable functional materials are enabling ingredients for the fabrication of wearable electronics [1], smart prosthetics [2, 3] and soft robotics [4–6]. These applications require the integration of electronic, optical and actuation capabilities on soft, conformable and biocompatible polymeric substrates [7, 8]. In particular, the fabrication of stretchable patterned microelectrodes is necessary for actuation [6, 9], electrical stimulation and recording in neuroprosthetics [10–12].

Poly(dimethylsiloxane) (PDMS) is a very popular playground for the proof-of-principle of soft devices since it couples biocompatibility with mechanical properties and machinability suitable for the production of dielectric elastomeric actuators [13]. Incorporation of metal nanoparticles in PDMS thin films using reduction of chemical precursors by superficial penetration or direct incorporation of preformed clusters have been used for the fabrication of lab-on-chip and optical devices ([14] and references therein). Particular efforts are also currently being concentrated on the fabrication of stretchable metallic circuits and microelectrodes integrated on PDMS [9, 15, 16].

A straightforward approach to the metallization (e.g. with Au, Ag, Pt, Pd) of PDMS is metal vapour deposition (MVD) [17], however, the use of MVD is hampered by the weak adhesion of the metallic layer on the elastomer and the subsequent delamination of the conducting layers even at very low deformations [11, 18, 19]. The use of adhesion layers such as Cr or Ti, or the treatment of the PDMS surface by oxygen plasma improve the performances, however the resilience is not adequate for a large number of applications [18, 20].

An alternative to MVD is ion implantation where noble metal ions are implanted with energies in the range of keV atom^{-1}, thus forming a conductive layer just below the polymeric substrate surface [21]; the diffusion of implanted ions gives also rise to the formation of nanoparticles

 © 2014 IOP Publishing Ltd Printed in the UK

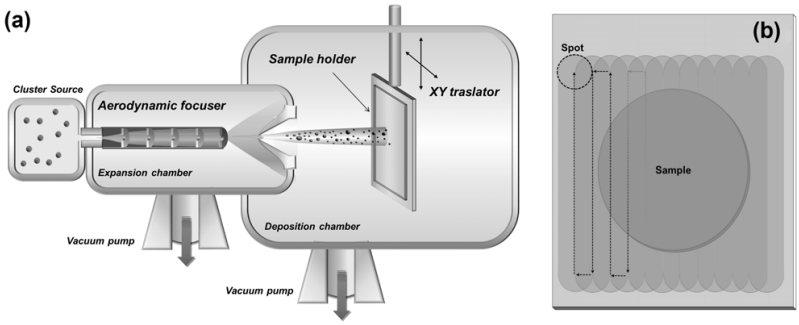

Figure 1. (*a*) The SCBI apparatus. The mix of gas and clusters produced in a cluster source attached to the expansion chamber is accelerated by a difference of pressure between the source and the expansion chamber and collimated by the aerodynamic focuser. Then the nanoparticles enter the deposition chamber and they are implanted in the polymeric substrate held on a movable sample holder allowing the deposition on large areas though a *rastering* technique. (*b*) Scheme of the rastering process: by moving repeatedly the sample holder vertically and horizontally with respect to the cluster beam, it is possible to uniformly implant large samples.

via Ostwald-ripening phenomena [22, 23]. Stretchable electrodes fabricated by ion implantation show adhesion and electrical conductivity degradation rates upon cyclical stretching that are significantly better than evaporated electrodes, however a substantial modification of the polymeric matrix due to radiation-induced disruption of chemical bonds, carbonization, bond reorganization and cross-linking is observed [24–26]. The use of ions also results in the build-up of electrical charges within the polymer substrate in the initial stages of the implantation process: this can perturb the trajectories of the incoming ions, thus lowering the lateral resolution of patterning performed using shadow masks. For this reason, shadow masks can be used only for structures larger than 100 μm; in general, micropatterning with high lateral resolution is obtained with ion implantation through photolithography steps or lift-off processes [21].

Recently we demonstrated that neutral metallic nanoparticles produced in the gas phase and aerodynamically accelerated in a supersonic expansion can be implanted in a polymeric substrate to form a conductive nanocomposite with superior resilience and interesting structural and functional properties [27, 28]. This approach is called supersonic cluster beam implantation (SCBI) and it is based on the use of a highly collimated supersonic beam carrying metallic clusters with a kinetic energy of about 0.5 eV atom^{-1}. Even if the kinetic energy is significantly lower than in ion implantation, neutral clusters are able to penetrate up to tens of nanometres into the polymeric target forming a conducting nanocomposite and avoiding electrical charging and carbonization [27, 28].

Supersonic cluster beams can be efficiently used for the production of micrometre-scale patterns through stencil masks [29, 30]. In particular, SCBI can produce micropatterns and microelectrodes on thin flexible polymeric substrates, such as SU8 using lift-off techniques [31]. Preliminary results showed also that electrically conducting regions can be patterned on PDMS with SCBI using stencil masks [27]. High-resolution patterning achievable with SCBI is a considerable advantage for soft devices microfabrication compared to chemical methods for functional nanocomposite production.

Here we present a characterization of 2D micropatterned regions of Au–PDMS nanocomposite integrated on PDMS by gold nanoparticle implantation through stencil masks. We have focused our attention on the evolution of surface roughness and morphology of Au–PDMS patterned nanocomposites and how this affects the lateral resolution attainable with SCBI. In order to have an insight into the influence of nanoparticle implantation on the polymeric matrix, we performed numerical simulations of the implantation process.

2. Experimental section

2.1. Supersonic cluster beam implantation

The supersonic cluster beam used for the implantation was produced by a pulsed microplasma cluster source (PMCS), as described in detail in [27, 32, 33]. Briefly, a PMCS consists in a ceramic body with a cavity where a metallic target (Au in the present case) is sputtered by a localized electrical discharge ignited during the pulsed injection of an inert carrier gas (He or Ar) at high pressure (40 bar). The sputtered metal atoms from the target thermalize with the carrier gas and aggregate in the cavity forming metal clusters. The carrier gas–cluster mixture expands out of the PMCS through a nozzle into a low pressure (10^{-6} mbar) expansion chamber (figure 1(*a*)). The supersonic expansion originating from the high pressure difference between the PMCS and the expansion chamber results in highly collimated supersonic beam: a divergence lower than 1° is obtained by using aerodynamic focusing nozzles [27, 33].

The central part of the cluster beam enters a second vacuum chamber (deposition chamber, at a pressure of about 10^{-5} mbar) through a skimmer, and it impinges on the polymeric substrate, supported by a motorized substrate holder. During implantation, the holder displaces the substrate in the two directions orthogonal to the cluster beam axis, allowing implantation on an arbitrarily wide area with a high homogeneity [31]. A typical scheme of this raster process is sketched in figure 1(*b*).

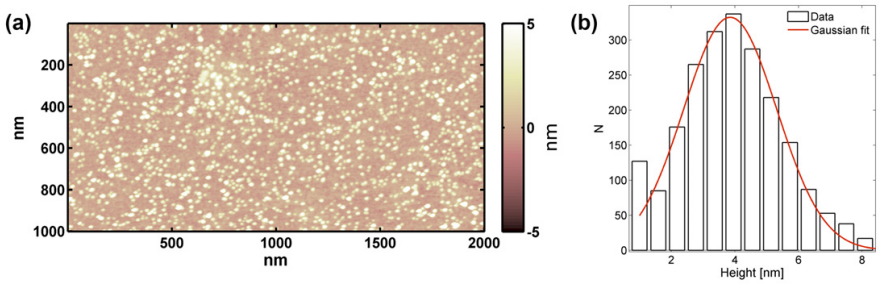

Figure 2. (*a*) AFM topography map (2 μm × 1 μm) of gold nanoparticles on silicon substrate; (*b*) Au nanoparticles size distribution obtained from the AFM map.

The size distribution of the nanoparticles used for implantation has been determined with atomic force microscopy (AFM) [34], by imaging a sub-monolayer sample obtained on a silicon substrate exposed to the nanoparticle beam for 3 s at a deposition rate of 0.02 nm s^{-1}. Figure 2(*a*) shows a representative topography of a 1 μm × 2 μm area of gold nanoparticles deposited on Si. The diameter of the nanoparticles (D_z) has been determined as the height of the objects. The distribution of heights (diameters) of nanoparticles, calculated from the analysis of ten topographic images, and the corresponding Gaussian fit are shown in figure 2(*b*). A mean value $D_z = 3.9 \pm 1.4$ nm (mean±standard deviation) was obtained.

Supersonic expansion accelerates the clusters to a mean velocity of approximately 1000 m s^{-1}, meaning that the metal clusters are accelerated towards the polymeric substrate with a kinetic energy E_k of roughly 0.5 eV atom^{-1} [35]. This energy is about four orders of magnitude less than the typical kinetic energies for ion beam implantation in polymers [9, 20]. Considering the atomic deposition rate N_{atm} (number of atoms reaching surface unit area per second), one can calculate the surface power density for the cluster implantation: $P_{surf} = N_{atm} \cdot E_k$. This power density is of the order of some μW cm^{-2} in the case of SCBI, thus not producing a significant increase of the substrate temperature above room temperature (RT). This should be compared with the power density for ion beams which is typically of the order of tenths of watts [21].

While for atom or nanoparticle deposition on a hard substrate one can define the thickness of the deposited material, in the case of nanoparticle implantation in polymers this quantity is not well defined. During implantation we placed a rigid substrate (generally a half-masked silicon or glass) on the sample holder together with the polymeric substrate to be implanted so that both intercept the same section of nanoparticles beam. Since the amount of deposited or implanted nanoparticles on the two substrates is the same, we can define the *equivalent thickness* t_{eq} of nanoparticles implanted in the nanocomposite as the thickness of the film produced by the same amount of nanoparticles deposited on the hard substrate.

2.2. Elastomeric substrates

PDMS substrates used in this work were produced with a Sylgard 184 Elastomer Kit (Dow Corning) by mixing for about 15 min the base and the curing agent in a 10 : 1 ratio. The mix was degased for 30 min in low vacuum in a desiccator and casted in a 10 cm diameter Petri dish up to a thickness of roughly 1 mm. After the polymerization at 100 °C for 1 h in an oven in ambient air, the PDMS was cut into pieces of the desired dimensions.

2.3. Patterning of the Au–PDMS nanocomposites

We used stencil masks for the nanocomposite patterning with micrometric resolution by exploiting the high collimation typical of supersonic beams. Three transmission electron microscopy (TEM) grids B, C and D (respectively, G2760N, G2786N, G220-8 from Agar Scientific) and a small piece of steel mesh (pattern E) were placed in front of the bare PDMS substrate at a distance of roughly 500 μm from the surface (figure 3(*a*)). The nickel grids have hexagonal, square and round holes with micrometric sizes of 30 μm, 7.5 μm and 36.5 μm, respectively, while the steel mesh consists in 4 μm × 90 μm and 60 μm spaced triangular apertures (see insets of figure 3(*b*)). Next to the masks a uniform region (area A in figure 3(*a*), size of 5 mm × 5 mm) was homogeneously implanted as a reference. Implantation through the masks was performed for 45 min at a rate of about 0.02 nm s^{-1}, reaching an equivalent thickness of 59 nm.

2.4. Implantation of nanoparticles with a radial density gradient

We characterized the effect of the dose of implanted nanoparticles on the surface morphology of PDMS by producing samples with a nanoparticles density gradient (figure 4). By moving the substrate during implantation only in the vertical direction (as schematically shown in figure 4(*a*)) we obtained a homogeneous nanocomposite in the direction parallel to the raster, with a gradient in the dose of nanoparticles implanted in the direction perpendicular to the raster. The deposition scheme of the sample with density gradient is shown in figure 4(*a*): a glass slide is half covered by a 13 mm wide and 76 mm long PDMS film, an aluminum foil mask partially shadows the PDMS film and the bare glass substrate. This configuration allows producing in one step a sample where implanted regions can be compared with pristine PDMS and cluster-assembled film on glass for

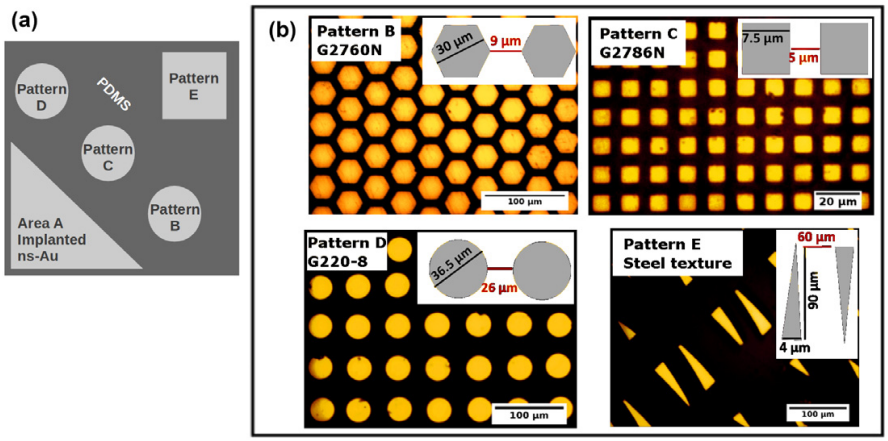

Figure 3. (*a*) Scheme of the sample prepared for the morphological characterization. Three TEM grids (patterns B, C, D) and a steel texture (pattern E) were used as stencil masks. The area A in the bottom left corner of the sample serves as reference for a non-patterned nanocomposite. (*b*) The four patterns in detail: the pictures represent the patterned PDMS observed with an optical microscope (50× magnification for pattern C, 20× magnification for the others), the insets in the top right corner in each picture represent the detailed scheme of the respective pattern.

the exact determination of the equivalent thickness gradient. The substrate underwent a SCBI process for 27 min with a deposition rate of 0.06 nm s^{-1}, reaching a maximum equivalent thickness (in the central position of the gradient) of 100 nm (figure 4(*b*)). The equivalent thickness of gold nanoparticles implanted in the PDMS follows a symmetric bell-shape trend in the horizontal direction, as reported in figure 4(*c*).

2.5. AFM characterization

The surface morphology of the nanocomposites was investigated using a Bioscope Catalyst/Nanoscope V AFM (Bruker Instruments). The AFM was operated in tapping mode in air, using rigid cantilevers with resonance frequency 250–350 kHz, equipped with single crystal silicon tips with nominal radius 5–10 nm. In the case of the sample produced with the radial density gradient, several 2 μm × 1 μm (2048 × 512 points) topographic maps were acquired on each of 12 different regions distributed along the gradient of the deposition and separated by about 100 μm from each other. The images were flattened by line-by-line subtraction of first- and second-order polynomials in order to remove artefacts due to sample tilt and scanner bow. AFM topographies are plotted using a colour scale spanning a finite vertical height range (dark to bright). On each flattened AFM image the RMS roughness R_q was calculated as the standard deviation of surface heights; R_q values have been averaged and standard deviation of the mean has been calculated as associated error.

2.6. TEM characterization

TEM was used for the evaluation of the clusters penetration depth d_{nc} in PDMS. Small PDMS substrates (approximately 5 mm long, 2 mm wide and 1 mm thick) were implanted with different increasing doses in order to evaluate the evolution of the implantation process and nanoparticle organization in the matrix. We used implantation times of 3 s, 30 min and 120 min at a rate of about 0.02 nm s^{-1}, reaching an equivalent sub-monolayer on a rigid substrate and equivalent thicknesses of 40 nm and 140 nm, respectively. Ultra-thin slices (with a thickness of about 100 nm) of nanocomposite were cut with a cryo-ultramicrotome at −160 °C and laid down on TEM grids covered with a layer of carbon-coated Formvar. Images were acquired with a Philips CM10 (80 kV) microscope.

2.7. Wettability characterization

The wettability of the nanocomposite surface was analysed by contact angle measurements with First Ten Angstroms FTA200. A milli-Q water droplet (volume: 3×10^{-6} l) was deposited on the surface of area A of the patterned nanocomposite sample and the contact angle value obtained by averaging 150 measures from as many droplet images acquired by a CCD camera immediately after the deposition.

2.8. Modelling

We performed large-scale molecular dynamics simulations of the implantation process based on state-of-the-art force fields [36]. While technical details of the present simulations have been published elsewhere [37], here we remark on their most important features. First of all, in order to keep the present simulations on the relevant experimental length scale we made use of very large-scale simulation cells containing as many as ∼4.6 million atoms. This system size corresponds to 25.6 × 25.6 × 85.35 nm^3: indeed, a very large simulation cell (demanding a very intense computer effort), is necessary if the full process of surface impact, the propagation into the substrate and the stopping of the Au clusters must be reproduced. Such large systems have been aged for as many

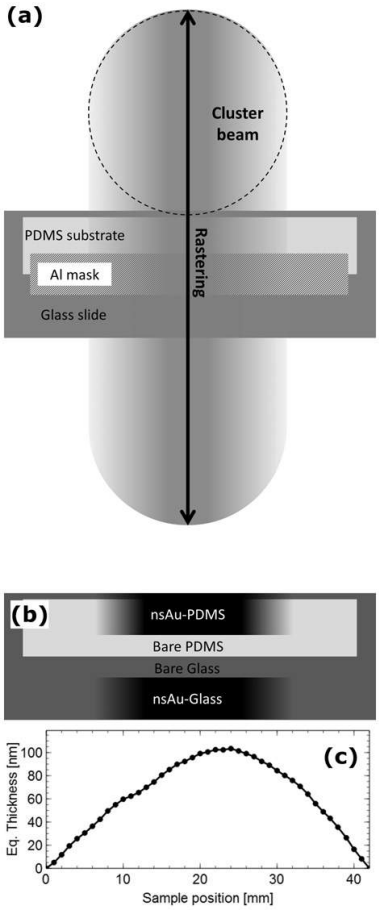

Figure 4. (*a*) Scheme of the sample prepared for the morphological characterization of the nanocomposite as a function of the equivalent thickness. The rastering in the vertical direction allows obtaining a gradient of nanoparticle dose implanted in the PDMS substrate. (*b*) Scheme of the sample after the implantation process: the deposition on glass serves as reference of a cluster-assembled film on a rigid substrate. (*c*) Equivalent thickness as a function of the horizontal position of the analysed sample.

as 180 ps. Such a relatively long simulation time was indeed necessary in order to allow the system to fully stabilize after the cluster impact.

Furthermore, special care was taken to model the interactions between the implanted Au clusters and the target substrate, as well as the possible presence of molecular linkers into the PDMS film. Accurate benchmark calculations have been executed on well-known physical properties of pristine PDMS (such as density and radial distribution function), confirming the quantitative reliability of the present computational set-up. Finally, the simulated protocol of implantation was chosen so as to mimic as close as possible the actual SCBI process; in particular, we implanted Au clusters with radius of 3 nm with energies of 0.5, 1.0 and 2.0 eV atom^{-1}.

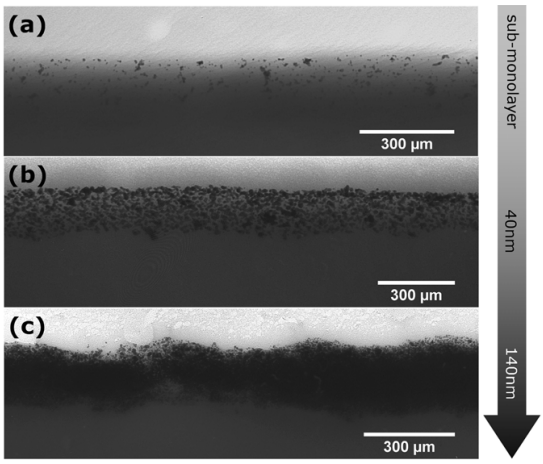

Figure 5. TEM images of thin slices (about 100 nm thickness) of the PDMS implanted for 3 s (*a*), with an equivalent thickness of 40 nm (*b*) and 140 nm (*c*) of gold nanoparticles. The penetration depth of the nanoparticles is approximately 180 nm in each case.

3. Results and discussions

3.1. Cluster implantation depth

The implantation of gold nanoparticles for different t_{eq} has been characterized by TEM imaging of ultra-thin slices of nanocomposite cut by cryo-ultramicrotomy. Figure 5(*a*) shows the nanoparticles embedded in the polymer resulting from a supersonic beam exposure of the substrate of 3 s, the implantation depth is roughly of 180 nm. A slight increase of nanoparticles density towards the PDMS surface is visible: this can be explained in terms of the limited dynamic range of the CCD camera overexposing the polymer–vacuum interface. By increasing the dose of implanted nanoparticles to equivalent thicknesses of 40 nm (figure 5(*b*)) and 140 nm (figure 5(*c*)), an increase of the volume filling factor (defined as the ratio between the total volume of the nanoparticles and the volume of the polymer in which they are implanted) is observed without any significant change in the cluster implantation depth. These observations indicate that implantation depth does not depend on the dose of implanted nanoparticles. A further increasing of the dose results in the surfacing of the clusters on top of the polymeric substrate and in the formation of a cluster-assembled metallic layer on the PDMS surface [27].

3.2. Patterning and swelling

Different nanocomposite patterns were produced and analysed, as described in the experimental section: here we report the results relative to hexagonal-shaped patterns; similar results have been obtained for the other patterns. Figure 6(*a*) shows the AFM characterization of the pattern, figures 6(*b*) and (*c*) show an individual hexagon with a surface presenting fractures. The equivalent thickness of implanted nanoparticles is $t_{eq} = 59 \pm 3$ nm, while the measured height of Au/PDMS hexagon is larger, being 100 ± 6 nm; this suggests that PDMS

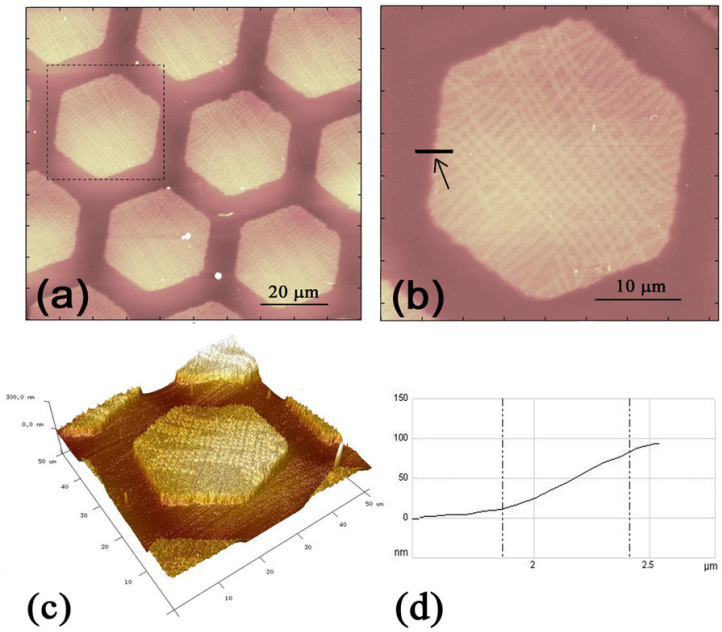

Figure 6. (*a*) AFM morphological map of the hexagonal patterns; (*b*) single hexagonal pattern, z scale ranges from −100 to 300 nm; (*c*) 3D map of the same pattern; (*d*) topographic profile across the boundary between bare PDMS and Au-nc/PDMS indicated by the arrow in (*b*).

undergoes swelling upon cluster implantation. Swelling in PDMS is reported as a consequence of solvent exposure [38]; far less studied is the effect of nanoparticle embedding on the reorganization of polymeric chains in silicones, although the formation of voids in polymers embedding inorganic particles has been reported [39]. In our case swelling could degrade the lateral resolution obtainable with patterning through stencil masks. To check this aspect we performed an AFM analysis of the boundary between bare PDMS and Au/PDMS hexagonal pattern (as indicated by the arrow in figure 6(*b*)). The effective lateral resolution of the pattern ranges from 0.5 to 1 μm showing that good lateral resolution can be obtained by SCBI in spite of the swelling phenomenon (figure 6(*d*)).

In order to clarify the relationship of the implanted nanoparticle dose with the PDMS swelling, we systematically analysed the evolution of the step between the bare PDMS substrate and the Au/PDMS nanocomposite in the sample with a nanoparticle density gradient (see section 2.4). The equivalent implantation thickness and the height of the swollen region of Au/PDMS nanocomposite with respect to the bare PDMS substrate were calculated from the histogram of the heights of AFM images acquired across sharp steps at the ns-Au/glass or Au-nc/PDMS boundaries, accordingly, produced by masking (figure 4(*b*)). The mean thickness/height was extracted as the distance between the peaks of the height distribution of the topographic maps; the errors associated with the average quantities were calculated summing in quadrature a statistical error (the standard deviation of the mean of step values calculated from different images), and a systematic error (7%), due to the non-linearity of the AFM piezo. The step height is always larger than the corresponding t_{eq}: the relation

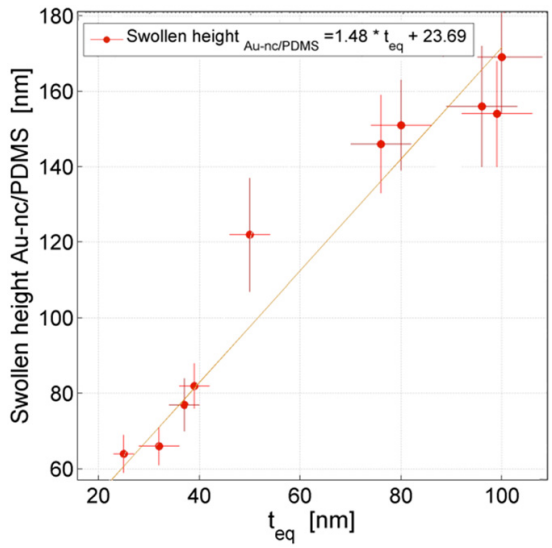

Figure 7. Thickness of the swollen gold nanoparticles PDMS nanocomposite versus the equivalent thickness of implanted clusters. The linear equation fit of the data is also shown.

between t_{eq} and the swelling height is to a good approximation linear as reported in figure 7. The swelling of PDMS grows with t_{eq} and even with $t_{eq} = 100$ nm it increases for more than a rigid offset without saturation in the investigated interval.

A possible origin of the observed swelling is the modification of the links between polymer chains caused by

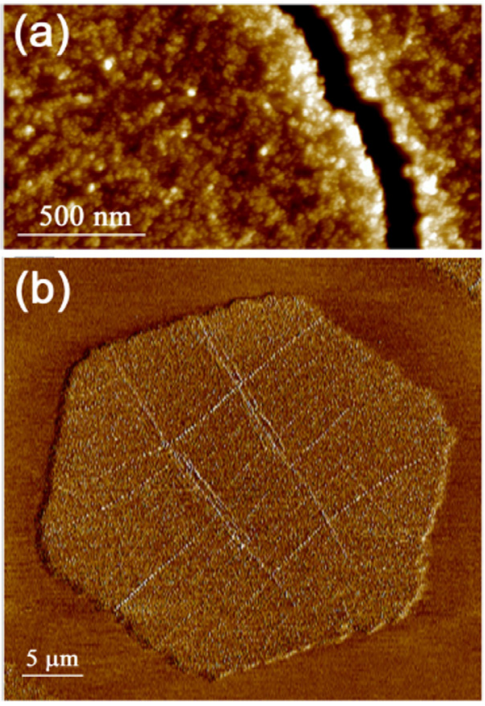

Figure 8. (*a*) AFM topographic map of the Au-nc/PDMS, with a detail of a crack on the surface. (*b*) Phase map of the hexagonal pattern.

nanoparticle impact during implantation: in order to check the presence of partial break up and reorganization of links at the polymer surface, we measured the wettability of implanted and pristine PDMS. For each of the two surfaces three series of data were acquired by depositing droplets in different points, in order to test the homogeneity of the sample. A contact angle of $(113 \pm 3)^\circ$ was measured on the bare PDMS, while the PDMS implanted with an equivalent thickness of 59 nm of gold nanoparticles (area A in figure 3) is characterized by a contact angle of $(112 \pm 3)^\circ$. These measurements suggest that gold cluster implantation does not significantly affect the microscopic structure of the PDMS surface.

Numerical simulations (see below) confirm that chains breakage is not occurring, whereas a local heating upon implantation is produced; this might be the origin of a local decrease of polymer density.

3.3. Surface morphology

Figure 6(*b*) and the 3D map in figure 6(*c*) show the presence of scratches on the surface. In figure 8(*a*) a detail of one of these surface defects, which appears like a fracture with elevated rims, is shown. The depth of the fracture as measured from the AFM image is 25 nm, although due to the limited penetration of the AFM tip inside the high aspect ratio defect this value must be taken as a lower limit for the actual fracture depth. We analysed the Au/PDMS roughness in 12

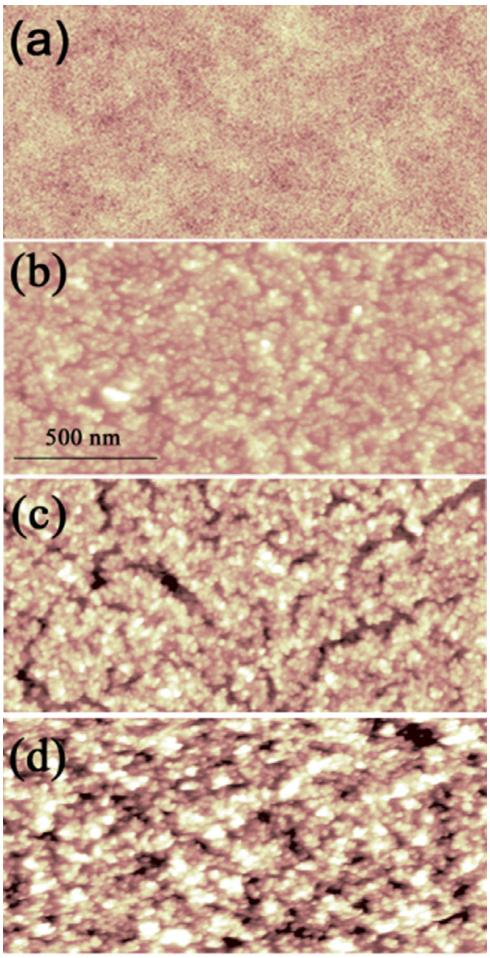

Figure 9. AFM topographical maps of PDMS (*a*), and three different samples of Au-nc/PDMS with equivalent thicknesses ~20 nm (*b*), 40 nm (*c*) and 100 nm (*d*); *z* scale ranges from −20 to 20 nm.

different positions along the gradient of deposited material, characterized by equivalent thickness t_{eq} ranging from 20 to 100 nm. Figure 9 reports the evolution of surface morphology upon the increase of the implantation dose from a pristine PDMS surface to three Au-nc/PDMS samples characterized by increasing equivalent thicknesses ($t_{eq} \approx 20$ nm, 40 nm and 100 nm, respectively). Nanoparticles implantation in PDMS produces an increasing corrugation as t_{eq} increases, with the appearance of craters and fractures which grow deeper and larger as the Au cluster loading on PDMS increases. The RMS roughness R_q of Au/PDMS nanocomposite evolves with t_{eq}: the quantitative analysis of the evolution of R_q with t_{eq} is reported in log–log scale in figure 10. For comparison purposes, we report in figure 11 the AFM topography of a Au/PDMS nanocomposite and that of a nanostructured film obtained by deposited gold cluster on a silicon substrate (ns-Au/Si) with the same equivalent thickness $t_{eq} \approx 20$ nm.

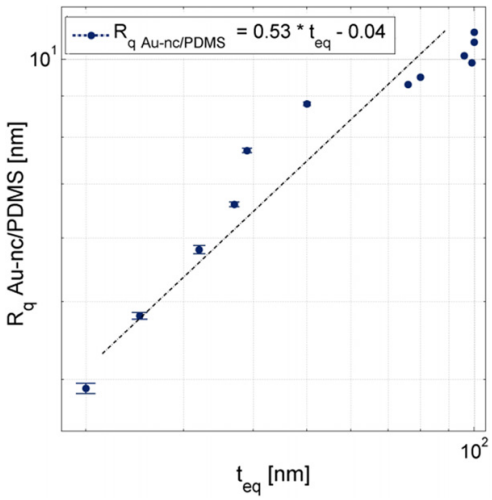

Figure 10. Log–log plot of the roughness of the swollen gold nanoparticles PDMS nanocomposite versus the equivalent thickness.

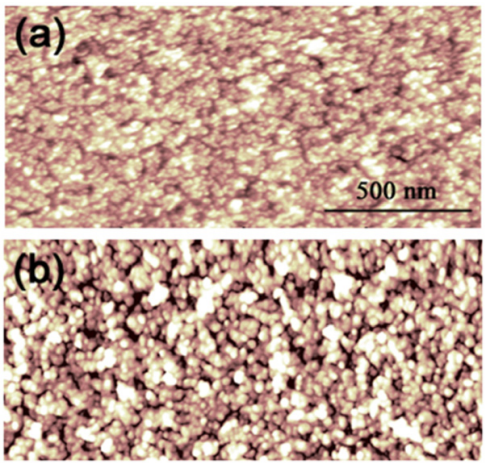

Figure 11. AFM topographical maps of Au-nc/PDMS (*a*) and ns-Au/Si (*b*). z scale ranges from −10 to 10 nm.

Table 1. RMS roughness R_q of the bare PDMS in different locations of the patterned sample (see figure 3).

Sample	Roughness R_q (nm)
Isolated PDMS	0.56 ± 0.01
Pattern B	0.98 ± 0.01
Pattern C	1.18 ± 0.01
Pattern D	0.78 ± 0.03
Pattern E	0.84 ± 0.01

Despite the similar thickness, roughness is markedly different: R_q of ns-Au/Si $= 6.8 \pm 0.1$ nm, while R_q Au-nc/PDMS $= 3.9 \pm 0.1$ nm.

The implantation of gold clusters in PDMS induces a change of morphology also in the PDMS regions close to the implanted area, as reported in table 1. The increase in PDMS roughness could be due to the horizontal swelling of the PDMS with implanted Au clusters or to the diffusion of Au clusters in the PDMS polymeric substrate, even though in AFM phase maps (figure 8(*b*)), a clear contrast between the bare PDMS and the Au-nc/PDMS nanocomposite is not visible.

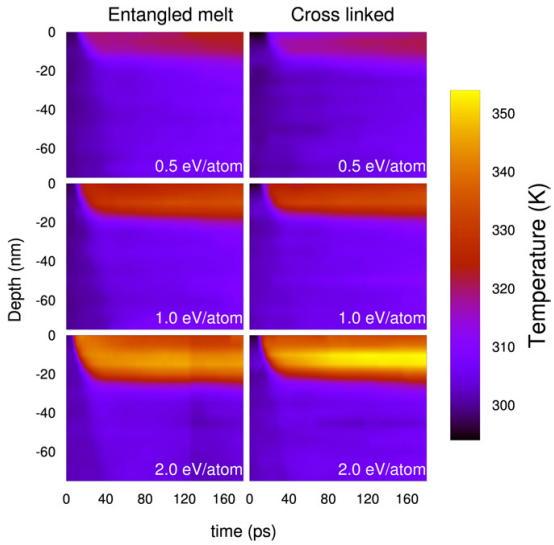

Figure 12. Temperature field (versus time and depth) of the EM- (left) and CL- (right) PDMS for the implantation energies of 0.5 eV atom^{-1} (top), 1.0 eV atom^{-1} (middle) and 2.0 eV atom^{-1} (bottom).

3.4. Numerical simulation of cluster implantation

Neutral metallic cluster implantation in polymers has been discovered only very recently [26, 27] and no detailed physical models of this phenomenon are available. Computer experiments are currently underway to gain deeper understanding of the microscopic mechanisms and the influence of the structural and mechanical properties of the polymeric matrix on the implantation. Recent simulations [36] provided evidence that for both entangled-melt (EM) and cross-linked (CL) PDMS the Au cluster penetration depth linearly depends on the implantation energy, having an angular coefficient of 7 nm eV^{-1} or 6 nm eV^{-1}, respectively. These results were explained in terms of the so-called *clearing the way effect* [40] which also predicts an inverse dependence of the same depth on the substrate cohesive energy.

In order to better characterize the implantation effect, we investigated the temperature field (wave) generated (propagating) inside the PDMS substrate upon cluster impact. In particular, we calculated the time-dependent temperature profile of the substrate during the implantation as a function of the penetration depth from the PDMS surface. Results are shown in figure 12 for the EM- (left) and CL- (right) substrates, corresponding to implantation energies of 0.5 (top), 1.0 (middle) and 2.0 (bottom) eV atom^{-1}. For both EM- and CL-PDMS we observe a sudden temperature increase ΔT_{PDMS} in the surface region: $\Delta T_{\mathrm{PDMS}} \sim 20$, 30 and

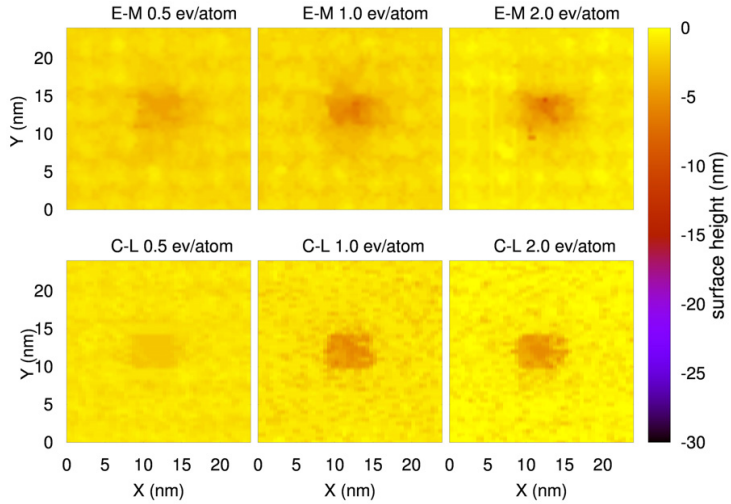

Figure 13. EM- (top) and CL- (bottom) PDMS surface height map for the implantation energies of 0.5 eV atom^{-1} (left), 1.0 eV atom^{-1} (centre) and 2.0 eV atom^{-1} (right).

50 K for increasing implantation energy. The corresponding temperature wave generated upon the impact is dissipated within the bulk substrate. After 180 ps we identify two main temperature spots in the PDMS substrate, namely: a *hot* region (H) at $T \sim 320$–350 K (figure 12, red–yellow shaded area) close to the surface and a *cold* region (figure 12, blue shaded area) at $T \sim 300$–310 K deeper into the substrate. We remark that the overall temperature increase is always larger for the cross-linked substrate, as a consequence of the different stiffness: the deformation upon the impact is larger in the case of the EM-PDMS substrate, thus resulting in a comparatively reduced increase of temperature.

The extension of the H region depends also on the implantation energy: by increasing its value from 0.5 to 2.0 eV atom^{-1}, we observe an increase of the H region depth from ∼10 nm up to ∼25 nm. Therefore, another effect of a single cluster impact is to increase the PDMS surface temperature up to 50 K, thus generating a decrease of the substrate density as large as ∼5%. This feature is in good agreement with the experimental finding of [41] that predicts a PDMS density decrease of ∼5% by increasing the temperature from 300 to 350 K. Therefore, the next impinging clusters will penetrate easily on a lower density PDMS substrate, further enhancing the effect of the local polymer density. This density decrease could explain the PDMS swelling experimentally observed upon the implantation.

We have extensively investigated the effect of a single cluster impact on the PDMS surface morphology by performing a theoretical analysis of the surface roughness. By analogy with the experimental AFM investigations reported above, we analysed the PDMS surface and internal nanopores by means of a spherical Au probe of radius 1.0 nm placed on top of the substrate. The probe interacts with the substrate via a 9-6 Lennard-Jones potential having the ε and σ parameters taken from the COMPASS force field. We spotted the PDMS surface by a square grid of points with 0.5 nm spacing; at each point of the grid we placed the probe and, by gently moving it up and down, we determined probe height corresponding to the minimum energy of the probe–substrate system. The envelope of such heights provided the simulated surface topography map, as shown in figure 13. The map, which has been suitably smoothed by means of a spline procedure, represents the surface height with respect to a conventional zero set at the maximum atom vertical position in the PDMS film.

In all cases we notice the presence of a crater created on the surface by the impinging Au cluster. The lateral dimensions of the crater (as large as ∼6 nm) are almost unchanged by increasing the implantation energy, while the crater depth strongly depends on it. In fact, for EM-(CL-)PDMS, we measure crater depths of ∼6 (3) nm, ∼8 (6) nm and ∼10 (7) nm for implantation energies of 0.5 eV atom^{-1}, 1.0 eV atom^{-1} and 2.0 eV atom^{-1}, respectively. The overall root-mean-square roughness (R_q) of EM-(CL-) PDMS increases with the implantation energy: $R_q = 1.1 \pm 0.1$ (0.9±1) nm, 1.8±0.1 (1.7±0.1) nm and 2.5±0.1 (2.3±0.1) nm for implantation energies of 0.5 eV atom^{-1}, 1.0 eV atom^{-1} and 2.0 eV atom^{-1}, respectively.

Shallower craters and an overall smaller roughness have been observed in the case of CL-PDMS. These results are consistent with the reduced cluster penetration depth observed for CL-PDMS [37]. This is due to the fact that in EM-PDMS the polymer chains are bonded only via dispersion and electrostatic interactions, while in the CL-PDMS the chains are partially covalently linked via the cross-linker molecule. Since the cluster penetration inside the PDMS matrix involves the breaking of the inter-chains bonds, we conclude that during the penetration inside the EM-PDMS substrate, the cluster experiences a weaker friction with respect to CL-PDMS.

4. Conclusions

We demonstrated the micrometric 2D patterning of Au–PDMS nanocomposite by supersonic cluster beam implantation through stencil masks on PDMS. The evolution of surface morphology and swelling of the patterned substrate can be quantitatively correlated to the dose of implanted nanoparticles. The PDMS swelling upon implantation does not substantially affect the lateral resolution of the pattern.

Atomistic simulations provide information on the PDMS microstructural evolution upon cluster implantation: the results show that even a single cluster impact on the PDMS substrate remarkably changes the polymer local temperature and density. Moreover, we observe the presence of craters created on the polymer surface having lateral dimensions comparable to the cluster radius and depths strongly dependent on the implantation energy.

Our results suggest that SCBI is a promising methodology for the efficient and easy fabrication of nanocomposite microstructures on polymers with interesting morphological, structural and functional properties.

Acknowledgments

The authors acknowledge Regione Lombardia and Regione Sardegna for their financial support to the project 'ELDABI - Elettronica Deformabile per Applicazioni Biomediche' (project n. 26599138). We also acknowledge computational support by CINECA (Bologna, Italy) under project ISCRA-UCIP, Maura Francolini, Elisa Sogne and Fondazione Filarete for support in TEM and Contact Angle measurements

References

[1] Pang C, Lee C and Su K-Y 2013 *J. Appl. Polym. Sci.* **130** 1429
[2] Moon J-H, Baek D H, Choi Y Y, Lee K H, Kim H C and Lee S-H 2010 *J. Micromech. Microeng.* **20** 025032
[3] Baek J-Y, An J-H, Choi J-M, Park K-S and Lee S-H 2008 *Sensors Actuators* A **143** 423
[4] Nawroth J C, Lee H, Feinberg A W, Ripplinger C M, McCain M L, Grosberg A, Dabiri J O and Parker K K 2012 *Nature Biotechnol.* **30** 792
[5] Buselli E, Smith A, Grover L, Levi A, Allman R, Menciassi A, Mattoli V and Beccai L 2011 *Microelectron. Eng.* **88** 1676
[6] Kovacs G, Lochmatter P and Wissler M 2007 *Smart Mater. Struct.* **16** S306
[7] Ma Z 2011 *Science* **333** 830
[8] Rogers J A, Someya T and Huang Y 2010 *Science* **327** 1603
[9] Rosset S and Shea H R 2013 *Appl. Phys.* A **110** 281
[10] Cyganowski A, Minev I R, Vachicouras N, Musick K and Lacour S P 2012 *IEEE Sensors 2012 Conf. (28–31 October)* paper 1974
[11] Graudejus O, Morrison B, Goletiani C, Yu Z and Wagner S 2012 *Adv. Funct. Mater.* **22** 640
[12] Lacour S P, Benmerah S, Tarte E, FitzGerald J, Serra J, McMahon S, Fawcett J, Graudejus O, Yu Z and Morrison B III 2010 *Med. Biol. Eng. Comput.* **48** 945
[13] Molberg M, Leterrier Y, Plummer C J G, Walder C, Löwe C, Opris D M, Nüesch F A, Bauer S and Månson J-A E 2009 *J. Appl. Phys.* **106** 054112
[14] Berry K R Jr, Russell A G, Blake P A and Roper D K 2012 *Nanotechnology* **23** 375703
[15] Zhang Y, Xu S, Fu H, Lee J, Su J, Hwang K-C, Rogers J A and Huang Y 2013 *Soft Matter* **9** 8062
[16] Adrega T and Lacour S P 2010 *J. Micromech. Microeng.* **20** 055025
[17] Graz I M, Cotton D P J and Lacour S P 2009 *Appl. Phys. Lett.* **94** 071902
[18] Douville N J, Li Z, Takayama S and Thouless M D 2011 *Soft Matter* **7** 6493
[19] Tuinea-Bobe C L, Lemoine P, Manzoor M U, Tweedie M, D'Sa R A, Gehin C and Wallace E 2011 *J. Micromech. Microeng.* **21** 115010
[20] Akogwu O, Kwabi D, Munhutu A, Tong T and Soboyejo W O 2010 *J. Appl. Phys.* **108** 123509
[21] Rosset S, Niklaus M, Dubois P and Shea H 2009 *Adv. Funct. Mater.* **19** 470
[22] Popok V N 2012 *Rev. Adv. Mater. Sci.* **30** 1
[23] Bechelany M, Maeder X, Riesterer J, Hankache J, Lerose D, Christiansen S, Michler J and Philippe L 2010 *Cryst. Growth Des.* **10** 587
[24] Jagielski J, Piatkowska A, Aubert P, Thomé L, Turos A and Abdul Kader A 2006 *Surf. Technol.* **200** 6355
[25] Abdul-Kader A M, Turos A, Grambole D, Jagielski J, Piatkowska A, Madi N K and Al-Maadeed M 2005 *Nucl. Instrum. Methods* B **240** 152
[26] Clough R L 2001 *Nucl. Instrum. Methods* B **185** 8
[27] Corbelli G, Ghisleri C, Marelli M, Milani P and Ravagnan L 2011 *Adv. Mater.* **23** 4504
[28] Ravagnan L, Divitini G, Rebasti S, Marelli M, Piseri P and Milani P 2009 *J. Phys. D: Appl. Phys.* **42** 082002
[29] Barborini E, Piseri P, Podestà A and Milani P 2000 *Appl. Phys. Lett.* **77** 1059
[30] Barborini E *et al* 2008 *J. Micromech. Microeng.* **18** 055015
[31] Marelli M, Divitini G, Collini C, Ravagnan L, Corbelli G, Ghisleri C, Gianfelice A, Lenardi C, Milani P and Lorenzelli L 2011 *J. Micromech. Microeng.* **21** 045013
[32] Barborini E, Piseri P and Milani P 1999 *J. Phys. D: Appl. Phys.* **32** L105
[33] Wegner K, Piseri P, Tafreshi H V and Milani P 2006 *J. Phys. D: Appl. Phys.* **39** R439
[34] Keller D 1991 *Surf. Sci.* **253** 353
[35] Milani P and Iannotta S 1999 *Cluster Beam Synthesis of Nanostructured Materials* (Berlin: Springer)
[36] Sun H 1998 *J. Phys. Chem.* B **102** 7338
[37] Cardia R, Melis C and Colombo L 2013 *J. Appl. Phys.* **113** 224307
[38] Lee J N, Park C and Whitesides G M 2003 *Anal. Chem.* **75** 6544
[39] Shirazi Y, Ghadimi A and Mohammadi T 2012 *J. Appl. Polym. Sci.* **124** 2871
[40] Yamamura Y and Muramoto T 1992 *Phys. Rev. Lett.* **69** 1463
[41] Shih H and Flory P J 1972 *Macromolecules* **56** 758

Part II

Reflective stretchable optics

CHAPTER 4

Fabrication and characterization of elastomeric optical devices

Elastomeric optical devices fabricated by Supersonic Cluster Beam Implantation of silver nanoparticles in PDMS were optically and morphologically characterized. In particular the performances of elastomeric nanocomposite-based mirrors and diffraction gratings were studied and compared with the state of the art.

4.1 Fabrication of the devices

Polydimethilsiloxane (PDMS) represents the ideal substrate for the fabrication of elastomeric optical devices, in terms of easy of processing, low cost, wide availability and good mechanical properties [12].

The first step of elastomeric mirrors and diffraction gratings fabrication process consists in the production of the PDMS substrate, following two approaches according to the wanted device. For the fabrication of elastomeric mirrors liquid PDMS was simply spin-coated on a glass slide, obtaining a uniform thin polymeric film. The surface of a commercially available rigid diffraction grating was replicated with PDMS by molding technique [12, 23] for the fabrication of elastomeric diffraction gratings.

PDMS substrates were implanted by SCBI of Ag nanoparticles with different equivalent thicknesses, up to 290nm, in order to study the effect of the polymer filler loading on the optical properties of the nanocomposite. Silver was chosen for its low cost and superior and uniform reflectivity in the visible range compared to other metallic materials (gold, for example).

Similar PDMS substrates were metallized by means of thermal evaporation for a comparison of the optical and morphological properties with the nanocomposite-based devices.

4.2 Morphological characterization

In the previous chapter the surface roughness was investigated in order to control the fraction of impinging light scattered from the device surface. Here the morphological properties relative to the devices were characterized, like the cracking of the reflective layer and the profile of the metallized elastomeric diffraction grating.

The superior resilience of the nanocomposite reflective layer undergoing mechanical stress was demonstrated by investigating the surface of SCBI and evaporated mirrors and gratings with an optical microscope in different conditions: as deposited, after peeling (i.e. removal of the nanocomposite from the supporting substrate) and after thousands of 50% stretching cycles. Evaporated samples rapidly encounter a deterioration

due to the breakage of the rigid conductive layer on top of the polymer surface, while SCB implanted devices do not show significant changes in their surface morphology.

The different effects of the reflective layer behavior upon mechanical stress are particularly important in the case of diffraction gratings: here the formation of cracks, with dimensions and periodicity comparable with the grooves of the grating, strongly affect the performances of the optical device. For this purpose, the morphology of the elastomeric gratings was further studied by acquiring AFM single-line scans of both the bare and metallized grating profiles. The results show a very good agreement between the profiles of the bare PDMS and the SCBI grating (also thanks to the high collimation of the cluster beam, allowing to perfectly reproduce the three dimensional structure of the grating), while a highly irregular profile is observed in the case of the evaporated grating.

4.3 Optical properties

4.3.1 Reflectance

Reflectivity of the nanocomposite superficial layer represents the most important optical property of the devices studied in this work. Samples with different equivalent thicknesses (30nm, 60nm, 120nm and 290nm) were analyzed in order to understand the effect of different nanoparticles concentrations on the trend of the surface reflectivity. The equivalent thickness maximizing the reflectivity of the device must be determined.

The optical setup for reflectance spectra measurement, shown in Figure4.1a, consists in a halogen lamp as light source, positioned at a large distance from a diaphragm (ideally at infinite distance) aiming to filter the white light generated by the lamp. The sample, held on a tilting stage for its fine alignment with the detector, immediately follows the diaphragm. The white light beam impinges on the nanocomposite with an angle of 45° and the reflected beam is collected by a computer controlled monochromator. The monochromator is equipped with a 600 lines/mm grating and a CCD camera (controlled with the monochromator) for the spectra acquisition in the vis-NIR range (350-1100nm). Reflectance $R(\omega)$ was calculated as the ratio between the intensity $I_R(\omega)$ of the light reflected by the sample and the intensity $I_0(\omega)$ of impinging light:

$$R(\omega) = \frac{I_R(\omega)}{I_0(\omega)} \tag{4.1}$$

In order to acquire the spectrum of the impinging light while maintaining the optical setup unaltered, I_0 was measured by replacing the sample with a commercial mirror.

The results, shown in Figure4.1b, present an interesting behavior. Reflectance of the 30nm-implanted PDMS is very poor, around 20% throughout the whole visible range, as expected since the low number of implanted particles. Reflected light intensity is strongly enhanced by the increase the equivalent thickness. Reflectivities between 60% and 70% are achieved for an equivalent thickness of 60nm, however reflected light intensity suddenly drops to 30%-40% for equivalent thicknesses of 120nm and 290nm respectively. This deterioration of the reflectivity for high nanoparticles concentration in the polymer depends on the complex behavior of the *surface plasmon resonance* (extensively studied in chapter 7) and, for even higher equivalent thicknesses, to the cracking of the cluster layer growing *on* the polymer surface once the implanted layer of PDMS is saturated. As a result of this characterization, an equivalent thickness of 60nm was chosen as a *standard* for the fabrication of all the samples and devices studied in this work (except where otherwise specified).

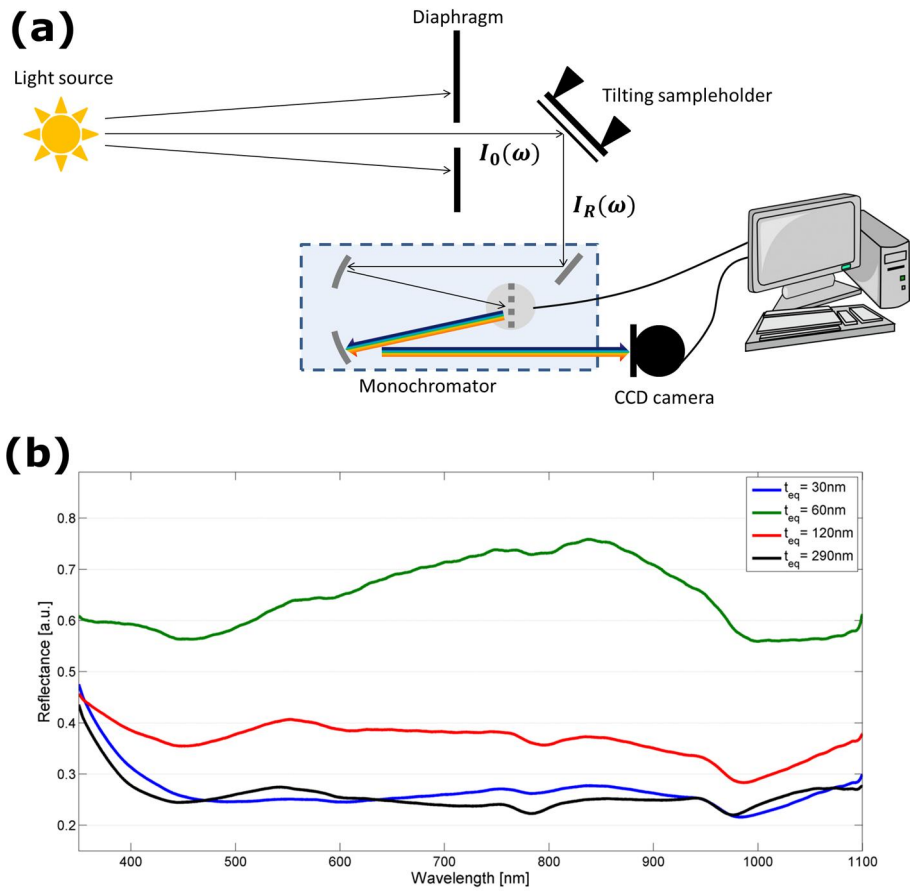

Figure 4.1: (a) Optical setup for the acquisition of reflectance spectra. (b) Reflectance spectra of the Ag/PDMS nanocomposite with different implanted equivalent thicknesses. The best reflectivity is achieved with an equivalent thickness of 60nm.

Reflectance of 60nm SCB implanted nanocomposite mirror was compared with a silver-evaporated PDMS mirror and the state of the art in the field of tunable gratings, consisting in gold-evaporated PDMS thin films [82]. Silver evaporated mirrors present a reflectivity similar to silver implanted PDMS while gold-evaporated PDMS show a much lower reflectivity (between 20% and 40%), dramatically dropping after few mechanical deformations.

4.3.2 Spot size and linearity

The effect of the irregular profile of the evaporated grating was quantitatively studied by measuring the diffracted spot size (referred as the solid angle subtended by the spot) when illuminated with monochromatic line (He-Ne laser, wavelength 632.8nm). Unlike nanocomposite-based gratings, in which the solid angle initially decreases and then remain stable up to 50% stretching, a strong instability of the solid angle is observed for gratings metallized by evaporation. Moreover, the formation of large cracks perpendicular to the grating grooves on the surface of the evaporated grating gives rise to the ap-

pearance of an unexpected and unwanted diffraction pattern orthogonal to the expected one.

The linear behavior of the diffraction angle as a function of the stretching percentage was tested too with good results for both the evaporated and SCBI gratings, leading to the fabrication of *stretchable-based* spectrometers, as deeper explained in the next chapter.

4.4 Focusing properties

The high conformability and extremely low surface roughness of the obtained nanocomposite-based optical devices suggest their application to non-optical grade curved surfaces in order to add optical power to the diffracting one. This property is requested in a number of optical mounts [63] for the correction of aberrations like astigmatism or higher order aberrations. In particular a SCBI elastomeric grating was applied to a roughly polished cylindrical surface and the focal length of the curved device measured both on the reflected and on the diffracted beams. Results fully compatible with the expected values were obtained, opening the way to the application of elastomeric optical devices on arbitrarily shaped non-optical grade surfaces for the correction of higher-order images aberrations. Several imaging applications may take advantage of this superior capability of nanocomposite-based diffraction gratings, hyperspectral imaging among them, as extensively discussed in the Conclusions and Perspectives.

LASER & PHOTONICS REVIEWS

Laser Photonics Rev. **7**, No. 6, 1020–1026 (2013) / **DOI** 10.1002/lpor.201300078

ORIGINAL PAPER

Abstract Stretchable and conformable optical devices open up very exciting perspectives for the fabrication of systems incorporating diffracting and optical power in a single element. Supersonic cluster beam implantation of silver nanoparticles in an elastomeric substrate grooved by molding allows effective fabrication of cheap and simple stretchable optical elements able to withstand thousands of deformations and stretching cycles without any degradation of their optical properties. The nanocomposite-based reflective optical devices were characterized both morphologically and optically showing excellent performances and stability compared to similar devices fabricated with standard techniques. The nanocomposite-based devices can therefore be applied to arbitrary curved nonoptical grade surfaces in order to achieve optical power and to minimize aberrations like astigmatism. The high resilience of the nanocomposite material on which the devices are based allows them to be peeled and reused multiple times.

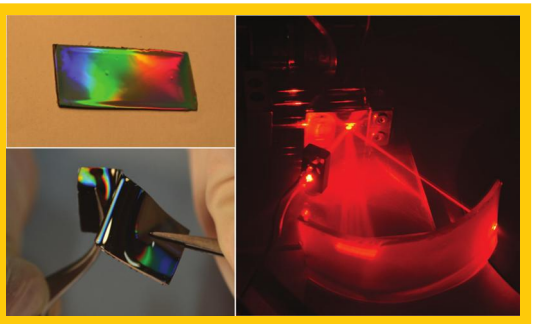

Nanocomposite-based stretchable optics

Cristian Ghisleri[1,2], Mirko Siano[2], Luca Ravagnan[1], Marco Alberto Carlo Potenza[2], and Paolo Milani[1,2,*]

1. Introduction

Adaptive optics is a technology based on optical systems that can dynamically change their shape to compensate for optical artifacts (due to optical aberrations, for example) introduced by the medium between the object and the image [1]. In biological systems (like the human eye) this is obtained by the capability of mechanically changing conformation to "accommodate" for the changes of the optical conditions.

In view of a large number of applications in spectroscopy, microscopy [2, 3], optical telecommunications [4], aerospace [5] and in vivo medical imaging [6, 7], a very strong interest is focused on the fabrication of optical elements such as lenses [2, 8], gratings [9–11], mirrors [3, 4, 6, 7, 12], able to change their geometrical shapes thus improving the image quality. Different alternatives have been proposed for the replacement of rigid optical elements (in particular gratings and mirrors) fabricated on glass or metals with adaptive elements such as electrostatically actuated suspended ribbons forming grating surfaces [13], complex comb-driven diffraction gratings [14] and piezoelectric-driven tunable gratings [15]. These technical approaches are finding applications, however, they are still considered too expensive and technologically complex to allow for a widespread use of adaptive optics solutions [16].

Elastomeric substrates could represent simple, low-cost and effective alternatives for the fabrication of optical elements that can be stretched and deformed. Transparent stretchable optical components operating in transmission mode and made of silicone have been demonstrated for the fabrication of lenses [17], light valves [18], transmission diffraction gratings and wave-front engineering devices [19, 20]. Since these devices work in transmission, light passing through the polymer undergoes absorption, refraction and scattering due to defects in the polymeric matrix.

Despite several attempts, the fabrication of reflective stretchable optical elements consisting of an elastomeric substrate covered by a reflecting metal film is affected by several problems: the metallization of elastomeric substrates by classical thin-film coating techniques (e.g. thermal metal evaporation, e-beam metal evaporation, electrodeposition, etc.) results in a poorly adherent reflecting layer undergoing cracking and delamination, even upon very small deformations [17, 21–24]. The mismatch between the metal and the supporting elastomer mechanical properties causes, also in static conditions, the formation of buckling instabilities and wrinkles on the surface [25–27].

Here, we demonstrate the fabrication of stretchable reflective gratings based on metal–elastomer nanocomposites obtained by supersonic cluster beam implantation (SCBI) in

[1] WISE s.r.l., Piazza Duse 2, 20122 Milano, Italy
[2] CIMAINA, Physics Department, Università degli Studi di Milano, Via Celoria 16, 20133 Milano, Italy
This work is dedicated to the memory of Gabriele Corbelli.
*Corresponding author: e-mail: pmilani@mi.infn.it

© 2013 by WILEY-VCH Verlag GmbH & Co. KGaA, Weinheim

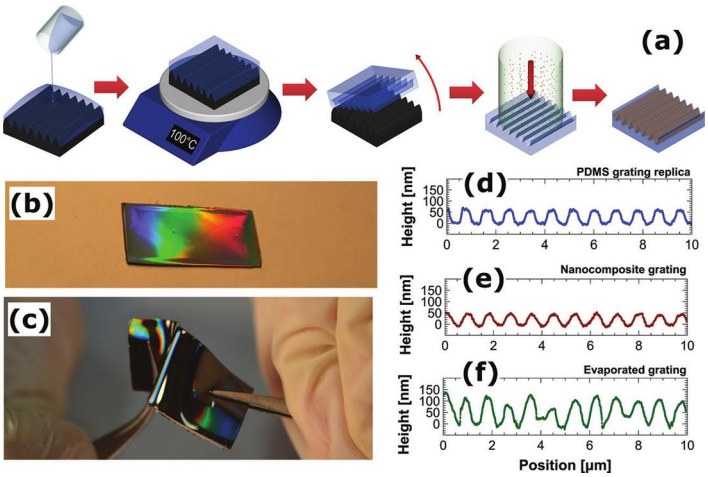

Figure 1 (a) Fabrication process of the PDMS grating replica from a commercial diffraction grating master and subsequent metallization. (b) Picture of the stretchable and deformable reflective diffraction grating. (c) PDMS grating withstanding arbitrary deformations without deterioration. (d), (e), (f) AFM single profiles of the bare PDMS grating, the 60-nm Ag SCBI and the 60-nm Ag thermally evaporated gratings, respectively.

polydimethylsiloxane (PDMS). The implantation of electrically neutral metallic nanoparticles accelerated in a supersonic expansion is a very effective method to metallize a polymer surface with stable and resilient layers [28]. Although the kinetic energy per atom in supersonically accelerated neutral clusters is four orders of magnitude lower than in the case of metal ion implantation in polymers [29], clusters (made of several thousand atoms) have sufficient inertia to penetrate inside the polymeric target and to form a nanocomposite layer, while avoiding charging and carbonization of the polymeric substrate [26, 30]. Metallic electrodes and micropatterns on stretchable substrates deposited by SCBI capable to sustain very large deformations with improving electrical conductance with cyclical deformation have been recently reported [28].

We show that stretchable diffraction gratings obtained by SCBI can easily withstand elongations up to 50% for thousands of cycles with no deterioration of their optical quality and dispersion performances. Moreover, their superior flexibility and resilience allow fitting the gratings upon surfaces of a given shape, thus making very simple and cheap imposing optical power in addition to dispersion properties, as it is currently needed in a number of optical devices [31–35].

2. Grating fabrication and morphological characterization

Transparent gratings were fabricated by making a PDMS replica from a master consisting of a commercial glass holographic diffraction grating (1200 grooves mm^{-1}); the molding procedure is schematically shown in Fig. 1a. PDMS liquid precursor (Sylgard 184 Silicone Elastomer Kit from Dow Corning, mixed in a 10:1 ratio) was cast on the glass diffraction grating and then crosslinked at RT for 48 h. After crosslinking the mold was carefully detached from the master, resulting in a grating with dimensions of about 25 mm × 12 mm and about 1 mm thick.

The transparent PDMS grating was then made reflective by implanting silver nanoparticles by means of a supersonic cluster beam implantation (SCBI) apparatus equipped with a pulsed microplasma cluster source (PMCS) [36, 37]. PMCS consists in a ceramic body with a cavity in which a solid silver target (purity 99.9%) is vaporized by a localized electrical discharge supported by a pulsed injection of an inert gas (He or Ar) at high pressure (40 bar). The metal atoms, sputtered from the target, aggregate in the source cavity to form metal clusters; the mixture of clusters and inert gas expands through a nozzle forming a supersonic beam into an expansion chamber kept at a pressure of about 10^{-6} mbar. Electrically neutral nanoparticles exiting the PMCS are aerodynamically accelerated in a highly collimated beam with divergence lower than 1° and with a kinetic energy of roughly 0.5 eV $atom^{-1}$ [28]. The central part of the cluster beam enters, through a skimmer, a second vacuum chamber (deposition chamber) where the beam is intercepted by the polymeric substrate. A raster of the nanoparticle beam on the PDMS grating is obtained by a computer-controlled motorized substrate holder during the implantation process. The measure of the quantity of material implanted into the PDMS is obtained by placing a half-masked hard substrate (glass or silicon) next to the grating, during the implantation process, in order the intercept the same number of nanoparticles. The thickness of the cluster-assembled film deposited on the hard substrate corresponds to the equivalent thickness t_{eq} in the case of the metal–polymer nanocomposite. We metallized different PDMS gratings and plane PDMS substrates with different equivalent thicknesses, up to 160 nm, with a deposition rate of about 0.08 Å s^{-1}. The deposition rate was calculated as the ratio between the final equivalent thickness and the overall implantation time on an area of 750 mm^2 required for a homogeneous implantation of the substrate.

© 2013 by WILEY-VCH Verlag GmbH & Co. KGaA, Weinheim

A reflective grating with t_{eq} of 60 nm is shown in Fig. 1b: it can be stretched and deformed without altering the macroscopic optical quality of the surfaces (Fig. 1c). Figure S1 in the Supporting Information Section shows a scanning electron microscopy image of the nanocomposite grating surface. The surface roughness of the nanocomposite is much smaller than the pitch of the grating and the light wavelength in the visible range, thus not affecting the optical properties of the device.

In order to compare the performance of the nanocomposite grating with devices obtained with a traditional approach, we metallized PDMS gratings with silver and gold films at different thicknesses using a standard thermal evaporation method. In particular, we produced PDMS gratings with 26-nm and 60-nm thick silver and 26-nm thick gold metallic layers with a deposition rate of about 0.6 Å s^{-1}. We characterized the diffracting side of bare and metallized PDMS gratings by atomic force microscopy (AFM): Fig. 1d shows an AFM single line scan of the profile of the bare PDMS grating, presenting a sinusoidal shape with a peak-to-valley height of about 50 nm and a pitch of 833 nm, exactly reproducing the features of the master, having a groove density value of 1200 grooves mm^{-1}. Figure 1e reports the same single line scan taken on the PDMS grating metallized by SCBI: an excellent reproduction of the bare profile is observed, while the profile relative to the 60 nm Ag thermally evaporated PDMS grating (Fig. 1f) shows a more irregular profile compared to the nanocomposite grating. The deposition rate used for classical metallization produced surfaces with a better morphology (see Figs. S2 and S3 of the Supporting Information Section) compared to what has been reported in the literature [21,26,27], however, the wrinkling of the surface has dimensions comparable with the grating pitch.

The difference in the peak-to-valley height between the two metallization techniques may be partly due to the high divergence of the thermally evaporated metal atoms causing a shadowing effect and hence a nonuniform coating of peaks and valleys. The very low divergence of nanoparticles accelerated in a supersonic beam results in a high lateral resolution of the implanted layer, allowing the very precise reproduction of submicrometer grooves [38,39].

3. Optical characterization

In order to characterize the optical performances of the gratings, we performed different experiments, aimed to test i) the reflectance of the nanocomposite ii) the grating response under controlled uniaxial stretching. For the optical characterization three silver SCBI and two silver evaporated gratings (respectively named C1, C2, C3 and E1, E2) were tested.

The reflectance of the silver–PDMS nanocomposite was measured on plane, mirror-like, silver implanted samples. A 45° incident white-light beam from a halogen lamp was reflected by the sample into a monochromator (coupled with a CCD camera for the spectral acquisition), while a standard mirror was used as reference. Figure 2 shows the visible-NIR reflectance of a SCBI silver nanocomposite (t_{eq} = 60 nm) compared with a thermally evaporated silver-PDMS mirror (t = 30 nm) and gold-PDMS mirror (t = 26 nm). A t_{eq} of 60 nm provides the best reflectance among all the tested nanocomposites with different equivalent thicknesses. Larger amounts of implanted nanoparticles lead to the increase of light absorption due to surface plasmon resonance, thus modifying the reflectance spectrum of the surface [40,41]. By further increasing the equivalent thickness, nanoparticles saturate the polymer and begin to grow on the surface of the polymer, forming a thick layer undergoing larger cracking and thus causing a loss of reflectance of the device.

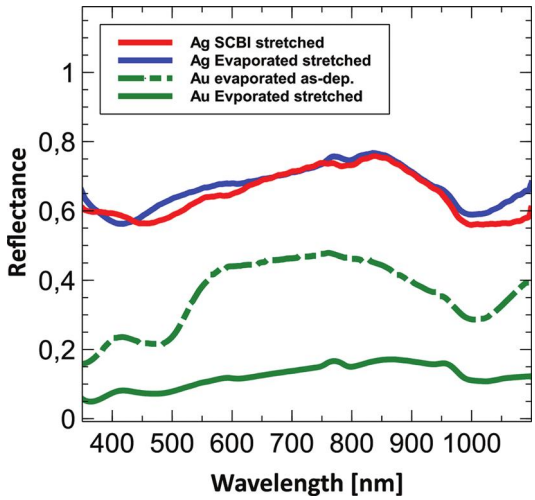

Figure 2 VIS-NIR reflectance (350–1100 nm) with 45° incident white light for the 60-nm Ag SCB Implanted (red line) and the 26-nm Ag evaporated (blue line) PDMS mirrors after peeling and stretching. The lower green lines represent the reflectance of a 26-nm Au evaporated PDMS mirror before (dashed) and after peeling and stretching (solid).

We also characterized stretchable devices obtained by gold evaporation since in the literature the use of gold coating has been reported for the fabrication of tunable diffraction gratings [42]. All the mirrors underwent several mechanical stresses due to manipulation and peeling from the sample holder prior to the measurement, followed by 3000 cycles of uniaxial stretching at 50% of elongation. The implanted and evaporated silver mirrors (blue and red lines) exhibit a similar reflectance, not undergoing significant modifications after stretching, whereas the gold mirror showed a severe deterioration (green solid line), due to the poor adhesion of gold on PDMS. In Fig. S2 we reported optical microscope images of a 26-nm thick gold film deposited on a flat PDMS surface and on a PDMS grating. The peeling of the gold evaporated polymeric film from the sample holder is sufficient to cause deterioration of the

© 2013 by WILEY-VCH Verlag GmbH & Co. KGaA, Weinheim

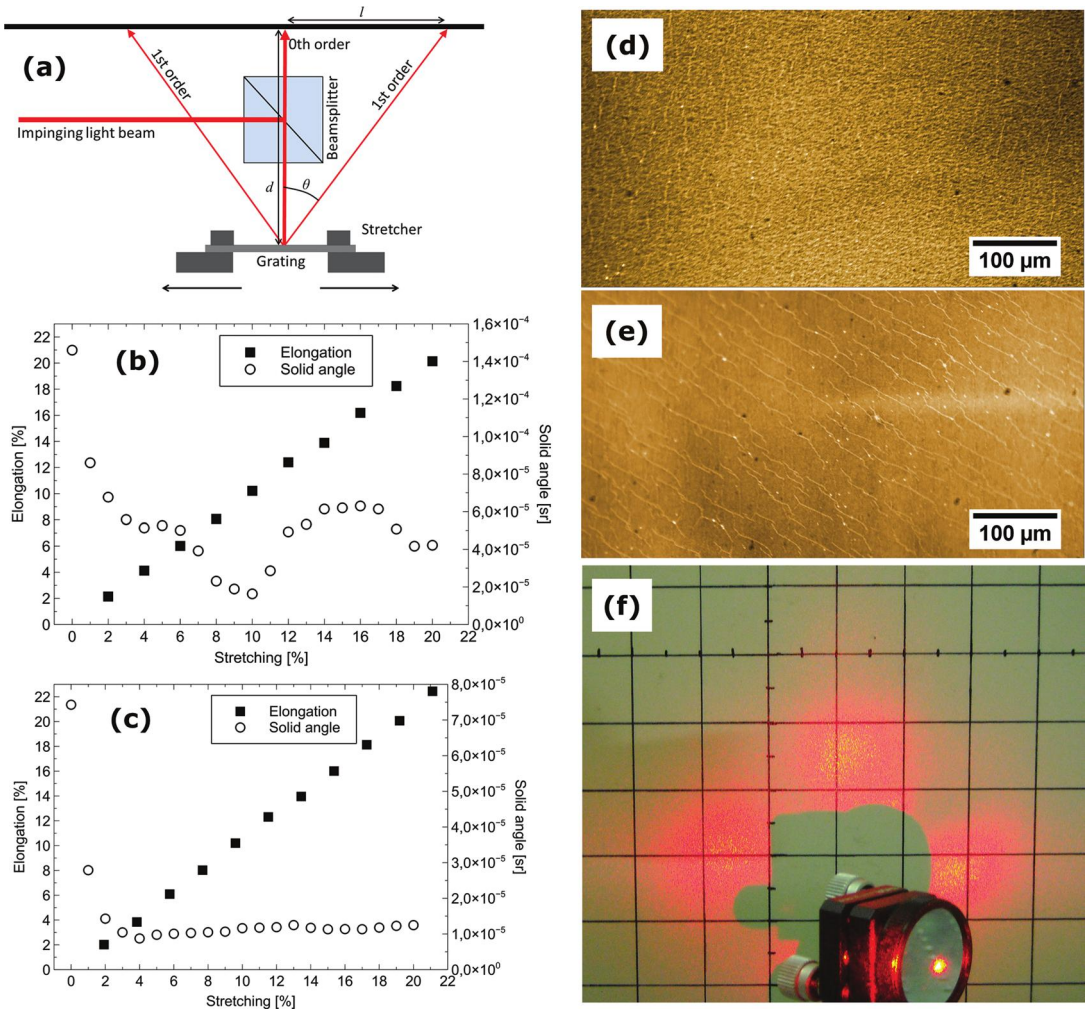

Figure 3 (a) Schematics of the optical layout used to characterize the stretched gratings. (b) and (c) show results obtained by stretching 60-nm Ag evaporated and 60-nm Ag SCBI gratings, respectively, after 10 000 stretching cycles. Horizontal scales show the stretching imposed to the gratings (%). Left vertical scale represents the elongation of the grooves spacing; right vertical scale represents the solid angle subtended by the diffracted spot. (d) and (e) show the surfaces of the evaporated and the SCBI gratings respectively after ten thousand stretching cycles, as seen at the optical microscope (20× magnification). (f) Diffraction pattern of the silver evaporated elastomeric grating. The two spots in the horizontal direction are due to the grooves of the grating, while the unwanted vertical spots (the symmetric spot is present but hidden by the mirror mount) are due to the uncontrolled cracking of the superficial metal layer of the grating. These vertical spots are not present in the case of the SCBI grating.

surface, while after 3000 cycles at 50% stretching the surface is completely covered by cracks.

For the characterization of the behavior under uniaxial stretching we only considered silver implanted (C2, t_{eq} = 60 nm) and evaporated (E2, t = 60 nm) reflective gratings. The gratings were clamped on a custom-built motorized uniaxial stretcher with the periodic structure of the grating perpendicular to the stretching direction. A monochromatic light beam (coming from a He-Ne laser, wavelength $\lambda = 632.8$ nm, power $P = 1$ mW) is sent through a cubic beam splitter, normally to the entrance face. The 90° reflected beam impinges normally onto the center of the free-standing clamped elastomeric grating (Fig. 3a). The position l of the spot of the 1st-order diffracted beam respect to the one relative to the 0th order on a screen at a distance d from the grating is related to the diffraction

© 2013 by WILEY-VCH Verlag GmbH & Co. KGaA, Weinheim

angle θ through the following equation, obtained from simple geometrical considerations:

$$\theta = \arcsin\left(\frac{l}{d}\right) \tag{1}$$

Both l and d were manually measured with a precision ruler, the distances being of the order of 100 mm. The elastomeric grating was stretched stepwise up to a 25% maximum extension, and for each step the corresponding value of l has been determined. Both the size and shape of the diffracted spot at the screen have also been characterized.

An example of the experimental results after 10 000 thousands stretching cycles for E2 and C2 is shown in Figs. 3b and c. In both cases (evaporated and SCBI) they show the expected linearity of the grating response as a function of the stretching. Besides, the solid angle subtended by the diffracted spot at the screen is reported for each case, showing a good stability overall the elongation range for the nanocomposite grating, while the evaporated one shows large fluctuations. In both cases, a small elongation is needed to reduce the spread of the diffracted light at rest position. Similar results have been obtained for all the tested gratings.

The superior resilience of SCBI gratings compared to evaporated ones is evident after thousands of stretching cycles. The optical microscope image of the surface of the evaporated grating after ten thousand stretching cycles (Fig. 3d) shows an evident cracking of the rigid metal layer both in the stretching and the orthogonal directions, causing the rapid increase of stray light and the arise of unexpected diffraction beams perpendicular to the stretching direction (Fig. 3f). The surface of the SCBI grating (Fig. 3e) presents only minor cracks, not affecting the optical quality of the device. The grating mounted on the uniaxial stretcher can be exploited to fabricate a very simple and cheap "linear" alternative to traditional rotating grating monochromators [31] as shown in the Supporting Information (Fig. S4 and the videoclip).

After a few weeks from fabrication both the implanted and the evaporated silver gratings underwent deterioration due to silver oxidation. In order to avoid this problem we deposited a very thin PDMS layer (about 10 μm thick) by spin coating on the metallized gratings in order to reduce oxygen exposure. The use of a capping layer is detrimental to the optical quality of the evaporated silver grating, even at very low metal thicknesses, as we report in Fig. S3 in the Supporting Information.

The stretchability and good resilience of the silver nanocomposite gratings allow them to be fitted to curved surfaces, thus adding optical power to the diffracting element. The following test, regarding the application of the stretchable grating to a cylindrical surface, is a benchmark for a number of possible applications in which the gratings are used to modify the wavefronts of the emerging beam, both in traditional and adaptive optics applications [31, 32]. For example, this can be used to compensate for aberrations, to limit the number of optical elements within a device and to cut down the fabrication costs of concave or arbitrary shaped gratings, currently used in a number of grating mounts [31]. The breakthrough here is represented by the separate production of identical conformable diffractive elements with an optical-grade surface to be subsequently adapted to rigid substrates with different shapes and curvatures. This can revolutionize the fabrication of different optical systems: producing arbitrarily curved and nonoptical grade shaping surfaces with traditional or computer numerical control (CNC) machines is much easier and cheaper than blazing a curved optical-grade surface [31].

For the proof-of-principle of this approach, we have chosen cylindrical surfaces in order to preserve the spacing between the grooves over all the grating extension. It should be noted that this is rigorously true regardless of the grooves' orientation over the surface, thanks to the perfect Euclidean geometry of cylindrical surfaces. The astigmatism of the system can be exploited either to compensate for aberrations, or in connection with other cylindrical surfaces with optical power in the orthogonal direction to give a spherical shape to the wave front.

The experiments were performed by sticking a SCBI stretchable grating onto the surface of a cylinder of radius $R = 164$ mm machined from an aluminum piece with no optical finishing of the surfaces. Figure 4a shows a sketch of the optical layout, with the grooves of the grating in the vertical direction, parallel to the rotation axis of the cylindrical surface. The plane wave front of a collimated laser beam impinges onto the surface of the grating, from which it is diffracted. In Fig. 4b a picture of the impinging, reflected and diffracted beams is shown, where the beam paths are evidenced by light scattered from vapors of liquid nitrogen. Due to the cylindrical shape of the surface, the system is endowed with a pure astigmatic optical power in the tangential direction, the curvature being vanishing in the other, so that the sagittal focal length is infinite (see Fig. 4a). The 0th and 1st diffraction orders have been collected with a CCD camera along the corresponding propagation directions, and the intensity distributions recorded at several distances from the grating. The sizes of the diffracted spots have been measured and the divergence provided a measure of the tangential focal length of the system. These results are compared to that obtained from basic optics: with R the cylinder radius, α and β the incidence and diffraction angles, the tangential focal length is given by [31, 43]:

$$f = R\frac{\cos^2\beta}{\cos\alpha + \cos\beta} \tag{2}$$

Note that, due to the finite thickness of the gratings, the deformation determines a slight change in the grooves' spacing, from 2.5 $\pm$0.2% to 3.5 $\pm$0.2% depending on the grating thickness. In Table 1 we report the results of measurements obtained from 20 positions for each grating, operated at the 0th and the 1st diffraction orders, compared with the theoretical expectations.

We have also performed an experiment where the laser beam is spatially filtered and expanded up to a diameter of

© 2013 by WILEY-VCH Verlag GmbH & Co. KGaA, Weinheim

Table 1 The effective focal lengths compared to the expected theoretical ones for 5 gratings. E1 and E2 indicate Ag thermally evaporated gratings (with 123 nm and 60 nm thick metal layers, respectively) while C1, C2 and C3 are the Ag SCBI gratings (with an equivalent thickness of 85, 60 and 140 nm, respectively). These results are the averages of a number of measurements in different positions of the gratings, from which we estimated the errors reported here.

Grating	0th-order experimental [mm]	0th-order theoretical [mm]	1st-order experimental [mm]	1st-order theoretical [mm]
E1	9.48 ± 0.73	7.2	8.61 ± 0.89	8.2
E2	8.06 ± 2.48	7.2	7.32 ± 2.53	8.3
C1	7.22 ± 0.47	7.2	8.85 ± 1.11	8.2
C2	7.82 ± 0.90	7.2	8.56 ± 1.46	8.2
C3	7.78 ± 0.62	7.2	8.95 ± 1.57	8.2

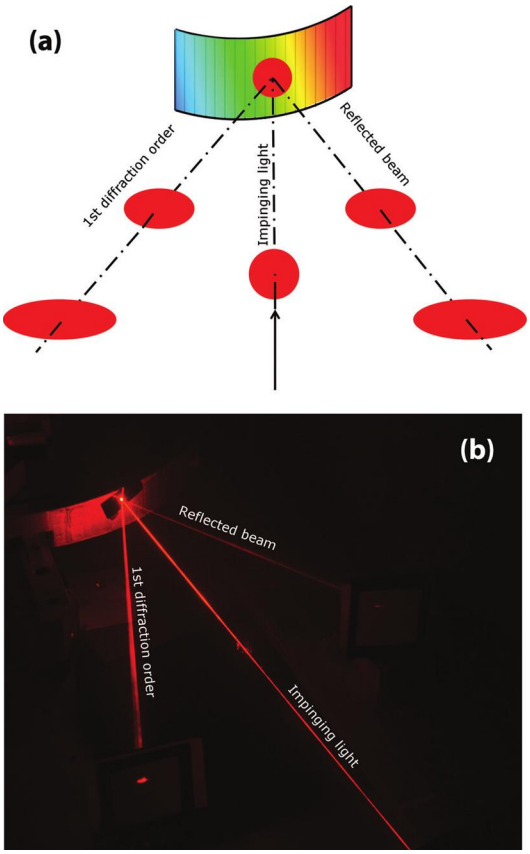

Figure 4 (a) The optical layout for the characterization of the optical power imposed by the cylindrical surface. (b) A picture of the optical bench, showing the impinging beam, the reflected and the 1st diffracted order.

10 mm approximately, then passed through a focusing lens and finally impinging onto the grating well before the focal region. The focusing conditions are chosen in such a way that a beam collimated in the horizontal direction emerges from the grating. The intensity profiles of the first-order diffraction beam have been monitored by a CCD camera at different positions along the optical axis, passing through the focal plane of the lens. The transversal intensity profiles showed the expected behavior, the beam being sharply focused along the vertical direction only.

4. Conclusions

In summary, we have shown that stretchable reflective optical gratings can be easily fabricated by supersonic cluster beam implantation in PDMS. The reflectance and resilience of the coating resulting from the implantation of nanoparticles in the elastomer guarantee the stability of the optical performances upon thousands of deformations of the grating up to the 50% of the original dimensions. Stretchable and conformable optical gratings open novel and very exciting perspectives for the fabrication of optical devices incorporating diffracting and optical power in a single element. Starting from nonoptical grade curved surfaces, one can fabricate optical elements by sticking stretchable gratings or mirrors fabricated by SCBI metallization of cheap replica molded and identical PDMS substrates. Furthermore, the superior stability and durability of the SCBI stretchable optical elements allows the peeling and reuse of the devices on different surfaces with arbitrary shape and curvature without compromising their optical quality.

Acknowledgements. The authors would like to thank Marco Indrieri for AFM measurements, Francesco Cavaliere and Daniele Viganò for the fabrication of the mechanical supports, Andrea Bellacicca for the development of the electronics in the miniaturized stretcher and Davide Marchesi for his assistance in the SEM characterization. (Supporting Information is available online from Wiley InterScience or from the author).

Supporting information for this article is available free of charge under http://dx.doi.org/10.1002/lpor.201300078

Received: 5 June 2013, **Revised:** 19 July 2013, **Accepted:** 19 August 2013

Published online: 10 September 2013

© 2013 by WILEY-VCH Verlag GmbH & Co. KGaA, Weinheim

Key words: Deformable optics, stretchable optics, nanocomposite materials, polymeric materials, stretchable gratings.

References

[1] D. R. Williams and J. Porter in Adaptive Optics for Vision Science: Principles, Practices, Design and Applications, edited by J. Porter, H. Queener, J. Lin, K. Thorn, and A. A. S. Awwal, (John Wiley & Sons, Hoboken, NJ, USA 2006), Ch. 1.
[2] B. F. Grewe, F. F. Voigt, M. van 't Hoff, and F. Helmchen, Biomed. Opt. Exp. **2**(7), 2035 (2011).
[3] O. Albert, L. Sherman, G. Mourou, T. B. Norris, and G. Vdovin, Opt. Lett. **25**(1), 52 (2000).
[4] F. Druon, G. Chériaux, J. Faure, J. Nees, M. Nantel, A. Maksimchuk, G. Mourou, J. C. Chanteloup, and G. Vdovin, Opt. Lett. **23**(13), 1043 (1998).
[5] M. Booth, M. Neil, and T. Wilson, J. Opt. Soc. Am. A **19**, 2112 (2002).
[6] A. Iqbal and F. B. Amara, Int. J. Optomechatron. **1**, 180 (2007).
[7] E. J. Fernández, I. Iglesias, and P. Artal, Opt. Lett. **26**(10), 746 (2001).
[8] H. Oku and M. Ishikawa, Appl. Phys. Lett. **94**, 221108 (2009).
[9] O. Solgaard, F. S. A. Sandejas, and D. M. Bloom, Opt. Lett. **17**(9), 688 (1992).
[10] D. W. Carr, J. P. Sullivan, and T. A. Friedmann, Opt. Lett. **28**(18), 1636 (2003).
[11] M. Aschwanden and A. Stemmer, Opt. Lett. **31**(17), 2610 (2006).
[12] J. P. Déry, E. F. Borra, and A. M. Ritcey, Chem. Mater. **20**(20), 6420 (2008).
[13] C. S. Gudeman, C. B. Carlisle, J. Hunter, R. W. Corrigan, R. J. Monteverde, and J. I. Trisnadi, Proc. SPIE **4653**, 56 (2002).
[14] A. A. Yasseen, S. W. Smith, F. L. Merat, and M. Mehregany, IEEE J. Sel. Top. Quantum Electron. **5**, 75 (1999).
[15] C. W. Wong, Y. Jeon, G. Barbastathis, and S.-G. Kim, Appl. Opt. **42**, 621 (2003).
[16] R. A. Guerrero, M. W. C. Sze, and J. R. A. Batiller, Appl. Opt. **49**(19), 3634 (2010).
[17] J. L. Wilbur, R. J. Jackman, G. M. Whitesides, E. L. Cheung, L. K. Lee, and M. G. Prentiss, Chem. Mater. **8**, 1380 (1996).
[18] B. Grzybowsky, D. Qin, R. Haag, and G. M. Whitesides, Sens. Actuators, A **86**, 81 (2000).
[19] J. A. Rogers, O. J. A. Schueller, C. Marzolin, and G. M. Whitesides, Appl. Opt. **36**(23), 5792 (1997).
[20] Y. Xia, E. Kim, X.-M. Zhao, J. A. Rogers, M. Prentiss, and G. M. Whitesides, Science **273**(5273), 347 (1996).
[21] I. M. Graz, D. P. J. Cotton, and S. P. Lacour, Appl. Phys. Lett. **94**, 071902 (2009).
[22] O. Graudejus, B. Morrison, C. Goletiani, Z. Yu, and S. Wagner, Adv. Funct. Mater. **22**(3), 640 (2012).
[23] N. J. Douville, Z. Li, S. Takayama, and M. D. Thouless, Soft Matter **7**, 6493 (2011).
[24] C. L. Tuinea-Bobe, P. Lemoine, M. U. Manzoor, M. Tweedie, R. A. D'Sa, C. Gehin, and E. Wallace, J. Micromech. Microeng. **21**, 115010 (2011).
[25] N. Bowden, S. Brittain, A. G. Evans, J. W. Hutchinson, and G. M. Whitesides, Nature **393**, 146 (1998).
[26] S. Rosset and H. R. Shea, Appl. Phys. A **110**, 281 (2013).
[27] J. Y. Chung, A. J. Nolte, and C. M. Stafford, Adv. Mater. **23**, 349 (2011).
[28] G. Corbelli, C. Ghisleri, M. Marelli, P. Milani, and L. Ravagnan, Adv. Mater. **23**(39), 4505 (2011).
[29] S. Rosset, M. Niklaus, P. Dubois, and H. R. Shea, Adv. Funct. Mater. **19**, 470 (2009).
[30] R. Cardia, C. Melis, and L. Colombo, J. Appl. Phys. **113**, 224307 (2013).
[31] C. Palmer, E. Loewen, in Diffraction Grating Handbook, 6th ed. Newport Corporation, USA (2005), Ch. 7.
[32] T. K. Gaylord and M. G. Moharam, Proc. IEEE **73**(5), 894 (1985).
[33] N. Zhu and T. Mei, Opt. Commun., doi: 10.1016/j.optcom.2013.02.032 (2013).
[34] D. Fattal, J. Li, M. Fiorentino, Z. Peng, and R. G. Beausoleil, Group IV Photonics (GFP), 2010 7th IEEE International Conference on, 37 (2010).
[35] D. Fattal, J. Li, M. Fiorentino, Z. Peng, and R. G. Beausoleil, Nature Photon. **4**, 466 (2010).
[36] E. Barborini, P. Piseri, and P. Milani, J. Phys. D: Appl. Phys. **32**, L105 (1999).
[37] K. Wegner, P. Piseri, H. V. Tafreshi, and P. Milani, J. Phys. D: Appl. Phys. **39**, R439 (2006).
[38] E. Barborini, P. Piseri, A. Podestà, and P. Milani, Appl. Phys. Lett. **77**(7), 1059 (2000).
[39] P. Piseri, A. Podestà, E. Barborini, and P. Milani, Rev. Sci. Instrum. **72**, 2261 (2001).
[40] V. Amendola, O. M. Bakr, and F. Stellacci, Plasmonics **5**, 85 (2010).
[41] K. Chatterjee, S. Banerjee, and D. Chakravorty, Phys. Rev. B **66**, 085421 (2002).
[42] M. Aschwanden and A. Stemmer, Proc. SPIE **6524**, 65241N (2007).
[43] H. G. Beutler, J. Opt. Soc. Am. **35**(5), 311 (1945).

© 2013 by WILEY-VCH Verlag GmbH & Co. KGaA, Weinheim

CHAPTER 5

A simple scanning spectrometer based on a stretchable reflective grating

Deformable optical elements (lenses, mirrors and gratings) are fundamental ingredients for the fabrication of a novel class of compact, inexpensive and portable devices based on adaptive optics. In particular the use of tunable gratings based on stretchable reflective substrates could revolutionize the design of optical miniature spectrometers and widen significantly the field of applications. In standard spectrometers a rigid grating spatially separates spectral components of diffracted light which can be either detected simultaneously by an array of photodetectors, or swept through a photodetector slit by one or more rotating elements. Both solutions are based on the so-called Czerny-Turner optical configuration [63] allowing a compact design consisting of two concave mirrors and one flat diffraction grating. This approach is very effective, however it requires the use of a quite sophisticated and expensive solutions in terms of detectors and/or mechanical mountings.

In this chapter a low-cost spectrometer operating in the visible range and based on Supersonic Cluster Beam implanted elastomeric diffraction gratings is presented. The mechanical properties of the elastomeric grating are exploited to select the wavelength of the light diffracted at a given angle respect to the normal of the grating, simply by imposing an increase of the pitch through a stretching of the device. This mount is particularly demanding in terms of durability of the elastomeric optical element since it needs to operate at huge number of cycles of strains up to approximately 100% of the initial size while maintaining diffraction efficiency, dispersion performances, and grooves quality. This particular application of elastomeric optical devices can be considered a good benchmark for an extended class of applications, including adaptive optics for spectroscopy, microscopy, and ophthalmology, as seen in the first chapter.

5.1 Grating fabrication

The polymeric substrate for the stretchable grating (30 mm long and 10 mm wide) was fabricated as described in detail in ref. [23]. Briefly the back of a commercial DVD (grooves pitch 740nm) was used as a master for the molding of the PDMS (Sylgard 184 from Dow Corning, in a 1:10 ratio) substrate, obtaining a transparent elastomeric diffraction grating. The transparent PDMS grating was then made reflective by Supersonic Cluster Beam Implantation of Ag nanoparticles at a rate of $8 \cdot 10^{-3} nm \cdot s^{-1}$ up to an equivalent thickness of approximately 60nm. In order to avoid oxidation of the silver nanoparticles and to facilitate the handling of the device, the metallized grating was coated with a second thin layer of PDMS (capping layer) deposited by spin coating at 3500rpm for 60s, reaching a thickness of about $10\mu m$, and cured at RT for 48 hours.

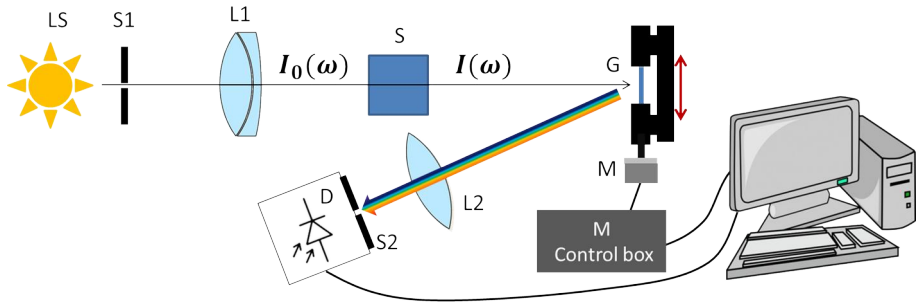

Figure 5.1: Optical setup of the spectrophotometer based on the elastomeric grating

The stretchable reflective grating was then clamped on a homemade stretcher consisting in a computer-controlled stepper motor coupled with a micrometric traslator, the whole system able to minimum movements of $2.5\mu m$, as described in [21].

The optical properties of these gratings have been accurately characterized in [23] and they proved to be stable enough for operating after a huge number of strain cycles. Performances of these gratings were also compared to those of identical substrates covered by means of traditional evaporation of silver (gold evaporation produces fast deterioration due to a poor adhesion of gold on PDMS, as shown in [23]).

5.2 Optical setup

The scanning spectrometer based on the stretchable grating is schematically shown in Figure5.1, with the aim of reducing the cost and the number of optical elements involved, as well as its dimensions. A light source (LS) has been placed close to a vertical slit (S1) 0.01x$5mm^2$ wide. An achromatic doublet (L1, $f = 100mm$) produces a beam spatially coherent in the horizontal direction, impinging normally onto the surface of the grating (G), with the grooves accurately placed in the vertical direction, after passing through the sample (S). The first order diffracted beam, collected by a lens at an angle of $27°$ ($L2, f = 100mm$), is focused into the collection slit (S2: 0.5x$5mm^2$ wide, vertically positioned) and then falls onto the detector (D). The detector consists in a cheap, multipurpose BPX65 photodiode equipped with a custom-made electronics aiming to amplify the signal while filtering high frequency electrical noises. Such a layout determines an ultimate resolution of about $2.5nm$ overall the wavelength range because of diffraction limits. The grating is stretched by a stepping motor (M) controlled by a PC. Steps of 0.1% up to 100% of the overall grating length have been applied, the stretching being continuously monitored to determine the wavelength of the collected light. The time sequence of the light intensity is measured synchronously to the stretching, thus obtaining the sequence of wavelengths sensed by the system.

Note that this system does not need any rotating stage, at variance with traditional monochromators, thus requiring a substantially simpler and straightforward mechanical mounting. The capability of spanning the whole spectrum by simply stretching the grating represents the main breakthrough of this system.

	$p1$ [nm]	$p2$ [nm]	$p3$	R^2
Extension	$5.504 \cdot 10^{-4}$	-0.1761	-1.4137	0.99986
Retraction	$5.096 \cdot 10^{-4}$	-0.1331	-12.0995	0.99989

Table 5.1: Fit parameters extracted from the quadratic fit of the calibration procedure. R^2 represents the regression coefficient.

5.3 Calibration

As a reference for the calibration of the spectrometer we acquired the spectrum of a Hg lamp, whose spectrum and emission peak positions are tabulated in [139]. By stretching the grating up to 100% all the 5 main emission peaks in the visible range are well detectable and can be easily identified. In Figure5.2 we show the results obtained with our spectrometer operated with the photodiode previously described. The showed spectra are the average of 20 acquisitions, both for extension and retraction of the stretchable grating. It is worth noting that the extension and retraction cycles do not perfectly coincide both in wavelength and in the relative intensities. This can be explained with the relaxation time needed by the polymeric chains of the substrate to rearrange after stretching. As a consequence, different calibrations for the extension and retraction cycles are needed. Data showing the wavelength of the peaks as a function of the stretching applied are reported in Figure5.2b and can be fitted with a quadratic equation $\varepsilon = p1 \cdot \lambda^2 + p2 \cdot \lambda + p3$, where λ indicates the wavelength, ε the percentage strain applied to the grating. The results for the fit coefficient $p1$, $p2$ and $p3$ relative to the extension and retraction cycles are reported in table 5.1 and are used for the determination of the wavelength in the next measurements. The relationship occurring between ε and λ is almost linear since the quadratic term p_1 is very small respect to p_2 and p_3. Unlike the most of available commercial instruments, our spectrometer can be thus considered as a linear monochromator. According to this calibration, by stretching the grating up to 100% we are able to span a wavelength range between $350nm$ and $620nm$ with minimum steps of $0.3nm$ (i.e. 0.1% of strain).

The spectral resolution is approximately $4 - 5nm$, close to the ultimate resolution of the optical device. The resolution is limited by the non-perfect shape of the reflecting surface that is affected by small local deformations changing with the stretching force. Works are in progress to understand the limitations imposed by these features that are ultimately related to the flexible nature of the elastomeric substrate. Moreover, since the grating consists in the replica of a DVD surface, some defects on the grooves structure can be present and the grooves are not linear but curved. The light spot impinging on the grating has a diameter of 6 millimeters and thus the diffracted beams, entering the photodiode through the vertical linear slit, are affected by the curvature of the grating lines, limiting the final resolution of the spectrum.

5.4 Spectra acquisition

As a benchmark, we have performed the analysis of the extinction spectrum of Rhodamine B dye, presenting a sharp and highly intense absorption peak at $543.6nm$ [140]. The extinction spectrum has been acquired and compared with the spectrum of the same sample acquired with a commercial spectrophotometer (Jasco 7850) and with data reported in literature [140]. A $3.2 \cdot 10^{-4}M$ solution of Rhodamine B in ethanol has been prepared in a quartz cuvette with an optical path of $10mm$ for the analyses.

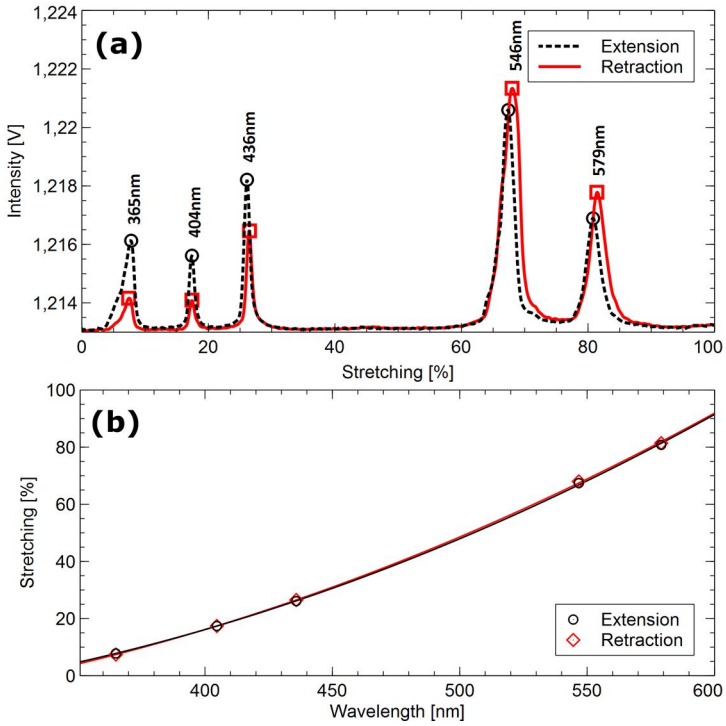

Figure 5.2: (a) Hg lamp spectra taken with the SCBI grating stretched up to 100%. Extension and retraction spectra are not coincident due to delay in the response of the polymer when released. Square and circles highlight the peaks, for extension and retraction spectra respectively, used for the calibration of the device while numbers indicate the reference wavelengths from [139] (b) Peaks position in terms of grating stretching (black circles for extension, red squares for retraction) and quadratic fit (solid black line for extension, red dotted line for retraction).

Extinction spectra of Rhodamine B have been acquired by stretching the grating up to 100% and acquiring first the light intensity transmitted by the ethanol ($I_0(\omega)$, the reference spectrum), then the light intensity transmitted by the dye ($I(\omega)$). The extinction spectra $A(\omega)$ have been calculated as follows:

$$A(\omega) = -\log_{10} \frac{I(\omega)}{I_0(\omega)} \tag{5.1}$$

The intensities $I_0(\omega)$ and $I(\omega)$ used in equation 5.1 for the determination of the absorbance are the average of 20 spectra both for ethanol and rhodamine B solution. The baseline values of the two spectra were measured as the mean of 1000 intensity values acquired applying a 100% strain to the grating, and subtracted from $I_0(\omega)$ and $I(\omega)$. The obtained absorbance spectra were then appropriately smoothed by means of a spline procedure.

The results in Figure5.3a show peaks at $545.0nm$ and $545.3nm$ for the extension and retraction cycles respectively, in good agreement with the data reported in literature ([140], black continuous line). Despite the differences in the spectra of the Hg lamp shown in Figure5.2, the two spectra of the Rhodamine B acquired during the extension and retraction cycles coincides, thanks to the different calibrations used in the two

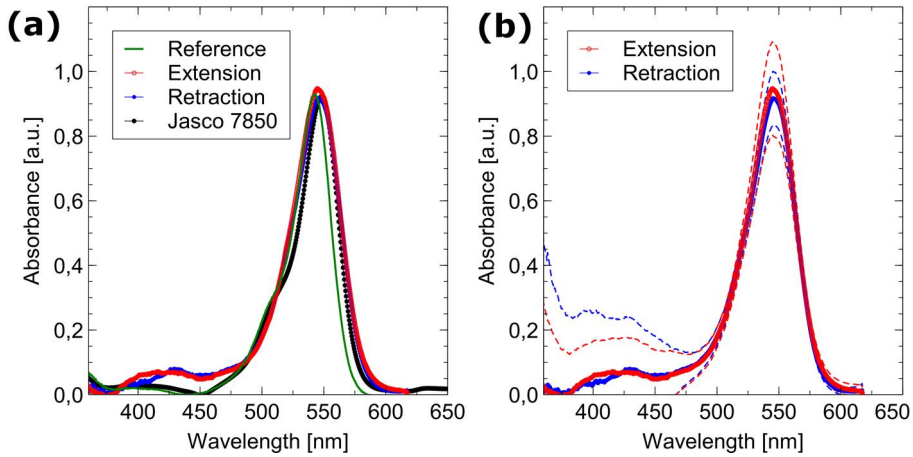

Figure 5.3: (a) Absorption spectra for Rhodamine B dye with a concentration of $3.2 \cdot 10^{-4} M$. Extension and retraction spectra acquired with the photodiode are perfectly coincident (solid green and blue lines) and the peak wavelength of 545.0nm and 545.3nm are comparable with the wavelength peak of reference spectrum [140] (dotted black line, 543.6nm). The same sample was also analyzed with a commercial Jasco 7850 Uvvis spectrophotometer (dash-dot red line), showing a peak position of 548.0nm. The broadening of the spectra taken with SCBI grating is mainly due to the curvature and slight tilt of the diffracted lines caused by the geometry of the grating grooves that is replicated from a DVD with curved lines. (b) The same extension and retraction absorption spectra with the associated uncertainties (dashed red and blue lines).

cases. The spectrum acquired with the commercial spectrophotometer is characterized by a shape similar to the one reported in literature, with a shift in the peak position to $548.0nm$. The slightly larger broadening of the spectra obtained with the stretchable grating can be explained with the nature of the grating itself, as mentioned above.

Similar absorbance peak intensities are measured between the extension and retraction cycles and the spectrum measured with the spectrophotometer as well. The small differences of the peak intensity abundantly fall in the uncertainty, showed in Figure5.3b. Here only the extension and retraction spectra with the relative uncertainties are shown, with the same scale of Figure5.3a, for sake of clarity. The uncertainties are obtained by propagating the point-by-point standard deviation of the ethanol and rhodamine spectra in the extension or retraction cases. It is worth noting that the uncertainties largely increase for shorter wavelengths (and thus for low stretching percentages). This behavior is due to the measure of the baseline subtracted from the original averaged ethanol and rhodamine spectra and to the high electrical noise detected by the photodiode during spectra acquisition. In Figure5.4a the averaged ethanol and rhodamine extension spectra before the baseline subtraction are reported. At low stretching percentages the two spectra should coincide since the transmittance of rhodamine is expected to be unitary. However a slight difference is observed, as can be clearly seen in the magnification of the first part of the spectra shown in Figure5.4b. This difference, of the order of approximately $2 \cdot 10^{-4} V$, can be eliminated by subtracting the baselines relative to the two samples. Nevertheless the electrical noise read by the photodiode during the acquisition of the baseline, shown in Figure5.4c, is high, being the fluctuations of intensity even larger than the difference between the two spectra, of the order of $4 \cdot 10^{-4} V$. This may lead to larger uncertainties of the first part of the absorption spectrum, once the mean

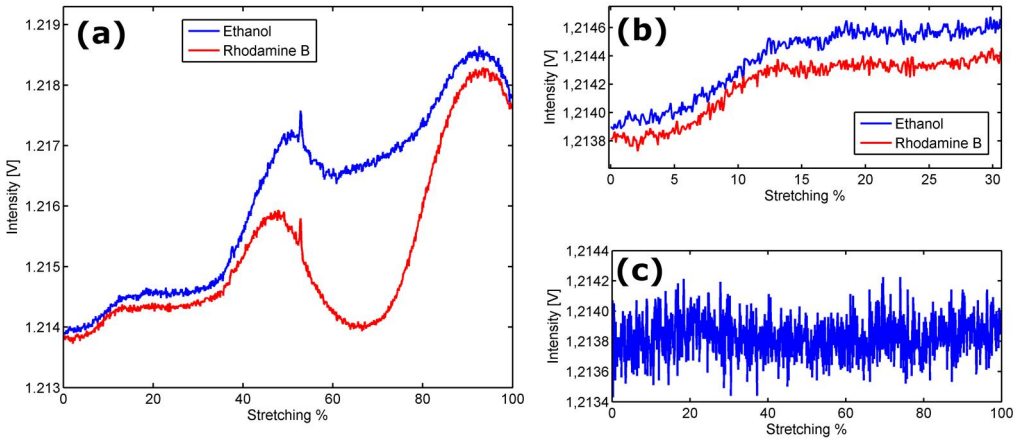

Figure 5.4: (a) Averaged extension and retraction spectra for ethanol (blue line) and rhodamine (red line) before the baseline subtraction, and a magnification of the first stages (b) highlighting the difference between the spectra. (c) The rhodamine baseline characterized by fluctuations of the same order of magnitude of the difference of spectra.

value of the baseline is subtracted. The uncertainty on the absorption peak region is much lower due to the larger difference between the ethanol and rhodamine spectra, at least one order of magnitude larger than the baseline fluctuations (signal-to-noise ratio of approximately 10). The same considerations can be applied to the retraction spectra.

In conclusion we have built an extremely cheap and simple spectrometer based upon the novel technology of SCBI stretchable gratings, capable of spanning the entire visible range of wavelengths without any moving component except the grating stretcher, and maintaining its optical performances for thousands of strain cycles. These results suggest the possibility to develop a novel class of cheap spectrometers, proper for all the applications where the resolution is not extremely demanding. The analysis of the obtained results suggests the directions toward the improvement of the system. The optimization of the optical setup, the molding of gratings characterized by straight grooves and their better clamping on the stretcher can lead to an improvement of the attainable spectra resolution. The uncertainties can be minimized, and thus the intensity precision enhanced, simply by acting on the noise filter and signal amplification stages of the electronics controlling the photodiode.

Part III

Plasmonics

CHAPTER 6

Surface Plasmon Resonance (SPR)

In the previous chapters peculiar behaviors of the optical properties were observed, in particular regarding the non-monotone trend of reflectivity with the amount of nanoparticles supersonically implanted in the Ag/PDMS nanocomposite used for the fabrication of elastomeric mirrors or diffraction gratings. The interaction between the metal and the oscillating external electromagnetic field affects the optical response of metallic materials [141]. The effect of this interaction is enhanced for metal particles with nanometric size [100], as in the case of metal-polymer nanocomposites used for the fabrication of elastomeric optical devices, and can be responsible for the behavior observed in reflectance spectra. Electromagnetic radiation impinging on the nanocomposite excites the free electrons of the metal, that begin to oscillate [142]. If the frequency of the incident light matches the characteristic frequency of the electrons-positive core interaction, a propagating resonant effect called *plasmonic resonance* arises [143].

The *surface-to-volume ratio* of small metallic nanoparticles is much larger than of bulk materials and the electronic states modify accordingly, with the arising of electronic *surface states*. As a result the free electrons are excited at different (usually higher) frequencies. This phenomenon is called *Surface Plasmon Resonance* (SPR) [100] or *Localized Surface Plasmon Resonance* (LSPR) if the size of the nanoparticle is much lower than the wavelength of the plasmonic wave, thus remaining localized on the particle, as depicted in Figure6.1. Surface Plasmon Resonance phenomena can be clearly measured by means of light extinction spectra in the visible range since resonances typically involve a large absorption of energy and thus light intensity.

Plasmons provide the basis for color-changing biosensors [144, 145], photothermal cancer treatments [146, 147], improved photovoltaic cells efficiency [148, 149, 150] and nanoscale photonics circuitry [151, 152]. In these applicative fields the strong enhancement of the electric field caused by the excitation of the plasmon resonance is exploited.

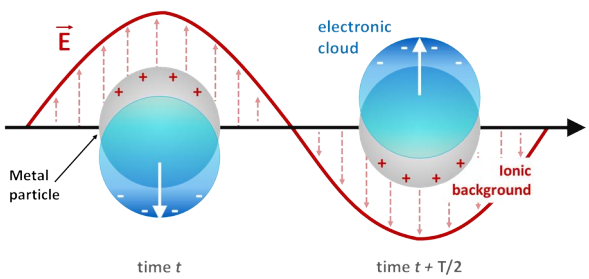

Figure 6.1: Picture of the free electrons-light interaction casing the surface plasmon resonance for metal nanoparticles.

Surface-enhanced Raman spectroscopy (SERS) is a surface-sensitive technique enhancing Raman scattering by molecules adsorbed on a surface properly functionalized in order to present a plasmon resonance [153]. When the incident light in the experiment strikes the surface, localized plasmon is excited and the strong electric field generated in turn excites the molecules adsorbed on the surface. If the shift is small, the Raman signal of the molecules excites again the plasmon resonance and a strong signal is emitted by the surface. Thus the signal is amplified by a factor E^4, allowing the detection of single molecules [154]. This is particularly convenient in the *biosensing* applicative field [144, 155, 156]. Gas sensing represents another interesting application of surface plasmon resonance [157, 158, 159, 160].

The strong electric field generated by the resonance can also be exploited in *photonic circuits* [151] for the amplification of the emission of a gaining medium surrounding the excited metal nanoparticle. Such systems represent a *surface plasmon amplification by stimulated emission of radiation* (SPASER), that is the smallest laser source to date [161, 162]. Nano-light sources in plasmonic circuits can be coupled with plasmonic waveguides and photodiodes or nanoantennas [163, 164, 165].

In order to finely tune the properties of functional plasmonic substrates for the cited applications and to extract information on the metal-polymer nanocomposite system, used in this thesis work, from optical characterization, a physical modeling of the resonances is necessary. In this chapter an overview of the main models describing surface plasmon resonance is given.

6.1 Theoretical models

Surface plasmon resonance causes the appearance of strong peaks in the light absorption spectrum $A(\omega)$ of the sample. Light absorption in a medium is related to the absorption coefficient $\alpha(\omega)$ and the thickness ℓ of the medium by means of the *Lambert-Beer law*:

$$A(\omega) = \alpha(\omega)\ell = N\sigma(\omega)\ell \tag{6.1}$$

Where N is the number of absorber (in our case the number of particles) and $\sigma(\omega)$ the extinction cross section, accounting for the plasmon resonances. The physical parameter controlling the behavior of the extinction cross section is the global *dielectric function* ε of the absorbing mean [100], that must therefore be calculated in order to foresee or understand the optical response of the material.

6.1.1 Drude model

Considering the free electrons like a classic gas moving freely and interacting with a background of positive ions much heavier than electrons, and thus considered fixed, represents the simplest approach for the calculation of the dielectric function of a metallic material. Three main assumption are introduced:

1. **Free electrons approximation**: The interaction between free electrons and the positive ions background is negligible. The only role of positive ions consists in maintaining the overall electrical neutrality of the material.

2. **Independent electrons approximation**: Interaction between electrons is neglected.

3. **Relaxation time approximation**: Collisions between electrons do not depend on the result of previous collisions.

These strong assumptions are however satisfied by materials with complete internal electronic states and with a single electron in the outer shell contributing to conduction (that can be considered free). Alkali metals (Na, K, Rb, Cs) perfectly represent this class of materials. This theory can also be exploited for noble metals, introducing proper corrections accounting for intraband transitions.

The behavior of free electrons subjected to an external electrical field $\vec{E}(t)$ is described by the following equation of motion [143]:

$$m_e \frac{d^2\vec{x}(t)}{dt^2} + m_e\gamma\frac{d\vec{x}(t)}{dt} + e\vec{E}(t) = 0 \tag{6.2}$$

where m_e is the electrons mass and $\gamma = \frac{1}{\tau}$ represents the damping parameter, accounting for electrons collisions, and proportional to the inverse of the electron relaxation time τ. The latter is the time between two subsequent collisions involving the considered electrons. The electric field $\vec{E}(t)$ of an electromagnetic radiation oscillates at a given frequency ω and can therefore be written as $\vec{E}(t) = \vec{E_0} \cdot \exp(-i\omega t)$. If the mean free path l of the electrons is much smaller than the wavelength $\lambda = \frac{2\pi c}{\omega}$ of the electromagnetic radiation ($l \ll \lambda$), the electric field felt by electrons can be considered constant and the *quasi-static approximation* condition is satisfied.

If an oscillating electric field is considered, a particular solution of the equation of motion is given by $\vec{x}(t) = \vec{x_0}(t) \cdot \exp(-i\omega t)$. Substituting this particular solution in equation 6.2, one obtains:

$$\vec{x}(t) = \frac{e}{m_e\left(\omega^2 + i\gamma\omega\right)}\vec{E}(t) \tag{6.3}$$

$$x_0 = \frac{e}{m_e\left(\omega^2 + i\gamma\omega\right)}E_0 \tag{6.4}$$

From classic electrostatics, the electrical displacement $\vec{D}$, the electric field $\vec{E}$ and the macroscopic polarization $\vec{P} = -ne\vec{x}$ induced by the collective motion of the electronic cloud, are bonded by the following relationship:

$$\vec{D} = \varepsilon_0\vec{E} + \vec{P} = \varepsilon_0\varepsilon\vec{D} \tag{6.5}$$

Gathering equations 6.5 and 6.3, the following result can be easily obtained:

$$\vec{D} = \varepsilon_0\left(1 - \frac{\omega_p^2}{\omega^2 + i\gamma\omega}\right)\vec{E} = \varepsilon_0\varepsilon(\omega)\vec{E} \tag{6.6}$$

where ω_p is called *plasma frequency*, the frequency at which the electromagnetic field is resonant with the electrons oscillation and the absorption peak in spectra arises:

$$\omega_p = \sqrt{\frac{ne^2}{\varepsilon_0 m_e}} \tag{6.7}$$

with n the free electrons density per unit volume. This plasma frequency depends on the density of free electrons in the conduction band and is therefore different for each material. The quantity in brackets in 6.6 coincides with the complex *dielectric function* of the material:

$$\varepsilon(\omega) = 1 - \frac{\omega_p^2}{\omega^2 + i\gamma\omega} = \left(1 - \frac{\omega_p^2}{\omega^2 + \gamma^2}\right) + i\left(\frac{\omega_p^2\gamma}{\omega\left(\omega^2 + \gamma^2\right)}\right) \tag{6.8}$$

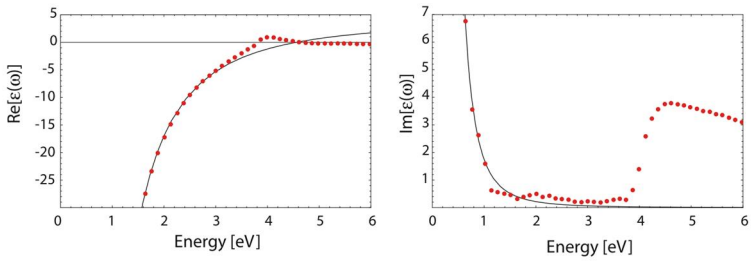

Figure 6.2: The real and imaginary parts of $\varepsilon(\omega)$ for silver determined by Johnson and Christy [167] (red dots) and a Drude model fit to the data [166].

This result well describes the behavior of metals in which electrons can be considered as ideally free. The behavior of noble metals (Ag among them) differ substantially from the theoretical expectations. These differences can be ascribed mainly to two effects: the contribution of the positive ions background to polarization and the interband transitions occurring at high frequencies. Moreover, corrections must be introduced in order to consider the finite size of metal particles.

Core polarization

Free electron approximation is no longer valid for noble metals since the partially filled d band close to the Fermi energy surface causes a highly polarized environment, affecting the motion of the electrons in the conduction band [166]. From Figure6.2 a significative difference of the experimental dielectric function $\varepsilon(\omega)$ respect to the expected theoretical values calculated with the Drude model at high frequencies (higher than 3eV) is clear. The effect of the polarized environment caused by the partially filled d band can be accounted by adding a term ε_{core} to the macroscopic polarization vector:

$$\vec{P}_{core} = \varepsilon_0 \left(\varepsilon_{core} - 1\right) \vec{E} \tag{6.9}$$

thus obtaining the following dielectric function:

$$\varepsilon(\omega) = \varepsilon_{core} - \frac{\omega_p^2}{\omega^2 + i\gamma\omega} \tag{6.10}$$

ε_{core} is usually determined by comparing experimental data of the real and imaginary parts of the dielectric function $\varepsilon(\omega)$ with theoretical models, and it takes values in the range $1 \leq \varepsilon_{core} \leq 12$.

Interband transitions

$\varepsilon(\omega)$ in free electrons metals is governed mainly by electronic transitions within the conduction band or *interband transitions* from inner to conduction band or between the conduction band and higher unoccupied states. In particular noble metals represent monovalent metals in which both the types of transition take place and depend on the electronic structure of noble metals. Metallic materials like, for example, Cu, Ag, or Au, have completely filled $3d$, $4d$ and $5d$ shells and just one electron in the $4s$, $5s$ and $6s$ bands respectively. The interband transitions occur within the broad conduction band (derived mainly from Ag $5s^1p$ hybridized atomic orbitals), which onset at zero frequency [168].

Interband transitions in noble metals can be accounted by introducing an additional complex term to susceptibility $\chi^{IB} = \chi_1^{IB} + i\chi_2^{IB}$ (and as a consequence to the dielectric function, since $\chi = \varepsilon - 1$). This term can be calculated by considering the transition matrix element $\langle f|M|i\rangle$ between the initial and final states of the electron. From the semiclassical model of Parravicini [169], the imaginary part of complex dielectric susceptibility of the interband transitions satisfies the following relation:

$$\omega^2\chi_2^{IB}(\omega) \propto \frac{2}{(2\pi)^3}\sum_{i,f}|\langle f|e\vec{r}|i\rangle|^2\int_{BZ} d^3\vec{k}\delta\left[E_f\left(\vec{k}\right) - E_i\left(\vec{k}\right) - \hbar\omega\right] \tag{6.11}$$

$\langle f\,|e\vec{r}|\,i\rangle$ is the matrix element of the dipole operator between the initial and final states of the electron, with energies E_i and E_f respectively. The integration is done with respect to the components of the wave vector $\vec{k}$ in the Brillouin zone. The real part of the dielectric susceptibility for interband transitions can be obtained by using the Kramers-Krönig transformations. The effects of the interband transitions on the dielectric functions can be accounted in the ε_{bulk} term, including the previously introduced for the effect of the positive ions background, and obtainable by the comparison between the theoretical expectations and experimental values [170].

Finite size effect

The model seen in this section is relative to an infinitely extended metallic material, or with dimensions much larger than the free mean path of the free electrons, of the order to few tens of nanometers. This assumption is no longer valid if nanometric-size particles are considered, as in the case of the silver nanoparticles used in this work.

The relaxation damping term γ appearing in the fundamental equation 6.8 concerns the limitations of the electron mean free path due to collisions between the electrons and of electrons with phonons o impurities of the material. In general the damping effect can be written as:

$$\gamma \to \gamma_\infty = \frac{v_F}{l_\infty} \tag{6.12}$$

where v_F is the Fermi velocity and l_∞ the mean free path of electrons in the bulk metal (approximately 52nm in the case of bulk silver [171]). If we have small particles, with a size $R \ll l_\infty$ the electrons mean free path is limited by the dimension of the particles [172, 173] and an *effective mean free path* $l_R < l_\infty$ must be introduced. In general l_R is proportional to the nanoparticle size R [100, 166, 168] and thus we can write:

$$\gamma(R) = \gamma_\infty + \Delta\gamma(R) \qquad \text{with} \qquad \Delta\gamma(R) = A\frac{v_F}{R} \tag{6.13}$$

Here A is a proportionality coefficient accounting for the aspect ratio, the electrons scattering isotropicity (for spherical particles is unitary) [168] and scattering from the particle surface [174]. This term can be added to the dielectric function 6.8, obtaining the following result:

$$\varepsilon(\omega, R) = \varepsilon_{bulk}(\omega) + \omega_p^2\left(\frac{1}{\omega^2+\gamma_\infty^2} - \frac{1}{\omega^2+\gamma(R)^2}\right) + i\frac{\omega_p^2}{\omega}\left(\frac{\gamma(R)}{\omega^2+\gamma(R)^2} - \frac{\gamma_\infty^2}{\omega^2+\gamma_\infty^2}\right) \tag{6.14}$$

$\varepsilon_{bulk}(\omega)$, whose values can be found in [167, 175], considers both the interband transitions and the core polarization effect

6.1.2 Mie theory

The Drude model can be exploited in the framework of the Mie electrodynamical theory describing the optical response of non-interacting metal spheres irradiated by an external electromagnetic field [176]. Maxwell equations are solved with proper boundary conditions in spherical coordinates and exploiting the multipoles expansion of the potential generating the external field [100]. Another assumption of Mie's theory consists in considering both the particles and the surrounding medium as homogeneous and describable by their bulk optical dielectric functions [177, 178].

Since we deal with nanoparticles with a size of some nanometers (see section 3.2.1 for a silver nanoparticles size distribution characterization), the condition $R << \lambda$ is satisfied and the *quasi-static approximation* can be applied. Only the first term of the multipole expansion, due to dipole excitation, is considered. Out of the approximation higher orders of the multipole expansion must be considered, introducing retardation effects affecting the optical response of the system, in particular the plasmonic absorption peak.

Radiation-matter interaction can be modeled considering two main mechanisms: light *absorption* with generation of heat, and light *scattering*. The sum of absorption and scattering is equivalent to *extinction*. The two different interaction mechanisms are described in terms of the interaction *cross-sections*, related to the radiation intensity loss $\Delta I(z)$ through the Lambert-Beer law:

$$\Delta I_{abs}(z) = I_0 \left(1 - e^{-n_c \sigma_{abs} z}\right) \tag{6.15}$$

$$\Delta I_{sca}(z) = I_0 \left(1 - e^{-n_c \sigma_{sca} z}\right) \tag{6.16}$$

$$\sigma_{ext} = \sigma_{abs} + \sigma_{sca} \tag{6.17}$$

where n_c is the nanoparticles density and σ_{abs}, σ_{sca} and σ_{ext} the absorption, scattering and extinction cross-sections respectively. In the framework of the Mie's theory, the cross-sections can be expressed as follows [166]:

$$\sigma_{ext} = \frac{2}{x^2} \sum_{L=1}^{\infty} (2L+1) \left[\Re(a_L + b_L)\right] \tag{6.18}$$

$$\sigma_{sca} = \frac{2}{x^2} \sum_{L=1}^{\infty} (2L+1) \left[\Re\left(|a_L|^2 + |b_L|^2\right)\right] \tag{6.19}$$

x depends on the particle size R and on the refractive index of the surrounding medium n_m:

$$x = \frac{2\pi R n_m}{\omega} \tag{6.20}$$

a_L and b_L are the scattering coefficients and can be expressed in terms of the Ricatti-Bessel functions $\psi_L(x)$ and $\xi_L(x)$:

$$a_L = \frac{m\psi_L(mx)\psi_{L'}(x) - \psi_L(x)\psi_{L'}(mx)}{m\psi_L(mx)\xi_{L'}(x) - \xi_L(x)\psi_{L'}(mx)} \tag{6.21}$$

$$b_L = \frac{\psi_L(mx)\psi_{L'}(x) - m\psi_L(x)\psi_{L'}(mx)}{\psi_L(mx)\xi_{L'}(x) - m\xi_L(x)\psi_{L'}(mx)} \tag{6.22}$$

and $m = \frac{n}{n_m}$ the ratio between the refractive indexes of the particle and of surrounding medium. The subscript L indicates the order of the spherical multipole excitation: $L = 1$ refers to dipole oscillation, $L = 2$ to quadrupole oscillation and so on. In quasi-static approximation only the first term (i.e. the dipole approximation) is considered and thus it follows [166]:

$$\sigma_{sca} = \frac{8\pi}{3} \left|\vec{k}\right| R^6 \left|\frac{\varepsilon - \varepsilon_m}{\varepsilon + 2\varepsilon_m}\right|^2 \qquad \sigma_{abs} = 4\pi \left|\vec{k}\right| R^3 \Im\left(\frac{\varepsilon - \varepsilon_m}{\varepsilon + 2\varepsilon_m}\right) \tag{6.23}$$

Where ε and ε_m are the dielectric functions of the nanoparticle and of the surrounding medium respetively, and $|\vec{k}| = 2\pi\frac{\sqrt{\varepsilon_m}}{\lambda}$ the wave vector of the incident light. From the different dependence of the two cross-sections from the particle size R it is clear that for extremely small particles (i.e. nanoparticles) the scattering cross-section can be neglected and thus the only contribution to extinction is due to absorption, $\sigma_{ext} \simeq \sigma_{abs}$. Hence for small particles in dipole approximation and considering the complex dielectric function $\varepsilon = \varepsilon_1 + i\varepsilon_2$:

$$\sigma_{ext} = \sigma_{abs} = 9\frac{\omega}{c}\varepsilon^{\frac{3}{2}} V_0 \frac{\varepsilon_2}{\left[\varepsilon_1 + 2\varepsilon_m\right]^2 + \varepsilon_2^2} \tag{6.24}$$

where $V_0 = \frac{4}{3}\pi R^3$ is the volume of the particle. From equation 6.24, the extinction cross-section is characterized by a resonance in the case $\varepsilon_1(\omega) = -2\varepsilon_m$ and does not directly depend on the cluster size R but only indirectly through the size dependance of the dielectric function $\varepsilon(\omega, R)$, as discussed in the previous section and shown in equation 6.14.

If $\omega \gg \gamma$, the damping term can be neglected, and substituting equation 6.8 in 6.24, a lorentzian curve, typical of absorption peaks, is obtained:

$$\sigma_{abs} = \sigma_0 \frac{1}{\left(\omega - \omega_{Mie}\right)^2 + \left(\frac{\gamma}{2}\right)^2} \tag{6.25}$$

where ω_{Mie} is the Mie's resonance frequency than, in dipole approximation, can be expressed as:

$$\omega_{Mie} = \frac{\omega_p}{\sqrt{1 + 2\varepsilon_m}} \tag{6.26}$$

If the polarization of the positive ion background is considered [100]:

$$\omega_{Mie} = \frac{\omega_p}{\sqrt{\varepsilon_{core} + 2\varepsilon_m}} \tag{6.27}$$

Mie's theory well describes the optical behavior of non-interacting metal nanoparticles but is an electrodynamical model, giving no insight in the physics of the system. For example, it does not take into account the effects due to the matrix and the polydispersion of the particles size [168]. More important, in metal-polymer nanocomposites synthesized by SCBI, metal nanoparticles are not well isolated as can be seen in Figure3.9, but their concentration depends on the implanted dose [22]. Hence metal nanoparticles feel the electrical field generated by the other particles and the non-interacting particles assumption is no longer valid. Nanoparticles implanted in the polymer in high concentrations aggregate, leading to the formation of metal nanostructures with different topologies and not uniformly distributed inside the dielectric. As a result, a different model, considering the macroscopic behavior of the nanocomposite system as an *effective medium* instead of single particles, and giving an insight in the physics of the system, is desirable.

6.1.3 Maxwell-Garnett theory

In nanocomposite systems with a high concentration (or *volume fraction*, defined by equation 3.4) of nanoparticles, their reciprocal distance is such that reciprocal interactions can not be neglected anymore [179, 168]. In particular if the distance between the nanoparticles drops below $5R$, a redshift and a broadening of the absorption peaks is observed and enhanced by the formation of cluster aggregates. As an example, an increase of the resonance peak position from 520nm up to 750nm is observed if two gold particles are approached down to a distance of 0.5nm [180]. The Mie's electrodynamical theory fails to describe such a behavior.

Maxwell Garnett theory [181] is an effective medium theory describing the macroscopic behavior of a system from the knowledge of the physical properties of its constituents. This theory is valid only in the quasi static approximation ($2R \ll \lambda$) and for very small interparticles distance. In this context a statistical description of the system, taking into account the distribution of the particles in the dielectric, their reciprocal distance and their aggregation status, is preferable, and the volume fraction f represents the parameter discriminating the different configurations of the system. For $f \ll 1$ clusters are so diluted that the interactions between them can be neglected: in this limit the theory coincides with the Mie's model and the optical response of the whole material is given by the sum of the contributions of each particle treated singularly. For larger values of f it makes no sense to deal with single non interacting particles and neither the dielectric function ε_m is no longer valid to describe the dielectric medium between the clusters.

In the framework of the Maxwell Garnett theory, the dielectric medium between the particles is conceptually replaced with an *effective medium*, with a dielectric function ε_{eff}, accounting for all the electrostatic interactions between neighboring clusters. ε_{eff} can be inferred from the dielectric functions ε characterizing the metal particles and ε_m of the dielectric matrix, and the volume fraction f. Extinction of the system is due to the effective electromagnetic field $E_{Maxwell}$ acting on a given particle and by the individual particle properties (i.e. its polarizability α), but if the concentration of the metallic filler is sufficiently high the field felt at a given particle position is affected by the fields generated by the other particles and by the polarizability of the medium until a certain distance (see Figure6.3). Given a reference particle, the sphere containing all the particles contributing to the optical response of the former is called *Lorentz sphere*. Hence at a given position the local electric field is:

$$E_{local} = E_{Maxwell} + E_s + E_{near} \tag{6.28}$$

where E_s is the field generated by the polarization charges at the Lorentz sphere and E_{near} the electric field generated by neighboring particles. Under quasi-static assumption, E_s can be calculated and is equal to:

$$E_s = \frac{P}{3\varepsilon_0\varepsilon_m} \tag{6.29}$$

with P representing the macroscopic polarizability of the dielectric:

$$P = E_{local} \sum_{j=1} N n_j \alpha_j = \varepsilon_0 \left(\varepsilon_{eff}\varepsilon_m\right) E_{Maxwell} \tag{6.30}$$

n_j is the number density of the j-th particle with polarizability:

$$\alpha_j = \frac{\varepsilon - \varepsilon_m}{\varepsilon + 2\varepsilon_m} R_j^3 \tag{6.31}$$

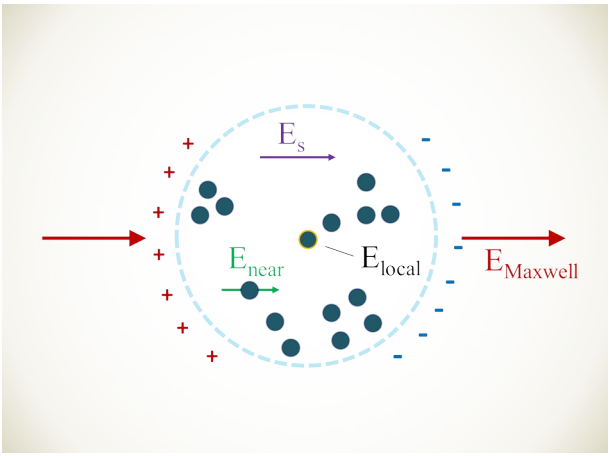

Figure 6.3: The Lorentz sphere concept applied to cluster matter. The signs of the charges correspond to an empty sphere in the dielectric surrounding [100].

Thus, in the quasi-static approximation, the whole system can be considered homogeneous and as an effective medium with a dielectric function $\varepsilon_{eff} = \varepsilon_{1,eff} + i\varepsilon_{2,eff}$ that, combining these last results, is given by:

$$\varepsilon_{eff}(\omega) = \varepsilon_m \frac{1 + \frac{2}{3\varepsilon_0\varepsilon_m}\sum_j n_j\alpha_j}{1 - \frac{1}{3\varepsilon_0\varepsilon_m}\sum_j n_j\alpha_j} \tag{6.32}$$

This effective dielectric function can be rewritten in terms of physical measurable quantities, like the volume fraction, obtaining the Maxwell Garnett formula:

$$\varepsilon_{eff} = \varepsilon_m \frac{1 + 2f\Lambda}{1 - f\Lambda}, \qquad \Lambda = \frac{1}{\varepsilon_m}\frac{\varepsilon - \varepsilon_m}{\varepsilon + 2\varepsilon_m} \tag{6.33}$$

This effective dielectric function reaches a maximum value (i.e. a resonance) if the following condition is satisfied [182]:

$$\varepsilon\left(\omega_{spr}^{MG}\right)(1 - f) + \varepsilon_m(2 + f) = 0 \tag{6.34}$$

Exploiting the equation 6.8 for the dielectric function in the Drude model, the resonant wavelength of the Maxwell Garnett theory can be obtained:

$$\omega_{spr}^{MG}(f) = \frac{\omega_p}{\sqrt{\left(\frac{2+f}{1-f}\right)\varepsilon_m + \varepsilon_{core}}} \tag{6.35}$$

that, for $f \to 0$ coincides with the result obtained in the Mie's theory, while it is clear that the resonance wavelength strongly depend on the filler volume fraction.

In order to better understand and justify the experimental results that will be presented in the next chapter, a study of the effect of the different parameters on the optical response of the system according to this model is necessary. The nanocomposite synthesized by SCBI is characterized by nanoparticles with a given distribution size, as shown in Figure3.8 and thus with different optical responses when irradiated with visible light.

In general absorbance A_{tot} is the sum of all the contributions due to different cluster sizes:

$$A_{tot} = N \sum_i n_i \left(R_i\right) k_{\lambda_i} \left(R_i\right) t \tag{6.36}$$

where N is the number of nanoparticles in the irradiated nanocomposite portion, $n_i(R_i)$ the fraction of nanoparticles with size R_i and absorption coefficient $k_{\lambda_i}(R_i)$, and t the nanocomposite thickness (i.e. the nanoparticles penetration depth). The absorption coefficient can be easily calculated from equation 6.24 [100] and expressed in terms of the wavelength λ for a direct comparison with the measurements:

$$k_\lambda = 18\pi f \varepsilon^{\frac{3}{2}} \frac{\Im\varepsilon_{eff}(\lambda)}{\lambda\left(\left(\Re\varepsilon_{eff}(\lambda) + 2\varepsilon_m\right)^2 + \Im\varepsilon_{eff}(\lambda)^2\right)} \tag{6.37}$$

where the dielectric function in this case is the *effective dielectric function* $\varepsilon(\lambda) = \varepsilon_{eff}(\lambda)$ obtainable from equation 6.33. In the effective dielectric function, the dielectric function of the metal nanoparticle (in this case silver) is obtained by equation 6.8 re-expressed in terms of the light wavelength:

$$\varepsilon(\lambda) = \varepsilon_{bulk}(\lambda) - \frac{2\pi c\tau\lambda^2}{\lambda_p^2\left(2\pi c\tau + i\lambda\right)} \tag{6.38}$$

It is worth noting that the absorption coefficient k_λ in equation 6.37 does not depend on the particle size, thus, according to the Maxwell Garnett theory, R does not affect neither the position nor the shape of the plasmonic absorption peak in an absorption spectrum.

The parameters needed for the plot of the theoretical spectra are obtained from literature or from direct measurements part of this work. A silver nanoparticle - PDMS nanocomposite is considered, simulating the system studied in this work and shown in section in the TEM image in Figure3.9. PDMS is a highly transparent elastomer and thus the imaginary part of the dielectric constant ε_m is negligible. From the PDMS datasheet [183], the (real) dielectric constant is $\varepsilon_m = 2.7$. The plasma resonance peak for bulk silver is calculated with equation 6.7 and turns out to be $\lambda_p = 136nm$ [184], and the relaxation time $\tau = 8.6fs$ obtained from [185]. The bulk silver dielectric function was extracted from an interpolation of data taken from Palik [175] in the range between $350nm$ and $900nm$. The real and imaginary parts of ε_{bulk} are reported in Figure6.4.

In Figure6.5 the simulated curves of the plasmon peak according to Maxwell Garnett theory are reported for different values of volume fraction f. The curves are obtained simply by using the absorption coefficient 6.37, since it does not depend on the cluster size. By increasing the volume fraction a redshift of the resonance frequency is observed, together with a sharpening and intensity increase of the peak. The trend of the resonance frequency as a function of the volume fraction is reported in the inset of Figure6.5: data from [175] were fitted with a quadratic polynomial, obtaining the equation $\lambda_{spr} = 277.76f^2 - 45.63f + 397.73$. The discontinuities of data in this graph are due to the interpolation procedure of the bulk dielectric function.

6.1.4 Shell-core model

The models seen in the previous sections describe the optical behavior of homomolecular particles, i.e. the behavior of particles constituted by just one element (in this case, silver). However it is well known that silver is subject to oxidation [186] even if implanted in an elastomeric matrix, since PDMS is permeable to air [187]. In ambient atmosphere

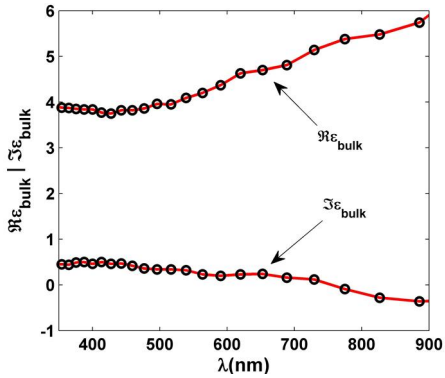

Figure 6.4: Plot of the interpolated data (taken from [175] for the bulk dielectric function ε_{bulk} relative to silver. Black circles represents experimental data, interpolated with the red line.

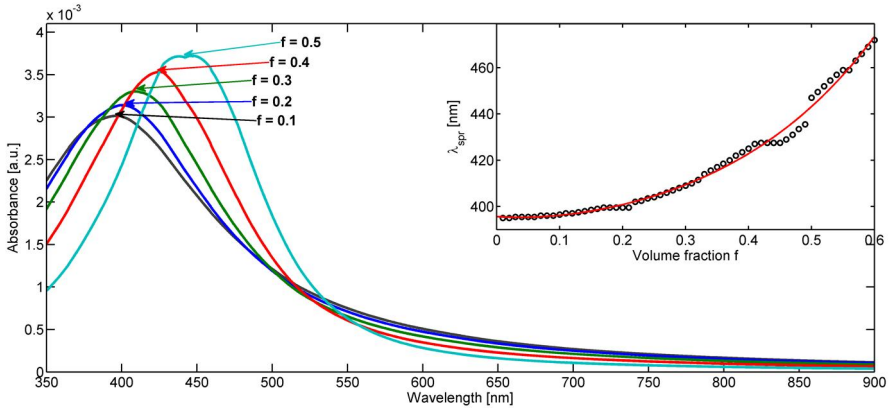

Figure 6.5: Simulation results of the plasmon peak calculated according to Maxwell Garnett theory (equation 6.37) for different values of the volume fraction f. The inset shows the trend of the resonance frequency as a function of the volume fraction (black circles), fitted with a second-order polynomial (red line).

silver particles oxidize on the surface only [188, 189] according to the following reaction [186]:

$$4Ag + O_2 \rightarrow 2Ag_2O \tag{6.39}$$

and oxide layer creates a passivation film protecting the bulk against oxidation. This reaction gives rise to the formation of eteromolecular clusters with a pure silver core and a silver oxide shell growing on the surface with a lower density ($7.14g/cm^3$) compared to pure silver ($10.49g/cm^3$) and thus increasing the total size of the nanoparticle. For such systems classical Mie's or Maxwell Garnett theories are not sufficient and a *shell-core* model must be used [190]. Silver nanoparticles oxidation affects the cluster polarizability α: if R_s, R_c represent the radius of the particle (core + shell) and of the silver core respectively, with dielectric functions ε_s and ε_c, then it follows from [190]:

$$\alpha = 3V_0\varepsilon_m \frac{\left(\frac{R_s}{R_c}\right)^3 (2\varepsilon_s + \varepsilon_c)(\varepsilon_s - \varepsilon_m) - (\varepsilon_s - \varepsilon_c)(2\varepsilon_s + \varepsilon_m)}{\left(\frac{R_s}{R_c}\right)^3 (2\varepsilon_s + \varepsilon_c)(\varepsilon_s + 2\varepsilon_m) - (\varepsilon_s - \varepsilon_c)(\varepsilon_s - \varepsilon_m)} \tag{6.40}$$

This polarizability must be used in the following absorption cross-section in order to describe the plasmon resonance peak of the shell-core particle:

$$\sigma_{abs} = \frac{2\pi}{\lambda\sqrt{\varepsilon_m}} \Im\alpha \tag{6.41}$$

This model was exploited in [191] for the modeling of the behavior of silver nanoparticles dispersed in polystyrene and oxidized with thermal annealing treatments. In [191] the oxidation of the silver nanoparticles gives rise to a two-peaks structure in the absorption spectrum: a first peak at a wavelength around $400nm$ due to pure silver particles, and a second contribution at higher wavelengths, convoluted with the first, due to the oxidized particles and describable with the shell-core model. The contribution of oxidized silver particles redshifts with the increase of the annealing temperature and the consequent thicker oxide shell: this behavior was studied extensively in [192] by FTDT simulations. The redshift of the oxidized particles peak is explained in terms of the decrease of interparticle distance caused by the increase of the oxide shell, also increasing the total volume of the cluster because of the lower density respect to pure silver, as shown in Figure6.6a. By exploiting equations 6.41 and 6.40, absorption spectra were simulated for different $\frac{R_s}{R_c}$ ratios in order to better explain the results shown in the next chapter regarding Ag/PDMS nanocomposites synthesized by SCBI. The same input parameters used in the case of Maxwell Garnett theory were employed in this case too. Additionally, the dielectric function of silver oxide ε_s was taken and interpolated from [175] in the range between $350nm$ and $900nm$ (Figure6.6b), and the cluster radius obtained from the TEM characterization of the size distribution reported in Figure3.8. The results of the simulations, presented in Figure6.6c, show a redshift and intensity decrease of the plasmonic peak with the growth of the silver oxide shell around the particle, compatible with a decrease of the interparticle distance observed, for example, in [182, 180, 193]. The inset of Figure6.6c shows the results for the trend of the plasmonic peak wavelength as a function of the $\frac{R_s}{R_c}$ ratio, fitted with the quadratic polynomial $\lambda_{spr} = -91.97\left(\frac{R_s}{R_c}\right)^2 + 355.37\left(\frac{R_s}{R_c}\right) + 218.15$.

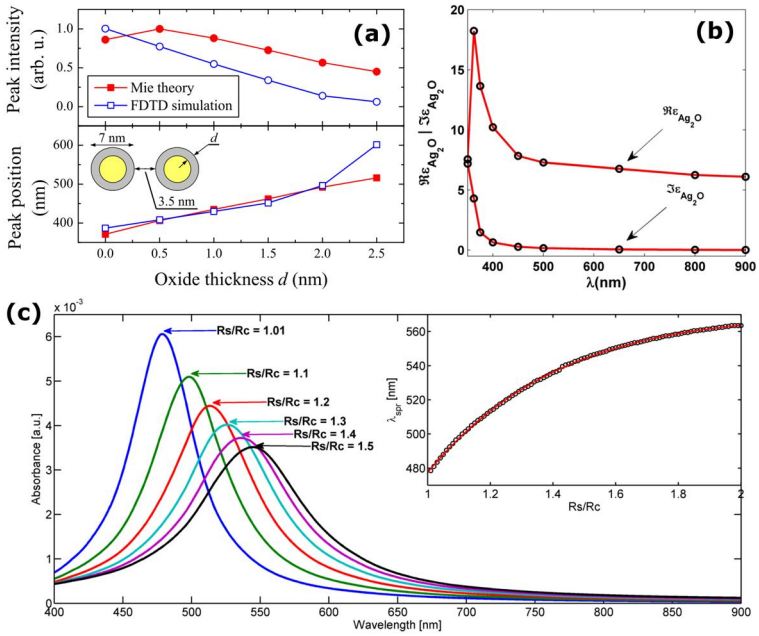

Figure 6.6: (a) Shell-core model with decreasing interparticle distance due to the growth of the silver oxide on the particle surface [192]. (b) Real and imaginary parts of the dielectric function of Silver oxide Ag_2O (black circles) interpolated with the red line. (c) Simulation results of the plasmon peak calculated according to the shell-core model (equation 6.41) for different values of the $\frac{R_s}{R_c}$ ratio. The inset shows the trend of the resonance frequency as a function of the particle/core radius ratio (black circles), fitted with a second-order polynomial (red line).

6.2 Bergman model

In the previous sections we have seen that a dielectric matrix filled with metal nanoparticles at a concentration such that the reciprocal interactions can not be neglected, can be described by introducing an effective dielectric function ε_{eff}. The dielectric function describing the behavior of a matrix filled with metal nanoparticles is obtained starting from the dielectric functions of the constituents of the system, properly combined by *mixing formulas* like equation 6.33 for Maxwell Garnett theory. According to this theory only systems characterized by low concentrations can be considered, such that the reciprocal interactions between the nanoparticles can be neglected. Other theories have been developed for the description of the optical behavior of metal-polymer nanocomposites. In particular the Bruggeman theory overcomes the limits of the Maxwell Garnett theory in terms of validity for volume fractions $f > 0.3$ and of the nanoparticles shape, that is assumed to be spherical. However also the Bruggeman theory suffers of some limitations: some resonances for $\frac{\varepsilon_1}{\varepsilon_2} < 0$ (with ε_1 and ε_2 the dielectric functions of the constituents of the nanocomposite) are not predicted and, more important, the effective dielectric function ε_{eff} can be calculated exactly only for very simple arrangements (or *topologies*) of the two phases inside the composite material [194].

The Bergman representation [194] represents a more general approach for the effective description of two phases composite systems, independently on the nanoparticles size, for arbitrary volume fraction and for each possible system topology or combination

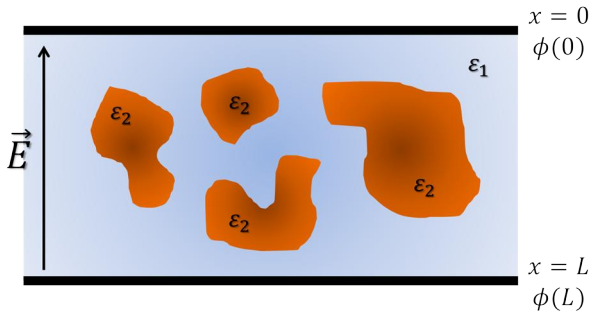

Figure 6.7: Schematic drawing of a parallel plate condenser of thickness L, filled with a composite medium made of arbitrarily shaped homogenous grains with a dielectric function ε_2 embedded in a homogeneous host with a dielectric function ε_1 [194]. $\vec{E}$ is the electric field across the sample generated by the difference of potential $\phi(0) - \phi(L)$.

of topologies. As in the case of the Mie's theory, Maxwell's equations are applied, in the quasi-static approximation, to a system consisting in a metallic filler with dielectric function ε_2 and volume fraction f inside a dielectric matrix with dielectric function ε_1, sandwiched between two electrodes through which an electric field $\vec{E}(\omega)$ is applied (like a capacitor, see Figure6.7). Thus the effective dielectric function ε_{eff} is defined through the expression for the electrostatic energy stored in the composite material:

$$\frac{1}{2}\varepsilon_0\varepsilon_{eff}(\omega)\left\langle\vec{E}(\omega)\right\rangle^2 = \frac{1}{V}\int_V \frac{1}{2}\varepsilon_0\varepsilon(\vec{r},\omega)\vec{E}^2(\vec{r},\omega)d\vec{r} \tag{6.42}$$

where $\varepsilon(\vec{r},\omega)$ represent the dielectric function of the constituent in a given position $\vec{r}$ of the system. This integral can be developed by integrating on the whole volume of the composite material, applying the proper boundary conditions. All the geometrical considerations and topology of the problem are mapped into a characteristic function, the so-called *spectral density* g, while the optical behavior described by the function t. The effective dielectric function ε_{eff} can be written as:

$$\varepsilon_{eff}(\omega) = \varepsilon_1(\omega)\left(1 - f\int_0^1 \frac{g(y)}{t(\omega) - y}dy\right) \tag{6.43}$$

where

$$t = \frac{\varepsilon_1(\omega)}{\varepsilon_1(\omega) - \varepsilon_2(\omega)} \tag{6.44}$$

If t takes real values between 0 and 1 at some frequency, the integrand denominator vanishes and the integral diverges. This situation is called *electrostatic resonance*.

The function g only depends on the system topology and does not have anything to deal with the dielectric properties of the constituents, all contained in the function t. g can be considered as a non-negative distribution function of resonances corresponding to the specific arrangement of the constituents. It is normalized:

$$\int_0^1 g(y)dy = 1 \tag{6.45}$$

and in the case of statistical isotropic samples, the moment rule is:

$$\int_0^1 yg(y)dy = \frac{1-f}{3} \tag{6.46}$$

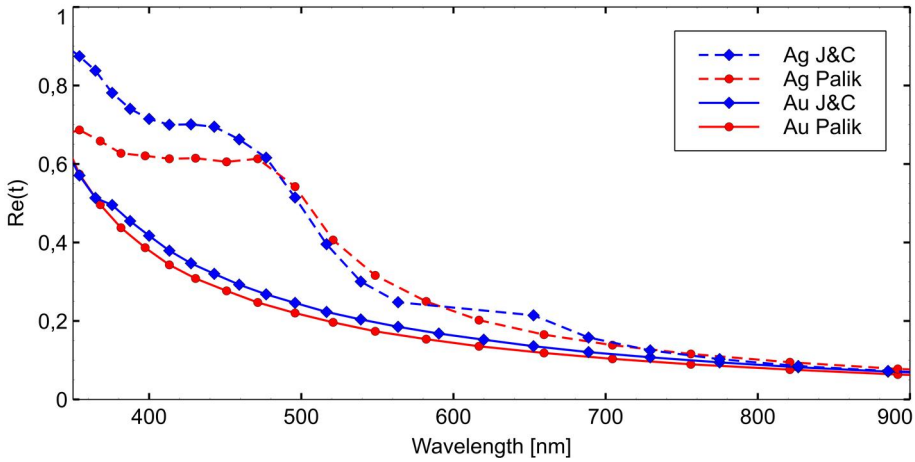

Figure 6.8: Values of the real part of the t function for Silver (solid lines) and Gold (dashed lines) implanted in PDMS ($\varepsilon_m = 2.7$, [183]) calculated with data taken from Johnson and Christy [167] (blue lines) and [175] (red lines).

The spectral density g has a noticeable influence on ε_{eff} if t is sufficiently close to the interval $[0, 1]$ on the real t-axis: in this case g can be obtained from measurements of ε_{eff}. If t is far away from $[0, 1]$, ε_{eff} is not sensitive to the system topology and therefore must be calculated with simple mixing formulas (e.g. Maxwell Garnett or Bruggeman). This condition, also referred as *rigorous bounds on* ε_{eff}, is satisfied for silver or gold nanoparticles implanted in PDMS: Figure6.8 shows the values assumed by the t function in the visible range by using data from different authors [175, 167] for the metals dielectric functions, and remains always in the range $[0, 1]$ between 350nm and 900nm.

Only few approaches have been made to explicitly and exactly calculate the spectral density g for realistic systems, like a dilute suspension of metal spheres [195], because of the Fredholm integral form of the expression for ε_{eff}. In the other cases in which g can not be explicitly calculated, it can be obtained from the measurement of ε_{eff} in an iterative way since, in most cases, slight errors in ε_{eff} may cause enormous numerical errors in g. The spectral density is thus adjusted to measurements using genetic algorithms. First an arbitrary starting function g, satisfying the normalization rules 6.45 and 6.46, is discretized. A random number generator assigns three points of the spectral density to be changed keeping the first two moments conditions satisfied. If the spectral density still is non-negative, the new integrals are calculated from the old ones and the new spectrum is compared with the measures. If the agreement is better than before, the iteration continues with the same variations. If not, different variations are tried. The resulting spectral density is finally smoothed using a momentum-conserving algorithm.

Bergman representation represents a powerful approach for the non-destructive investigation of the arrangement of the nanoparticles inside the polymeric matrix by means of optical measurements, mainly if the nanocomposite is subjected to a mechanical stress. Moreover it is worth noting that the same spectral density g obtained from optical measurements can be used to model other physical properties (always by using the Bergman representation), like the electrical or thermal conductivity. the Bergman representation will not be used for the description of the experimental results obtained and reported in the next chapter, but is a fundamental brick for the development of the future work deriving from the conclusions of this work.

CHAPTER 7

SPR in SCBI metal-polymer nanocomosites

The study of the plasmonic response of the Ag/PDMS nanocomposite synthesized by means of SCBI is driven by the necessity of investigating the optical properties of the material used for the fabrication of elastomeric mirrors or gratings and improve the fabrication process. Different processes are involved in the evolution of the optical response of the Ag/PDMS nanocomposite (PDMS swelling and nanoparticles oxidation, diffusion and aggregation among them) that must be investigated through nanocomposites treated with different processes. Nanoparticles oxidation was catalysed by thermal annealing at different temperatures and different times. The same treatments also enhance nanoparticles diffusion and aggregation in the polymer matrix. The deposition of a second PDMS layer after implantation was tried as a possible solution for the freezing of the nanocomposite state both in terms of oxidation and diffusion/aggregation.

Moreover, since elastomeric optical devices are often used in applications where *deformability* is a requirement, the surface plasmon resonance was also characterized as a function of sample *elongation*. Preliminary results will be presented at the end of this chapter, showing interesting results regarding the nanocomposite internal dynamics. These results also helps in better understanding the cluster topology and the electronic transport properties of such systems.

All the samples have been characterized by the acquisition of absorbance spectra in the uv-visible wavelength range (350-900nm) with a Jasco 7850 spectrophotometer. The sample holder of this instrument was modified by adding a home made computer-controlled motorized linear stage, enabling to measure different samples simultaneously and repeatedly at given time intervals. The temperature of the measurement chamber of the spectrophotometer was approximately $30°C$. A reference spectrum of the bare PDMS was acquired before each measurement and the absorbance nullified at 900nm, far from the resonance peak, before mounting the nanocomposite samples.

7.1 Absorption with different equivalent thicknesses

In section 4.3.1 reflectance spectra of the Ag/PDMS nanocomposites with different implanted equivalent thicknesses were presented, showing an interesting non-monotone trend. Highly filled nanocomposites exhibit a lower reflectance respect to nanocomposites with lower amounts of implanted nanoparticles, at odd with expectations. Reflectance is just one of the three components of the optical response of a material, together with transmittance and absorbance. The sum of these three quantities is unitary, therefore reflectance can be attenuated by absorbance or transmittance. Of the two, transmittance decreases with the amount of nanoparticles implanted in the polymer, because of the well-known Lambert-Beer's law. Absorbance thus remains the only possible

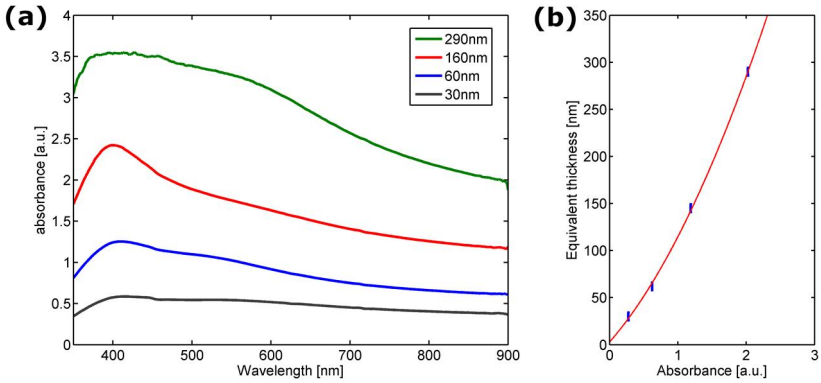

Figure 7.1: (a) Absorbance spectra of nanocomposites with different implanted equivalent thicknesses (b) Plot of the *baseline* absorbance for different equivalent thicknesses. The baseline was calculated as the mean absorbance far from the resonance peak, in the wavelength interval 850-900nm.

explanation for the reflectance behavior of metal-polymer nanocomposites with increasing implanted equivalent thicknesses.

Absorption spectra of samples implanted with different equivalent thicknesses (290, 120, 60, 30nm, named c5, c6, c7 and c8 respectively) were acquired by uv-vis spectroscopy and the results shown in Figure7.1a. By increasing the equivalent thickness an enhancement of the absorbance is observed, as expected. However the whole spectrum is shifted toward larger values of absorbance, at odd with the expectations of the Maxwell-Garnett model, in which the *baseline* (the region of spectrum far from the resonance, typically in the near-infrared in the current case) is expected to be null. The high baseline of the reported spectra can be explained with the aggregation of a fraction of the metal nanoparticles inside the polymer, forming a buried *bulk metal layer* with a plasmon resonance shifted to the infrared region and causing a uniform absorbance in the whole wavelength visible range considered for the measurements. This simple model, already presented in [118] in order to conciliate optical and electrical measurements, is schematically reported in Figure7.2. An increase of the implanted equivalent thickness leads to the growth both in density and thickness of this bulk layer, enhancing the absorbance throughout the entire spectrum, as observed in Figure7.1. Additionally, as already seen in section 3.4.4 and in [22], a *swelling* of the PDMS is observed upon implantation. This phenomenon *drags* the non-aggregated metal nanoparticles far away from the bulk layer, giving rise to the formation of a polymer layer with dispersed nanoparticles above the bulk layer, responsible for the presence of the surface plasmon resonance.

Baseline levels were measured by averaging the infrared tails of spectra (in the region between 850nm and 900nm), far from the resonance peaks. The results of this analysis for the different values of equivalent thickness are reported in Figure7.1b. The increase of absorbance with the amount of implanted nanoparticles justifies the non-monotone behavior of the reflectance observed in Figure4.1b: the larger number of nanoparticles in the polymer and the subsequent formation of thicker nanostructured bulk layers cause an enhancement of absorbance, negatively affecting the reflectance of the material. On the opposite, reflectance of nanocomposites implanted with a low equivalent thickness is limited by the low number of metal nanoparticles. The trade-off between high values

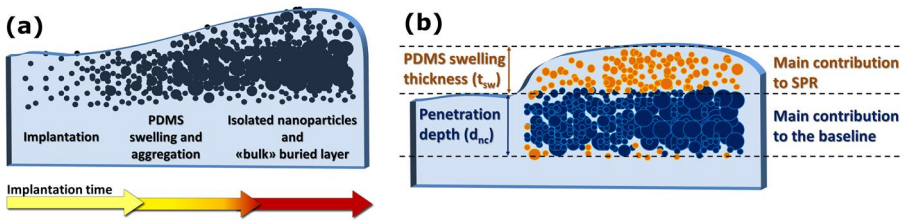

Figure 7.2: (a) Schematic picture of the evolution of the metal-polymer nanocomposite with increasing implantation time and thus equivalent thickness, with the formation of a buried bulk layer. (b) Final configuration of the metal-polymer nanocomposite after implantation and polymer swelling: The upper region with dispersed nanoparticles is responsible for the surface plasmon resonance peak in the absorption spectrum, while the buried *bulk* layer affects the level of the baseline. (From [118]).

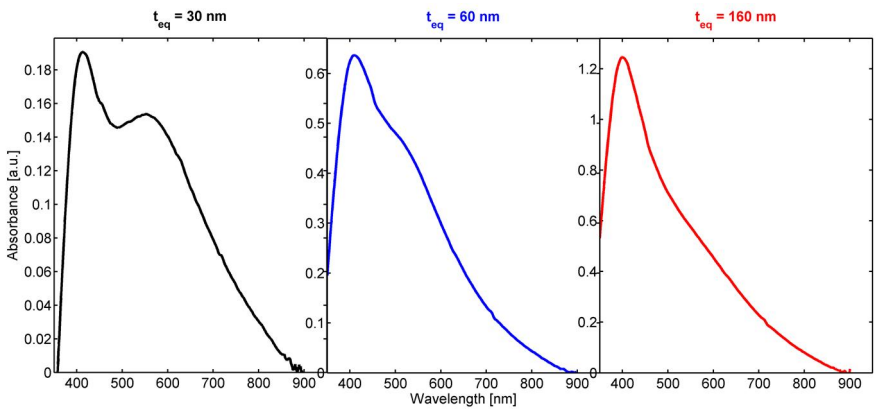

Figure 7.3: Absorbance spectra of samples c6, c7 and c8 with the subtracted baseline and with different vertical scales for a direct comparison of the shape of the surface plasmon resonance peaks.

of reflectance and limited absorbance is achieved for an equivalent thickness of approximately 60nm, as already discussed in section 4.3.1.

In order to analyze the dynamics of the isolated nanoparticles in the upper region of the nanocomposite, the baseline was subtracted from the spectra of the samples c6, c7 and c8, and the results presented in Figure7.3. Sample c5 was not considered because of the high absorbance (near to the instrumental dynamic range) that avoids to obtain a smooth resonance peak from which useful and reliable information can be extracted. By subtracting the baseline, the contribution of the surface plasmon resonance is highlighted and exhibits a double-peak structure, mainly for nanocomposites implanted with lower equivalent thicknesses. The *first peak*, at approximately 400nm, is due to the surface plasmon resonance of pure silver nanoparticles and its shape can be well compared with the Maxwell-Garnett simulated spectra (Figure6.5). The *second peak*, positioned between 500nm and 600nm, is supposed to be caused by the surface plasmon resonance of oxidized silver nanoparticles, describable with the shell-core model introduced in section 6.1.4 (Figure6.6).

The first peak, due to the pure silver nanoparticles, undergoes a blueshift with in-

creasing implanted equivalent thickness, at odd with the Maxwell Garnett model and the expected increase of the volume fraction. Similar results were observed and deeply studied in Au/PDMS nanocomposites [21]. Blueshift can be explained with the decrease of the filler volume fraction caused by aggregation of nanoparticles to the bulk layer and to the increase of the nanocomposite total volume following the swelling of the polymer, enhanced by larger implanted equivalent thicknesses (as observed and explained in [22]).

More interesting, the behavior of the second peak due to the oxidized silver nanoparticles. Its relative intensity respect to the intensity of the first peak is lower and shifts toward longer wavelengths for larger implanted doses. According to the shell-core model introduced in section 6.1.4 this trend is compatible with thicker oxide shell around the silver nanoparticles in the case of low implanted nanocomposite respect to high implanted doses. As already stated in section 6.1.4, PDMS is permeable to oxygen and thus, in the case of a low equivalent thickness, the few implanted nanoparticles are all exposed to oxygen and they therefore undergo oxidation. If a larger amount of filler is implanted, nanoparticles near the surface of the nanocomposite *shield* the underlying particles, thus limiting their oxidation.

7.2 Time evolution of the nanocomposite at RT

Silver nanoparticles oxidation gives rise to a second resonance peak in the absorption spectrum of the Ag/PDMS nanocomposite, also affecting the reflectance of the material. It is thus necessary to investigate and control the time evolution of the surface plasmon resonances, both at room temperature and after thermal annealing processes, in order to improve the fabrication process of the elastomeric optical devices. Only nanocomposites implanted with an equivalent thickness of 60nm were characterized.

Absorbance spectra of similar samples were acquired every 30 minutes up to 456 hours after implantation. The samples were kept in standard conditions, at room temperature, between the measurements. Since all the samples show the same behavior, in Figure7.4a only the results relative to one sample is shown after certain significative times after implantation. The baseline was subtracted from spectra in order to directly compare the shape of the resonance peaks with the theoretical models. The time evolution of the intensity relative to the pure silver peak and to the baseline (calculated as the average of the spectrum between 850nm and 900nm) are reported in Figure7.4b, while the position of the pure silver peak in time is shown in Figure7.4c.

From Figure7.4a we can see that after 1 hour the peak due to the oxidized particles arises and reaches a steady shape after 12 hours. The position of this second peak is difficult to determine, because of the superposition with the plasmonic peak of the pure silver, that avoids to reliably distinguish the two contributes. In a similar way, the bulk absorbance does not change significantly, meaning that at the measurements temperature (approximately $30°C$) diffusion and aggregation of the silver nanoparticles to the bulk layer is limited. Diffusion and aggregation between the nanoparticles take place in the upper swollen region, causing a redshift of the pure silver peak that changes from 400nm to approximately 410-412nm after 144 hours and then remains stable.

Two sets of samples were measured at the same time after implantation, but one of them was passivated after 36 hours and left at room temperature (approximately $20°C$) for 96 hours for the PDMS passivation layer crosslinking. In order to compare the evolution data, also the first non-passivated set was kept in the same conditions, at a temperature lower than the measurement chamber. This change of temperature could have caused a temporary rearrangement of the nanocomposite or a change in the swollen

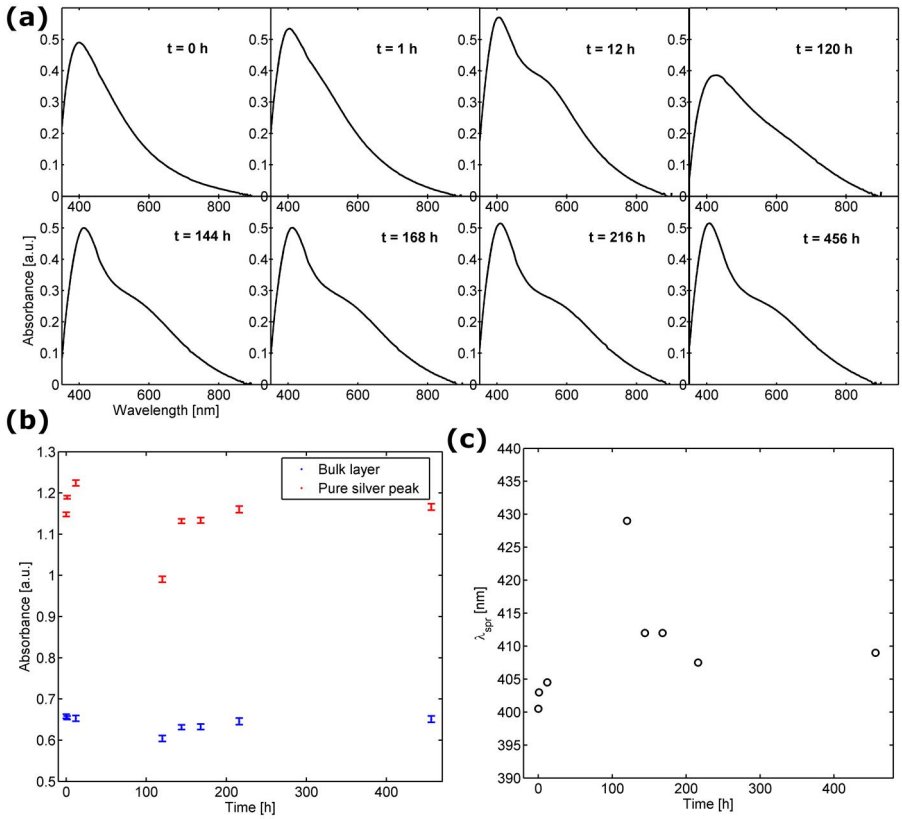

Figure 7.4: (a) Absorbance spectra of the Ag/PDMS nanocomposite sample at eight significative times after implantation. (b) Plot of the absorbance versus time of the intensity of the pure silver peak (the *first peak*) and of the baseline, calculated as the average of the spectrum in the range 850nm-900nm. (c) First peak position in time

polymer density, affecting the optical response of that region of the sample. After having resumed the measurements at $30°C$, the sample recovered the behavior before the passivation of the other set of samples. It is thus clear that the optical response of Ag/PDMS nanocomposites is highly sensitive to slight changes in the environmental temperature. This effect will be deeply investigated in the next section.

7.3 Thermal annealing

In order to investigate the effect of thermal annealing on the optical response of the Ag/PDMS nanocomposites, a set of three samples were heated at different temperatures ($150°C$, $100°C$, and $50°C$) for 1 hour and compared to a sample kept at room temperature, all implanted with an equivalent thickness of 60nm. The results, presented in Figure7.5, show a different behavior between the two samples heated at $150°C$ and $100°C$, and the two samples heated at $50°C$ and kept at room temperature. Samples annealed at $100°C$ and $150°C$ present both the peaks due to pure silver and silver oxide particles, while those annealed at $50°C$ and kept at RT are characterized only by a peak around 400nm due to pure silver nanoparticles, meaning that a temperature of $50°C$ is

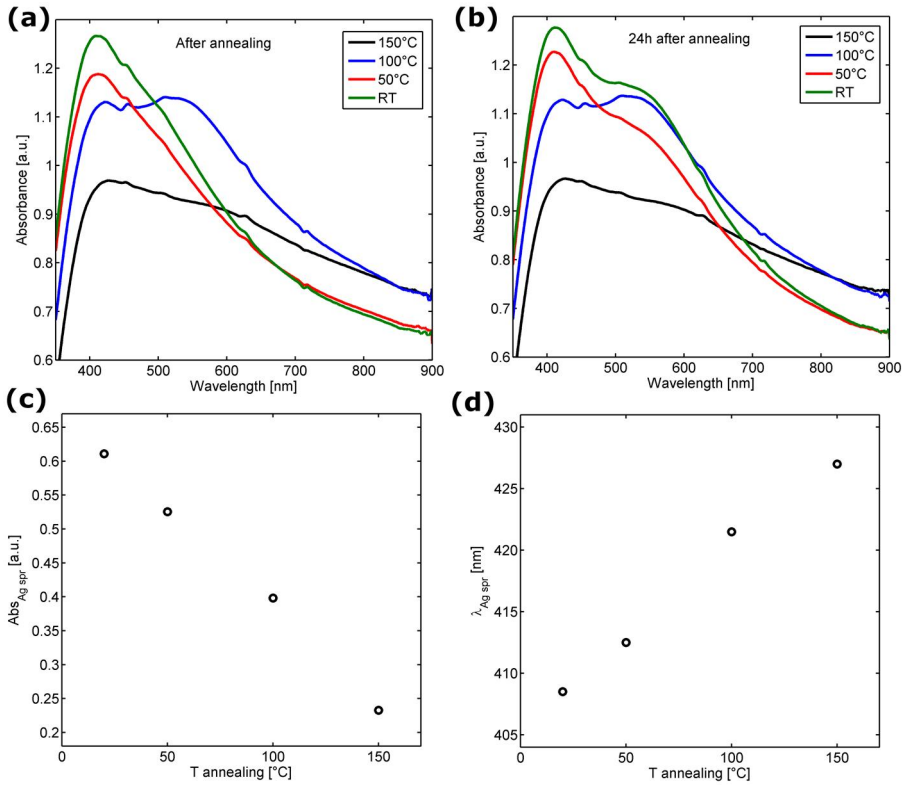

Figure 7.5: Spectra of samples immediately after annealing at different temperatures, indicated in the legend (a), and 24 hours after annealing (b). In (c) and (d) the wavelength and the intensity of the pure silver resonance peak respectively versus the annealing temperature.

not sufficient to trigger an acceleration of the oxidation process. The intensity and position of this first peak for the four samples were highlighted in Figure7.5c and d: with the increase of the annealing temperature the peaks redshift and attenuate. This trend can be explained through the nanocomposite model introduced in the previous sections and with a reduction of the thickness of the swollen region. The shrinking of the swollen polymer region (already observed and measured in [118]) induces an increase of the volume fraction (and thus a redshift) and an increase of the diffusion and aggregation between the nanoparticles and of the nanoparticles to the bulk layer, enhanced by the thermal energy of the annealing process. The reduction of the number of nanoparticles in the swollen region causes a decrease of intensity of the first resonance peak while the aggregation of particles to the bulk layer an increase of the spectra baselines, as clearly visible in Figure7.5a.

24 hours after annealing the four samples were measured again: samples annealed at $100°C$ and $150°C$ are identical to the first measures, while those annealed at $50°C$ and kept at RT show the arising of the peak due to silver oxide, while the baselines of the four samples present no variations (as already observed in Figure7.4b). From these results it is clear that annealing processes at temperatures higher or equal to $100°C$ accelerate the oxidation of the silver nanoparticles and enhance the aggregation of nanoparticles

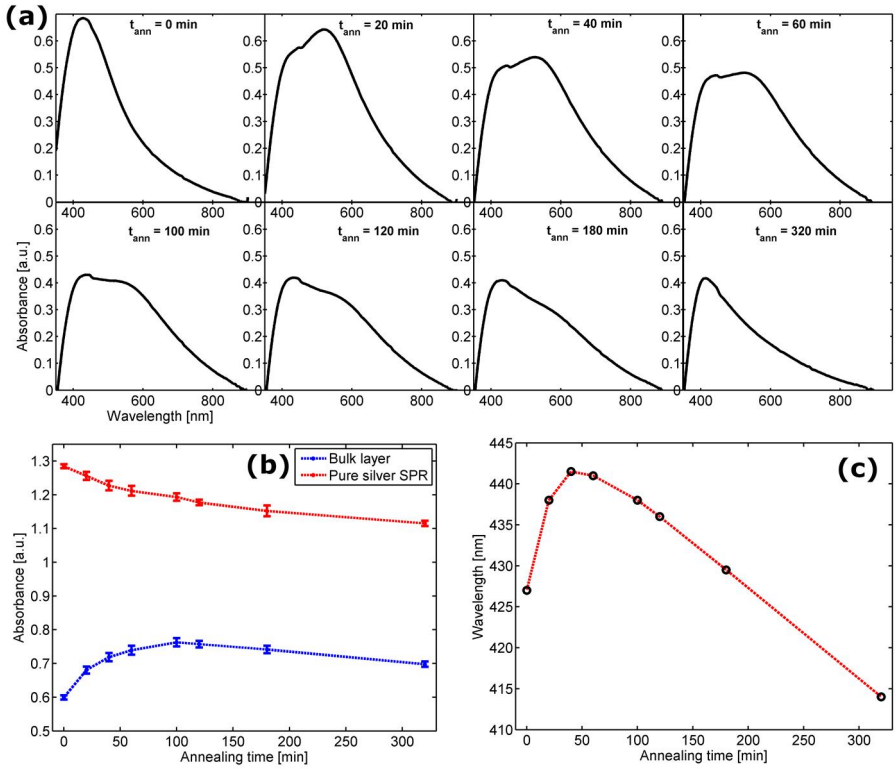

Figure 7.6: (a) Time evolution of the surface plasmon resonance of the Ag/PDMS nanocomposite system: the baseline was subtracted in order to directly compare the shape of spectra. (b) Evolution of the pure silver peak intensity and of the baseline level in time. (c) Time evolution of the pure silver peak position.

to the bulk layer, contributing to a flattening (and intensity *increase*) of the absorbance spectrum, thus affecting reflectance.

The high sensitivity of SCBI Ag/PDMS to temperature, due to the complex nanoparticles internal dynamics, deserves a deeper study of the time evolution of the nanocomposite optical response under prolonged thermal annealing. A set of samples was annealed at $100°C$ and measured each 20 minutes in order to investigate the evolution of the nanoparticles dynamics through surface plasmon resonances. All the samples behave identically, so only the results and analyses relative to one sample are reported in Figure7.6 as representatives.

The silver oxide resonance peak arises after only 20 minutes of annealing at $100°C$ and its intensity is higher than the intensity of the pure silver nanoparticles peak, that decreases because of the strong oxidation reaction activated by the temperature. The evolution shows a strong redshift of the silver oxide peak, accompanied by a decrease in its intensity, as predicted by the shell-core model with an increase of the oxide shell thickness, until its disappearing under the *first* peak.

Time evolution of the pure silver SPR peak intensity and of the spectrum baseline level are plotted in Figure7.6b: the attenuation of the SPR peak intensity is accompanied by an increase of the spectrum baseline. This confirms the hypothesis according to which

thermal annealing improve the silver nanoparticles diffusion and aggregation to the bulk buried layer supposed in the SCBI nanocomposite model.

Also the time evolution of the *position* of the silver nanoparticles peak, shown in Figure7.6c, is interesting. An initial redshift is observed, caused by the nanoparticles aggregation and shrinking of the swollen polymer [118]. After approximately 1 hour a trend inversion and a shift toward shorter wavelengths take place. This behavior can be explained again with the aggregation of silver nanoparticles to the bulk layer together with an adjustment of the polymer volume, causing a decrease of the swollen region volume fraction.

The samples were kept at room temperature for one week and then measured again, without any further significant variation in the absorbance spectra.

7.4 Effect of passivation on SPR

In section 7.2 and 7.3 we have seen that the nanocomposite optical properties change with time and with thermal annealing because of the rearrangement and oxidation of silver nanoparticles and the swelling or shrinking of the superficial layer of the polymeric substrate. A method for the *freezing* of the nanocomposite optical response in a given state is required for the exploitation of the ns-Ag/PDMS system in practical applications. A possible solution relies in the *passivation* of the nanocomposite, consisting in the spin-coating of a second PDMS layer on the implanted nanocomposite. This process also helps in improving the handling and reliability of the nanocomposite based device, since it protects the implanted surface from scratching or sweeping. Moreover, even if PDMS is permeable to oxygen [187], a PDMS capping layer helps also limiting silver nanoparticles oxidation.

Samples in different evolution states (c10 and c11 annealed and c25 kept at room temperature) were passivated with a PDMS capping layer deposited by spin coating at 1000rpm for 60 seconds and crosslinked at RT for 48 hours. Absorption spectra, acquired by uv-vis spectroscopy, are reported in Figure7.7a. Once again the baseline was subtracted from the spectra in order to directly compare the features of the resonance peaks.

The same trend is observed for all the three samples: both the pure silver and the oxidized silver nanoparticles peaks shift toward shorter wavelengths, meaning a decrease both of the silver particles volume fraction according to the Maxwell Garnett model, and of the oxide shell thickness according to the shell-core model. Moreover, also the baseline level decreases, as shown in figure 7.7b. These processes can be explained by means of two different mechanisms. Regarding the decrease of the volume fraction, it is well known that PDMS is highly sensitive to organic solvents present in the PDMS liquid precursor spin-coated on the nanocomposite. Solvents are absorbed by the elastomeric matrix causing a *swelling* of the polymer [101, 102], an increase of the nanocomposite total volume and thus a decrease of the nanoparticles volume fraction. The swelling of the nanocomposite polymeric matrix also drags silver nanoparticles away from the bulk layer, causing a decrease of the observed spectrum baseline level.

The hypothesis at the basis of the silver oxide particles blueshift is more complicated. The PDMS liquid precursor also containes silicone monomers that get cross-linked by a Platinum-complex based catalyzer [196, 197]. PDMS liquid precursor diffuse in the nanocomposite polymer matrix and both silver and silver oxide nanoparticles participate in the crosslinking reaction, causing a *de-oxidation* of the latter. An interaction between the polymer chains and metal nanoparticles was already observed for different

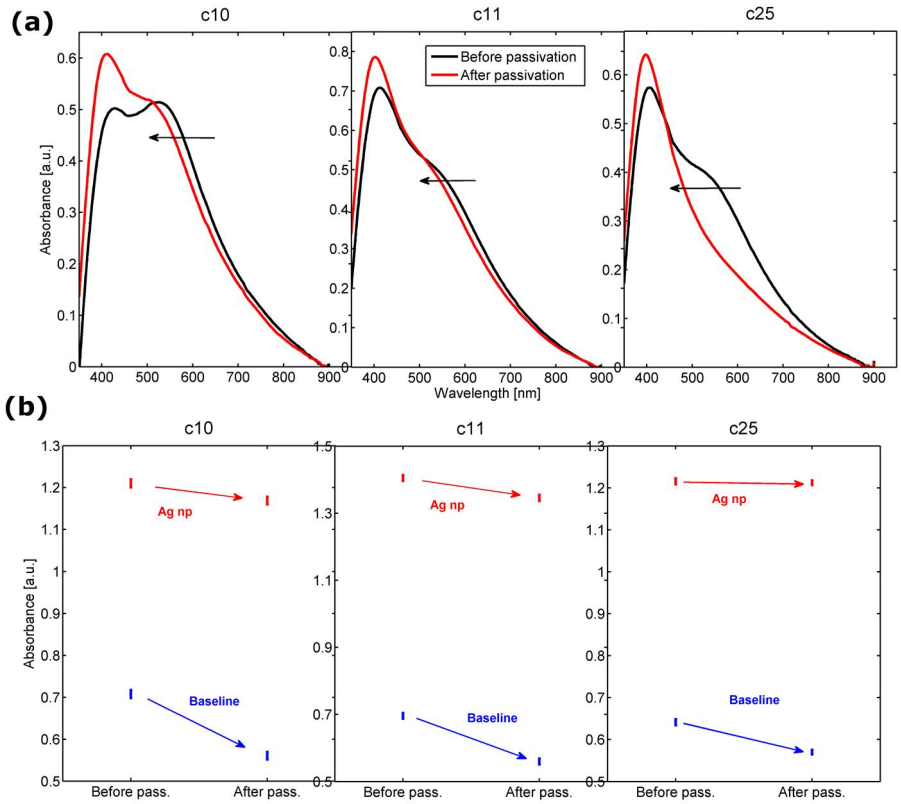

Figure 7.7: Absorption spectra of the nanocomposite samples *before* and *after* the passivation process. (b) Change of intensity of the silver SPR peak and of the spectra baseline level before and after the passivation process.

systems [198, 199], in particular between silicon dioxide substrates and the oxygen of unterminated PDMS chains, of which the liquid PDMS precursor is rich.

The same samples were kept at room temperature after the passivation process and measured again after one week, showing no significant modifications in the optical response. Thus we can conclude that passivation affects the optical properties of the nanocomposite material but the *new state* achieved is freezed and does not undergo further modifications.

7.5 Stretching measurements

Since elastomeric metal-polymer nanocomposites synthesized by SCBI are supposed to be exploited in stretchable or deformable optical devices like mirrors or gratings, a study of the behavior of the optical response of the material subjected to mechanical stress is also necessary. In this section *very preliminary results* regarding a Au/PDMS stretched nanocomposite system will be presented. Gold was chosen instead of Silver as nanocomposite filling metal, thanks to its inertness to oxygen (it does not suffer oxidation like silver) and because the expected surface plasmon resonance peak falls in the middle of the visible range, at approximately 550-600nm, thus large tunabilities can be observed.

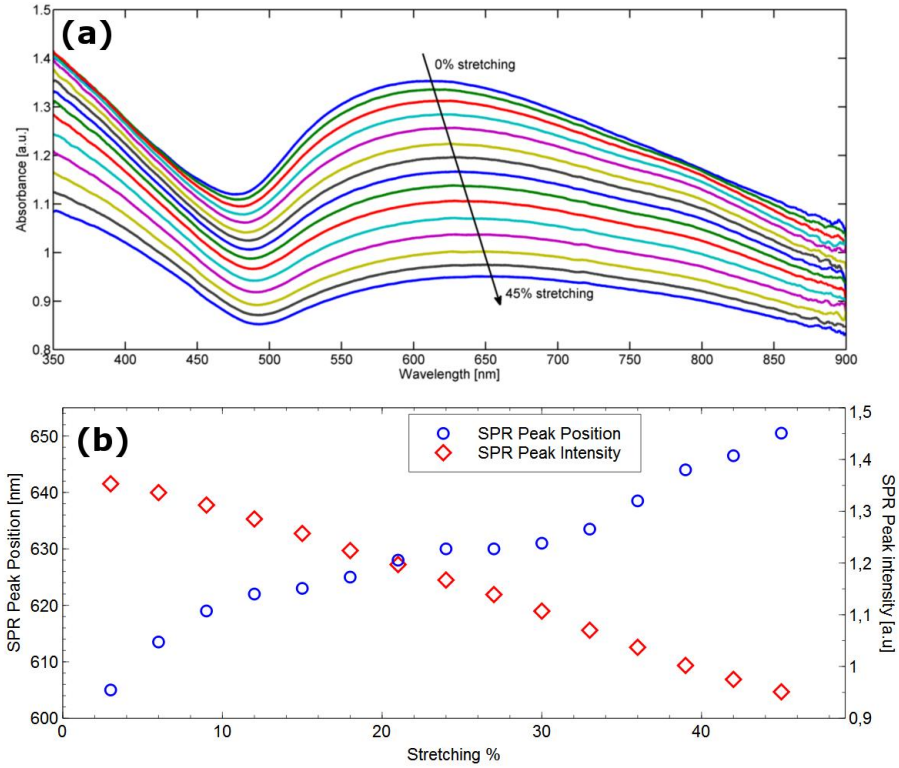

Figure 7.8: (a) Absorbance spectra of stretched Au/PDMS nanocomposite. A clear redshift of the SPR peak position is evident. (b) SPR Peaks position and intensity plotted as a function of the applied strain.

Moreover the behavior of the optical response of the Au/PDMS nanocomposite synthesized by SCBI is already known, since it was characterized by uv-vis spectroscopy [118] as a function of time, thermal annealing and implanted equivalent thickness.

A PDMS substrate was implanted by Supersonic Cluster Beam Implantation with an equivalent thickness of approximately 100nm and then mounted on the uv-vis spectrophotometer modified sample holder. One extremity was clamped (with a Teflon-covered aluminum bar) in a support fixed to the sample holder, while the other side clamped in a moving support, coupled with a computer controlled stepper motor. On the reference beam a freestanding bare PDMS layer serves as background for the measurements. The Au/PDMS nanocomposite was measured two weeks after the implantation process in order to limit the contribution of the SPR natural time evolution due to the diffusion and aggregation of nanoparticles inside PDMS. The nanocomposite film was stretched up to 40% and absorbance spectra acquired at stretching intervals of 3%. The preliminary results are presented in Figure7.8.

During a single stretching cycle a redshift and an attenuation of the SPR Peak is observed. According to Maxwell Garnett theory, a redshift means an increase of the volume fraction and this can be caused by two phenomena: a rearrangement and aggregation of the nanoparticles driven by the stretching of the polymeric chains, and/or a decrease of the nanocomposite total volume because of the shrinking of the polymer in the two

directions orthogonal to the stretching direction, due to the Poisson ratio (that is 0.5 [200] for PDMS). However an attenuation of the SPR peak intensity is observed, at odd with the expectations of the Maxwell Garnett model. This decrease could be explained with an aggregation of the gold nanoparticles to a bulk layer, similarly to the silver case seen in the previous sections, but in this case the baseline can not be determined since gold exhibits a much larger SPR peak, covering a range between 500nm and 900nm. A second hypothesis for the SPR peak attenuation relies on the formation of aggregates oriented in the stretching direction. According to this assumption the same number of nanoparticles gives rise to a lower number of linear aggregates with a high aspect ratio, shifting the SPR toward longer wavelengths, as observed in [201]. Nanoparticles aggregation in structures with larger aspect ratio even without applied stretching was supposed by the comparison of the measured nanocomposite surface Young modulus with theoretical expectations of Guth model seen earlier in section 3.4.3. The formation of nanoparticles aggregates in the stretching direction in deformed metal-polymer nanocomposites was investigated in [202] and is at the basis for the explanation of the improvement of the electrical conductance upon stretching measured in [21, 118].

The rearrangement of the nanoparticles inside the Au/PDMS nanocomposite in the stretching direction may also *linearly polarize* the light passing through the nanocomposite. This effect can be exploited for the direct investigation of the aggregation state of the implanted nanoparticles with uv-vis spectroscopy, measuring the intensity attenuation of transmitted incident light, polarized at different angles by means of a revolving linear polarizer, both in the measure and in the reference beams.

The nanoparticles aggregation status can be also investigated applying the *Bergman model*, introduced in section 6.2, to the obtained uv-vis absorption spectra. The spectral density g obtained from the Bergman model gives information on the distribution of resonances and thus to the structure of the nanoparticle aggregates inside the polymer. However, since the function g is obtained from a fitting procedure of the spectra, a non-trivial genetic algorithm and computational effort are required.

The knowledge of the nanoparticles structure and its effect on the optical properties of the nanocomposite is of great interest for the fabrication and tuning of the elastomeric optical devices characteristics, but serves also for a better understanding of the electronic transport mechanism of such materials.

Conclusions and perspectives

In this thesis I demonstrated the possibility to fabricate reliable nanocomposite-based elastomeric optical components working in reflection by means of Supersonic Cluster Beam Implantation. Unlike reflective elastomeric optical components fabricated by classical techniques the resilience of the metal-elastomer nanocomposite ensures a sufficient elasticity of the reflective layer while maintaining an extremely low surface smoothness, limiting the fraction of scattered light. The superior optical and mechanical properties of these devices compared to currently available elastomer metallization techniques allowed to design and to build cheaper and simpler novel optical instruments like monochromators and spectrometers, characterized by an easier and linear wavelength selection respect to currently available commercial spectrophotometers. In particular SCBI elastomeric optical components applied to arbitrarily shaped and non-optical grade surfaces can replace and add new features to existing concave diffraction gratings, opening the way to the use of our elastomeric components in novel cheaper and easier optical setups and instruments.

The optical properties of elastomeric optical devices can be finely tuned during the nanocomposite synthesis and with post-implantation thermal treatments, as shown by the study of the behavior of Surface Plasmon Resonance observed in the nanocomposite absorption spectra. In particular I demonstrated that passivation of the nanocomposite layer helps in preventing silver nanoparticles oxidation and mobility, and improving the handling of the device. Preliminary results on the optical behavior of the nanocomposite upon stretching, suggesting a re-arrangement of the nanoparticles inside the polymer, are particularly encouraging in view of a better understanding both of the behavior of elastomeric tunable gratings or mirrors.

The results obtained in this work open new research opportunities and possible applications of elastomeric optical devices. Among these applicative fields deformable mirrors for small adaptive optics systems and hyperspectral imaging systems, exploiting the resilience of elastomeric mirrors and the imaging capabilities of arbitrarily shaped elastomeric diffraction gratings respectively, are the most promising.

Reflective membranes, actuated by electrostatic forces, for cheap and reliable compact adaptive optics systems can be easily fabricated by means of SCBI Ag/PDMS nanocomposites. The reflectivity of our nanocomposites can be combined with the possibility to create conductive nanocomposite micropatterns [21, 22] by means of SCBI with stencil masks without any deterioration of the elastomer. The result would be a single reflective elastomeric device comprising patterned electrodes, representing the ideal candidate for the replacement of currently available continuous faceplates mirrors, affected by a high fragility and a complex (and expensive) piezoelectric-based actuation system.

Finally, reflective elastomeric nanocomposite-based diffraction gratings synthesized by SCBI may represent a significative breakthrough, making hysperspectral imaging systems commonly available and useful in everyday life. Our elastomeric devices would overcome the limited focusing and imaging capabilities of existing diffraction gratings. The high fabrication cost of concave gratings or the large dimensions and costs of alternative mounts, based on planar gratings and complex focusing and corrective systems, limit the use of hyperspectral imaging in niche applications [203, 204]. Novel cheaper, simpler and more compact hyperspectral imaging systems can be developed thanks to the results relative to the applications of nanocomposite-based elastomeric gratings to arbitrarily shaped non optical grade surfaces. Images can be thus diffracted, focused and off-axis aberrations corrected by a single inexpensive elastomeric optical component.

Bibliography

[1] H. W. Babcock. The possibility of compensating astronomical seeing. *Pub. Astr. Soc. Pac.*, 65:229, 1953.

[2] A. Buffington, F. S. Crawford, R. A. Muller, A. J. Schemin, and R. G. Smits. *J. Opt. Soc. Am.*, 67:298, 1977.

[3] A. Buffington, F. S. Crawford, R. A. Muller, and C. D. Orth. *J. Opt. Soc. Am.*, 67:304, 1977.

[4] J. W. Hardy, J. E. Lefebvre, and C. L. Koliopoulos. Real-time atmospheric compenstion. *J. Opt. Soc. Am.*, 67:360, 1977.

[5] P. Wizinowich, D. S. Acton, C. Shelton, P. Stomski, J. Gathright, K. Ho, W. Lupton, K. Tsubota, O. Lai, C. Max, J. Brase, J. An, K. Avicola, S. Olivier, D. Gavel, , B. Macintosh, A. Ghez, and J. Larkin. First light adaptive optics images from the keck ii telescope: A new era of high angular resolution imagery. *Pub. Astr. Soc. Pac.*, 112:315, 2000.

[6] R. B. Dunn. *Proc. SPIE*, 1271:216, 1990.

[7] R. C. Smithson. *Proc. SPIE*, 779:18, 1987.

[8] R. C. Smithson, M. L. Peri, and R. S. Benson. *Appl. Opt.*, 27:1615, 1988.

[9] F. Merkle, K. Freischlad, and H. L. Reischmann. Deformable mirror with combined piezoelectric and electrostatic actuators. *Proc. SPIE*, 332:260, 1982.

[10] O. Solgaard, F. S. A. Sandejas, and D. M. Bloom. Deformable grating optical modulator. *Opt. Lett.*, 17:688, 1992.

[11] Y. T. Yu, W. Z. Yuan, T. P. Li, and B. Yan. Develpment of a micromechanical pitch-tunable grating with reflective/transmissive dual working modes. *J. Micromech. Microeng.*, 20:065002, 2010.

[12] J. L. Wilbur, R. J. Jackman, and G. M. Whitesides. Elastomeric optics. *Chem. Mater.*, 8:1380, 1996.

[13] T. Bifano. Mems deformable mirrors. *Nat. Photonics*, 5:21, 2011.

[14] N. J. Douville, Z. Li, S. Takayama, and M. D. Thouless. Fracture of metal coated elastomers. *Soft Matter*, 7:6493, 2011.

[15] Y. Shao and M. A. Brook. Structured metal films on silicone elastomers. *J. Mater. Chem.*, 20:8548, 2010.

[16] G. Ouyang. *Hybrid Integrated Components for Optical Display Systems - Electroactive Polymer Based Micro-Opto-Electro-Mechanical Actuators*. PhD thesis, Department of Physics, University of Oslo, 2012.

[17] W. Caseri. Nanocomposites of polymers and metals or semiconductors: Historical background and optical properties. *Macromol. Rapid Commun.*, 21:705, 2000.

[18] K. R. Berry Jr, A. G. Russell, P. A. Blake, and D. K. Roper. Gold nanoparticles reduced in situ and dispersed in polymer thin films: optical and thermal properties. *Nanotechnology*, 23:375703, 2012.

[19] S. Rosset. *Metal Ion Implanted Electrodes for Dielectric Elastomer Actuators*. PhD thesis, Programme doctoral en microsystémes et microélectronique - EPFL, 2009.

[20] M. Niklaus, S. Rosset, P. Dubois, M. Dadras, and H. Shea. Modification of conductivity and of mechanical properties of electroactive polymer (eap) thin films by titanium ion implantation. In *MRS Fall Meeting 2007*, 2007.

[21] G. Corbelli, C. Ghisleri, M. Marelli, P. Milani, and L. Ravagnan. Highly-deformable nanostructured elastomeric electrodes with improving conductivity upon cyclical stretching. *Adv. Mater.*, 23(39):4504, 2011.

[22] C. Ghisleri, F. Borghi, L. Ravagnan, A. Podestá, C. Melis, L. Colombo, and P. Milani. Patterning of gold-polydimethylsiloxane (au-pdms) nanocomposites by supersonic cluster beam implantation. *J. Phys. D: Appl. Phys.*, 47:015301, 2014.

[23] C. Ghisleri, M. Siano, L. Ravagnan, M. A. C. Potenza, and P. Milani. Nanocomposite-based stretchable optics. *Laser & Photon. Rev.*, 7:1020, 2013.

[24] C. Ghisleri, A. Annoni, S. Capra, M. A. C. Potenza, L. Ravagnan, and P. Milani. A simple scanning spectrometer based on a stretchable reflective grating. *Applied Physics Letters*, Submitted, 2013.

[25] M. Loktev, O. Soloviev, and G. Vdovin, editors. OKO Technologies, 2008.

[26] Multiple Authors. *Adaptive Optics for Vision Science: principles, practices, design and applications*. Wiley-Interscience, 2006.

[27] J. M. Beckers. Adaptive optics for astronomy: Principles, performance, and applications. *Annu. Rev. Astron. Astrophys.*, 31:13, 1993.

[28] N. R. Zelmanovitch. The outreach plan around the ?rst science with the gran telescopio canarias (gtc). *Proceedings IAU Symposium*, 260:1, 2009.

[29] W. G. Hulburd. Segmented mirrors for atmospheric compensation. *Proc. SPIE*, 1130:42, 1989.

[30] A. Roorda. Adaptive optics ophthalmoscopy. *J. Refract. Surg.*, 16:S602, 2000.

[31] EASO. The 4m international liquid mirror telescope project - http://www.aeos.ulg.ac.be/lmt/index.php.

[32] P. Laird, N. Caron, M. Rioux, E. F. Borra, and A. Ritcey. Ferrofluidic adaptive mirrors. *Appl. Opt.*, 45:3495, 2006.

[33] D. Brousseau, E. F. Borra, and S. Thibault. Wavefront correction with a 37-actuator ferrofluid deformable mirror. *Opt. Express*, 15:18190, 2007.

[34] A. Iqbal and F. B. Amara. Modeling of a magnetic-fluid deformable mirror for retinal imaging adaptive optics systems. *Int. J. Optomech.*, 1:180, 2007.

[35] A. Iqbal and F. B. Amara. Modeling and experimental evaluation of a circular magnetic-fluid deformable mirror. *Int. J. Optomech.*, 2:126, 2008.

[36] James webb space telescope (jwst) indepent comprehensive review panel (icrp) final report. Technical report, NASA, 2012.

[37] T. Young. On the mechanism of the eye. *Phil. Trans. R. Soc. Lond.*, 91:23, 1801.

[38] H. Helmoltz. *Physiological Optics*. Optical Society of America, Rochester (NY), 1924.

[39] M. S. Smirnov. Measurement of the wave aberration of the human eye. *Biofizika*, 6:687, 1961.

[40] A. W. Dreher, J. F. Bille, and R. N. Weinreb. Active optical depth resolution improvement of the laser tomographic scanner. *Appl. Opt.*, 28:804, 1989.

[41] J. Liang, B. Grimm, S. Goelz, and J. F. Bille. Objective measurement of wave aberrations of the human eye with the use of a hartmann-shack wave-front sensor. *J. Opt. Soc. Am. A*, 11:1949, 1994.

[42] J. Liang and D. R. Williams. Aberrations and retinal image quality of the normal human eye. *J. Opt. Soc. Am. A*, 14:2873, 1997.

[43] H. Hofer, P. Artal, B. Singer, J. L. Aragon, and D. R. Williams. Dynamics af the eye's aberrations. *J. Opt. Soc. Am. A*, 18:497, 2001.

[44] J. Caroll, D. C. Gray, A. Roorda, and D. R. Williams. Recent advances in retinal imaging with adaptive optics. *Opt. Photon. News*, 16:36, 2005.

[45] A Roorda and D. R. Williams. The arrangement of the three cone classes in the living human eye. *Nature*, 397:520, 1999.

[46] M. J. Booth. Adaptive optics in microscopy. *Phil. Trans. R. Soc. Lond. A*, 365:2829, 2007.

[47] O. Albert, L. Sherman, G. Mourou, T. B. Norris, and G. Vdovin. Smart microscope: an adaptive optics learning system for aberration correction in multiphoton confocal microscopy. *Opt. Lett.*, 25:52, 2000.

[48] M. J. Booth, M. A. A. Neil, R. Juškaitis, and T. Wilson. Adaptive aberration correction in a confocal microscope. *Proc. Natl Acad. Sci. USA*, 99:5788, 2002.

[49] B. F. Grewe, F. F. Voigt, M. van 't Hoff, and F. Helmchen. Fast two-layer two-photon imaging of neuronal cell populations using an electrically tunable lens. *Biomed. Opt. Express*, 2:2035, 2011.

[50] F. Druon, G. Chériaux, J. Faure, J. Nees, M. Nantel, A. Maksimchuk, G. Mourou, J. C. Chanteloup, and G. Vdovin. Wave-front correction of femtosecond terawatt lasers by deformable mirrors. *Opt. Lett.*, 23:1043, 1998.

[51] W. Zeller, L. Naehle, P. Fuchs, F. Gerschuetz, L. Hildebrandt, and J. Koeth. Dfb lasers between 760nm and 16μm for sensing applications. *Sensors*, 10:2492, 2010.

[52] J. Alemán, A. V. Chadwick, J. He, M. Hess, K. Horie, R. G. Jones, P. Kratochvíl, I. Meisel, I. Mita, G. Moad, S. Penczek, and R. F. T. Stepto. Definitions of terms relating to the structure and processing of sols, gels, networks, and inorganic-organic hybrid materials. *Pure Appl. Chem.*, 79:1801, 2007.

[53] D. Qin, Y. Xia, and G. M. Whitesides. Elastomeric light valves. *Adv. Mater.*, 9:407, 1997.

[54] C. Yang, K. Shi, P. Edwards, and Z. Liu. Demonstration of a pdms based hybrid grating and fresnel lens (g-fresnel) device. *Opt. Express*, 18:23529, 2010.

[55] A. N. Simonov, O. Akhzar-Mehr, and G. Vdovin. Light scanner based on a viscoelastic stretchable grating. *Opt. Lett.*, 30:949, 2005.

[56] A. N. Simonov, S. Grabarnik, and G. Vdovin. Stregrating diffraction gratings for spectrometry. *Opt. Express*, 15:9784, 2007.

[57] S. Rosset, B. M. OB́rien, T. Gisby, D. Xu, H. R. Shea, and I. A. Anderson. Self-sensing dielectric elastomer actuators in closed-loop operation. *Smart Mater. Struct.*, 22:104018, 2013.

[58] S. C. Truxal, K. Kurabayashi, and Y. C. Tung. Design of a mems tunable polymer grating for single detector spectroscopy. *Int. J. Optomech.*, 2:75, 2008.

[59] B. A. Grzybowski, S. T. Brittain, and G. M. Whitesides. Thermally actuated interferometric ssensor based on the thermal expansion of transparent elastomeric media. *Rev. Sci. Instrum.*, 70:2031, 1999.

[60] G. Ye and X. Wang. Polymer diffraction gratings on stimuli-responsive hydrogel ssurface: Soft-litographic fabrication and optical sensing properties. *Sens. Actua-*

tors, B, 147:707, 2010.
[61] Patent us 7453646 b2 - fluidic adaptive lens systems and methods, 2008.
[62] M. C. Hutley. *Diffraction gratings*. Academic Press, 1982.
[63] C. Palmer. *Diffraction Grating Handbook*. Newport Corporation, 2005.
[64] G. Y. Tian, R. S. Lu, and D. Gledhill. Surface measurement using active vision and light scattering. *Opt. Laser Eng.*, 45:131, 2007.
[65] H. E. Bennett and J. O. Porteus. Relation between surface roughness and specular reflectance at normal incidence. *Journal of the Optical Society of America*, 51:123, 1961.
[66] P. Beckmann and A. Spizzichino. *The Scattering of Electromagnetic Waves from Rough Surfaces*. Pergamon, Oxford, 1965.
[67] T. Li and Z. Suo. Ductility of thin metal films on polymer substrates modulated by interfacial adhesion. *Int. J. Solids Struct.*, 44:1696, 2007.
[68] T. Li, Z. Huang, Z. Suo, S. P. Lacour, and S. Wagner. Stretchability of thin metal films on elastomer substrates. *Appl. Phys. Lett.*, 85:3435, 2004.
[69] H. Huang and F. Spaepen. Tensile testing od free-standing cu, ag and al thin films and ag/cu multilayers. *Acta mater.*, 48:3261, 2000.
[70] S. L. Chiu and P. S. Ho. Fracture of metalpolymer line structure. i. semiflexible polymide. *J. Appl. Phys.*, 76:5136, 1994.
[71] Y. Xiang, T. Li, Z. Suo, and J. J. Vlaassak. High ductility of a metal film adherent on a polymer substrate. *Appl. Phys. Lett.*, 87:161910, 2005.
[72] S. P. Lacour, D. Chan, S. Wagner, T. Li, and Z. Suo. Mechanisms of reversible stretchability of thin metal films on elastomeric substrates. *Appl. Phys. Lett.*, 88:204103, 2006.
[73] B. Budiansky and R. J. O'connell. Elastic moduli of a cracked solid. *Int. J. Solids Struct.*, 12:81, 1976.
[74] N. Laws and J. R. Brokenbrough. The effect of micro-crack systems on the loss of stiffness of brittle solids. *Int. J. Solids Struct.*, 23:1247, 1987.
[75] M. R. Begley, O. N. Scott, M. Utz, and H. Bart-Smith. Fracture of nanoscale copper films on elastomer substrates. *Appl. Phys. Lett.*, 95:231914, 2009.
[76] S. P. Lacour, S. Wagner, Z. Huang, and Z. Suo. Stretchable gold conductors on elastomeric substrates. *Appl. Phys. Lett.*, 82:2404, 2003.
[77] I. M. Graz, D. P. J. Cotton, and S. P. Lacour. Extended cyclic uniaxial loading of stretchable gold thin-films on elastomeric substrates. *Appl. Phys. Lett.*, 94:071902, 2009.
[78] S. Olcum, A. Kocabas, G. Ertas, A. Atalar, and A. Aydinli. Tunable surface plasmon resonance on an elastomeric substrate. *Opt. Express*, 17:8542, 2009.
[79] N. Bowden, S. Brittain, A. G. Evans, J. W. Hutchinson, and G. M. Whitesides. Spontaneous formation of ordered structures in thin flms of metals supported on an elastomeric polymer. *Nature*, 393:146, 1998.
[80] J. Y. Chung, A. J. Nolte, and C. M. Stafford. Surface wrinkling: A versatile platform for measuring thin-film properties. *Adv. Mater.*, 23:349, 2011.
[81] R. A. Guerrero, J. T. Barretto, J. L. V. Uy, I. B. Culaba, and B. O. Chan. Effects of spontaneous surface buckling on the diffraction performance of an au-coated elastomeric grating. *Opt. Commun.*, 270:1, 2007.
[82] M. Aschwanden and A. Stemmer. Polymeric, electrically tunable diffraction grating based on artificial muscles. *Opt. Lett.*, 31:2610, 2006.
[83] N. Galler, H. Ditlbacher, B. Steinberger, A. Hohenau, M. Dansaschmüller,

F. Camacho-Gonzales, S. Bauer, J. R. Krenn, A. Leitner, and F. R. Ausseneg. Electrically actuated elastomers for electro-optical modulators. *Appl. Phys. B*, 85:7, 2006.

[84] K. Wetzig and C. M. Shneider. *Metal based thin films for electronics*. Wiley-VCH GmbH and Co. KGaA, Weinheim, 2003.

[85] M. Kolle, B. Zheng, N. Gibbons, J. J. Baumberg, and U. Steiner. Stretch-tuneable dielectric mirrors and optical microcavities. *Opt. Express*, 18:4356, 2010.

[86] S. P. Lacour, J. Jones, Z. Suo, and S. Wagner. Design and performance of thin metal film interconnects for skin-like electronic circuits. *IEEE Electr. Device Lett.*, 25:179, 2004.

[87] Y. W. Jiang, F. T. Chuang, H. H. Chen, and S. C. Lee. Self-assembled rippling structure based on metal-elastomer composite for tunable plasmonics. *IEEE Phot. Technol. Lett.*, 23:670, 2011.

[88] E. Guth. Theory of filler reinforcement. *J. Appl. Phys.*, 16:20, 1945.

[89] Y. P. Wu, Q. X. Jia, D. S. Yu, and L. Q. Zhang. Modeling young's modulus of rubber-clay nanocomposites using composite theories. *Polym. Testing*, 23:903, 2004.

[90] L. Nicolais and G. Carotenuto. *Metal-polymer nanocomposites*. Wiley, 2005.

[91] A. B. R. Mayer. Formation of noble metal nanoparticles within a polymeric matrix: nanoparticle features and overall morphologies. *Mater. Sci. Eng. C*, 6:155, 1998.

[92] F. Faupel, V. Zaporojtchenko, H. Greve, U. Schürmann, V. S. K. Chakravadhanula, Ch. Hanish, A. Kulkarni, A. Gerber, E. Quandt, and R. Podschun. Deposition of nanocomposites by plasmas. *Contrib. Plasma Phys.*, 47:537, 2007.

[93] V. Zaporojtchenko, R. Podschun, U. Schürmann, A. Kulkarni, and F. Faupel. Physico-chemical and antimicrobial properties of co-sputtered ag/au-ptfe nanocomposite coatings. *Nanotechnology*, 17:4904, 2006.

[94] C. V. Bechtolsheim, V. Zaporojtchenko, and F. Faupel. Influence of thermal treatment on the morphology and adhesion of gold films on trimethylcyclohexanepolycarbonate. *Appl. Phys. Surf.*, 151:119, 1999.

[95] D. V. Gioia. Preparation and formation mechanisms of uniform metallic particles in homogeneous solutions. *J. Mater. Chem.*, 14:451, 2004.

[96] M. Iwamoto, K. Kuroda, V. Zaporojtchenko, S. Hayashi, and F. Faupel. Production of gold nanoparticles-polymer composite by quite simple method. *Eur. Phys. J. D*, 24:365, 2003.

[97] D. Bloor, K. Donnelly, P. J. Hands, P. Laughlin, and D. Lussey. A metal-polymer composite with unusual properties. *J. Phys. D: Appl. Phys.*, 38:2851, 2005.

[98] Z. Lu, G. Liu, and S. Duncan. Poly(2-hydroxyethyl acrylate-co-methyl acrylate)/sio2/tio2 hybrid membranes. *J. Membr. Sci.*, 221:113, 2003.

[99] R. A. Zoppi, S. das Neves, and S. P. Nunes. Hybrid films of poly(ethylene oxide-b-amide-6) containing sol-gel silicon or titanium oxide as inorganic fillers: effect of morphology and mechanical properties on gas permeability. *Polymer*, 41:5461, 2000.

[100] U. Kreibig and M. Vollmer. *Optical Properties of Metal Clusters*. Springer, 1995.

[101] J. N. Lee, C. Park, and G. M. Whitesides. Solvent compatibility of poly(dimethylsiloxane)-based microfluidic devices. *Anal. Chem.*, 75:6544, 2003.

[102] A. Mata, A. J. Fleischman, and S. Roy. Characterization of polydimethylsiloxane (pdms) properties for biomedical micro/nanosystems. *Biomed. Microdevices*, 7:281, 2005.

[103] R. Ruggerone. *Highly Filled Polymer Nanocomposite Films Derived from Novel Nanostructured Latexes*. PhD thesis, Programme doctoral en science et génie des

matériaux., 2009.

[104] D. Fragiadakis, P. Pissis, and L. Bokobza. Glass transition and molecular dynamics in poly(dimethylsiloxane)/silica nanocomposites. *Polymer*, 46:6001, 2005.

[105] H. Zou, S. Wu, and J. Shen. Polymer/silica nanocomposites: Preparation, characterization, properties, and applications. *Chem. Rev.*, 108:3893, 2008.

[106] S. Rosset and H. R. Shea. Flexible and stretchable electrodes for dielectric elastomer actuators. *Appl. Phys. A*, 110:281, 2013.

[107] P. Dubois, S. Rosset, S. Koster, J. Stauffer, S. Mikhaïlov, M. Dadras, N. de Rooij, and H. Shea. Microactuators based on ion implanted dielectric electroactive polymer (eap) membranes. *Sens. Actuators, A*, 130-131:147, 2006.

[108] S. Rosset, M. Niklaus, P. Dubois, and H. R. Shea. Metal ion implantation for the fabrication of stretchable electrodes on elastomers. *Adv. Funct. Mater.*, 19:470, 2009.

[109] A. L. Stepanov, D. E. Hole, and P. D. Townsed. Reflectance of the dielectric layers containing metal nanoparticles formed by ion implantation. *J. Non-Cryst. Solids*, 244:275, 1999.

[110] A. L. Stepanov. Synthesis of silver nanoparticles in dielectric matrix by ion implantation: a review. *Rev. Adv. Mater. Sci.*, 26:1, 2010.

[111] M. Niklaus, S. Rosset, and H. Shea. Array of lenses with individually tunable focal-length based on transparent ion-implanted eaps. *Proc. SPIE*, 7642:1, 2010.

[112] T. K. Shih, C. F. Chen, J. R. Ho, and F. T. Chuang. Fabrication of pdms (polydimethylsiloxane) microlens and diffuser using replica molding. *Microelectron. Eng.*, 83:2499, 2006.

[113] P. J. Flory. Molecular theory of rubber elasticity. *Polym. J.*, 17:1, 1985.

[114] L. Ravagnan, G. Divitini, S. Rebasti, M. Marelli, P. Piseri., and P. Milani. Poly(methyl methacrylate)-palladium clusters nanocomposite formation by supersonic cluster beam deposition: a method for microstructured metallization of polymer surfaces. *J. Phys. D: Appl. Phys.*, 42:082002, 2009.

[115] M. Marelli, G. Divitini, C. Collini, L. Ravagnan, G. Corbelli, C. Ghisleri, A. Gianfelice, C. Lenardi, P. Milani, and L. Lorenzelli. Flexible and biocompatible microelectrode arrays fabricated by supersonic cluster beam deposition on su-8. *J. Micromech. Microeng.*, 21:045013, 2011.

[116] K. Wegner, P. Piseri, H. V. Tafreshi, and P. Milani. Cluster beam deposition: a tool for nanoscale science and technology. *J. Phys. D: Appl. Phys.*, 39:R439, 2006.

[117] H. Haberland, Z. Insepov, and M. Moseler. Molecular-dynamics simulation of thin-film growth by energetic cluster impact. *Phys. Rev. B*, 51:11061, 1995.

[118] G. Corbelli. *Synthesis and characterization of metal-polymer nanocomposites for stretchable electronics applications*. PhD thesis, Doctorate School in Physics, Astrophysics and Applied Physics - University of Milan, 2012.

[119] G. Bongiorno, A. Podestá, L. Ravagnan, P. Piseri, P. Milani, C. Lenardi, S. Miglio, M. Bruzzi, and C. Ducati. Electronic properties and applications of cluster-assembled carbon films. *J. Mater. Sci.: Mater Electron*, 17:427, 2006.

[120] E. Barborini, G. Corbelli, G. Bertolini, P. Repetto, M. Leccardi, S. Vinati, and P. Milani. The influence of nanoscale morphology on the resistivity of cluster-assembled nanostructured metallic thin films. *New J. Phys.*, 12:073001, 2010.

[121] L. Diederich, E. Barborini, P. Piseri, A. Podestá, P. Milani, A. Schneuwly, and R. Gallay. Supercapacitors based on nanostructured carbon electrodes grown by cluster-beam deposition. *Appl. Phys. Lett.*, 75:2662, 1999.

[122] L. G. Bettini, G. Bardizza, A. Podestá, P. Milani, and P. Piseri. Electrochemical

impedance spectroscopy on nanostructured carbon electrodes grown by supersonic cluster beam deposition. *J. Nanopart. Res.*, 15:1429, 2013.

[123] M. Bruzzi, S. Miglio, M. Scaringella, G. Bongiorno, P. Piseri, A. Podestá, and P. Milani. First study of humidity sensors based on nanostructured carbon films produced by supersonic cluster beam deposition. *Sens. Actuators, B*, 100:173, 2004.

[124] T. Mazza, E. Barborini, I. N. Kholmanov, P. Piseri, G. Bongiorno, S. Vinati, P. Milani, C. Ducati, D. Cattaneo, A. Li Bassi, C. E. Bottani, A. M. Taurino, and P. Siciliano. Libraries of cluster-assembled titania films for chemical sensing. *Appl. Phys. Lett.*, 87:103108, 2005.

[125] A. Podestá, G. Bongiorno, P. E. Scopelliti, S. Bovio, P. Milani, C. Semprebon, and G. Mistura. Cluster-assembled nanostructured titanium oxide films with tailored wettability. *J. Phys. Chem. C*, 113:18264, 2009.

[126] R. Carbone, I. Marangi, A. Zanardi, L. Giorgetti, E. Chierici, G. Berlanda, A. Podestá, F. Fiorentini, G. Bongiorno, P. Piseri, P. G. Pellicci, and P. Milani. Biocompatibility of cluster-assembled nanostructured tio2 with primary and cancer cells. *Biomaterials*, 27:3221, 2006.

[127] P. Milani and S. Iannotta. *Cluster Beam Synthesis of Nanostructured Materials*. Springer, 1999.

[128] H. V. Tafreshi, G. Benedek, P. Piseri, S. Vinati, E. Barborini, and P. Milani. Aerodynamic focusing of clusters into a high intensity and low divergence supersonic beam. *Europ. Phys. J. Appl. Phys.*, 16:149, 2001.

[129] H. V. Tafreshi, G. Benedek, P. Piseri, S. Vinati, E. Barborini, and P. Milani. A simple nozzle configuration for the production of low divergence supersonic cluster beam by aerodynamic focusing. *Aerosol Sci. Technol.*, 36:593, 2002.

[130] Y. Yamamura and T. Muramoto. Depth profiles due to big cluster impacts. *Phys. Rev. Lett.*, 69:1463, 1992.

[131] C. Anders and H. M. Urbassek. Dependence of cluster ranges on target cohesive energy: Molecular-dynamics study of energetic au_{402} cluster impacts. *Nucl. Instrum. Methods Phys. Res., Sect. B*, 266:44, 2008.

[132] S. J. Carroll, P. D. Nellist, and R. E. Palmer. Shallow implantation of "size-selected" ag clusters into graphite. *Phys. Rev. Lett.*, 84:2654, 2000.

[133] V. N. Popok, I. I. Azarko, R. I. Khaibullin, A. L. Stepanov, V. Hnatowicz, A. Mackova, and S. V. Prasalovich. Radiation-induced change of polyimide properties under high-fluence and high ion current density implantation. *Appl. Phys. A*, 78:1067, 2004.

[134] R. Cardia, C. Melis, and L. Colombo. Neutral-cluster implantation in polymers by computer experiments. *J. Appl. Phys.*, 113:224307, 2013.

[135] E. Barborini, P. Piseri, and P. Milani. A pulsed microplasma source of high intensity supersonic carbon cluster beams. *J. Phys. D: Appl. Phys.*, 32:L105, 1999.

[136] P. Milani and W. A. deHeer. Improved pulsed laser vaporization source for production of intense beams of neutral and ionized clusters. *Rev. Sci. Instrum.*, 61:1835, 1990.

[137] P. R. Willmott and J. R. Huber. Pulsed laser vaporization and deposition. *Rev. Mod. Phys.*, 72:315, 2000.

[138] H. R. Siekmann, Ch. Lüder, J. Faehrmann, H. O. Lutz, and K. H. Meiwes-Broer. The pulsed arc cluster ion source (pacis). *Z. Phys. D*, 20:417, 1991.

[139] NIST. Persistent lines of neutral mercury (hg i) - http://physics.nist.gov/.

[140] S. Prahl. Rhodamine b - http://omlc.ogi.edu/spectra/photochemcad/index.html.

[141] C. Kittel. *Introduction to Solid State Physics, 8th Edition*. John Wiley & Sons, 2005.
[142] N. W. Ashcroft and N. D. Mermin. *Solid State Physics*. Holt Rinehart & Winston, 1976.
[143] P. Drude. Zur elektronentheorie der metalle. *Annalen der Physik*, 306:566, 1900.
[144] J. N. Anker, W. P. Hall, O. Lyandres, N. C. Shah, J. Zhao, and R. P. van Duyne. Biosensing with plasmonic nanosensors. *Nat. Mater.*, 7:442, 2008.
[145] J. Homola. Present and future of surface plasmon resonance biosensors. *Anal. Bioanal. Chem.*, 377:528, 2003.
[146] X. Huang, I. H. El-Sayed, W. Qian, and M. A. El-Sayed. Cancer cell imaging and photothermal therapy in the near-infrared region by using gold nanorods. *J. Am. Chem. Soc.*, 128:2115, 2006.
[147] IV K. C. L. Black. *Biomimetic Strategies Employed in the Formation of Biotargeted Metal Nanoparticles for Optical Imaging and Photothermal Therapy*. PhD thesis, Northwestern University, 2012.
[148] T. H. Meen, J. K. Tsai, S. M. Chao, Y. C. Lin, T. C. Wu, T. Y. Chang, L. W. Ji, W. Water, W. R. Chen, I. T. Tang, and C. J. Huang. Surface plasma resonant effect of gold nanoparticles on the photoelectrodes of dye-sensitized solar cells. *Nanoscale Res. Lett.*, 8:450, 2013.
[149] S. Pillai, K. R. Catchpole, T. Trupke, and M. A. Green. Surface plasmon enhanced silicon solar cells. *J. Appl. Phys.*, 101:093105, 2007.
[150] D. Derkacs, S. H. Lim, P. Matheu, W. Mar, and E. T. Yu. Improved performance of amorphous silicon solar cells via scattering from surface plasmon polaritons in nearby metallic nanoparticles. *Appl. Phys. Lett.*, 89:093103, 2006.
[151] V. J. Sorger, R. F. Oulton, and R. M. Ma andX. Zhang. Toward integrated plasmonic circuits. *MRS Bulletin*, 37:728, 2012.
[152] J. A. Dionne and H. A. Atwater. Plasmonics: Metal-worthy method and materials in nanophotonics. *MRS Bulletin*, 37:717, 2012.
[153] N. J. Halas and M. Moskovits. Surface-enhanced raman spectroscopy: Substrates and materials for research and applications. *MRS Bulletin*, 38:607, 2013.
[154] E. Smith and G. Dent. *Modern Raman Spectroscopy: A Practical Approach*. John Wiley and Sons, 2005.
[155] B. Liedberg, C. Nylander, and I. Lundström. Biosensing with surface plasmon resonance - how it all started. *Biosens. Bioelectron.*, 10:i, 1995.
[156] E. Petryayeva and U. J. Krull. Localized surface plasmon resonance: Nanostructures, bioassays and biosensing - a review. *Anal. Chim. Acta*, 706:8, 2011.
[157] E. Della Gaspera, M. Guglielmi, S. Agnoli, G. Granozzi, M. L. Post, V. Bello, G. Mattei, and A. Martucci. Au nanoparticles in nanocrystalline tio2-nio films for spr-based, selective h2s gas sensing. *Chem. Mater.*, 22:3407, 2010.
[158] N. Liu, M. L. Tang, M. Hentschel, H. Giessen, and A. P. Alivisatos. Nanoantenna-enhanced gas sensing in a single tailored nanofocus. *Nat. Mater.*, 10:631, 2011.
[159] J. M. Bingham, J. N. Anker, L. E. Kreno, and R. P. van Duyne. Gas sensing with high-resolution localized surface plasmon resonance spectroscopy. *J. Am. Chem. Soc.*, 132:17358, 2010.
[160] J. B. Wright, K. N. Cicotte, G. Subramania, S. M. Dirk, and I. Brener. Chemoselective gas sensors based on plasmonic nanohole arrays. *Opt. Mater. Exp.*, 2:1655, 2012.
[161] M. A. Noginov, G. Zhu, A. M. Belgrave, R. Bakker, V. M. Shalaev, E. E. Narimanov, S. Stout, E. Herz, T. Suteewong, and U. Wiesner. Demonstration of a spaser-based

nanolaser. *Nature*, 460:1110, 2009.

[162] M. I. Stockman. The spaser as a nanoscale quantum generator and ultrafast amplifier. *J. Opt.*, 12:024004, 2010.

[163] G. Pellegrini, G. Mattei, and P. Mazzoldi. Nanoantenna arrays for large-area emission enhancement. *J. Phys. Chem. C*, 115:24662, 2011.

[164] A. Nevet, N. Berkovitch, A. Hayat, P. Ginzburg, S. Ginzach, O. Sorias, and M. Orenstein. Plasmonic nanoantennas for broad-band enhancement of two-photon emission from semiconductors. *Nano Lett.*, 10:1848, 2010.

[165] A. G. Curto, G. Volpe, T. H. Timiniau, M. P. Kreuzer, R. Quidant, and N. F. van Hulst. Unidirectional emission of a quantum dot coupled to a nanoantenna. *Science*, 329:930, 2010.

[166] S. A. Maier. *Plasmonics: Fundamentals and Applications*. Springer, 2007.

[167] P. B. Johnson and R. W. Christy. Optical constants of the noble metals. *Phys. Rev. B*, 6:4370, 1972.

[168] S. K. Ghosh and T. Pal. Interparticle coupling effect on the surface plasmon resonance of gold nanoparticles: From theory to applications. *Chem. Rev.*, 107:4797, 2007.

[169] F. Bassani and G. P. Parravicini. *Electron States and Optical Transitions in Solids*. Pergamon Press, 1975.

[170] T. W. H. Oates and A. Mücklich. Evolution of plasmon resonances during plasma deposition of silver nanoparticles. *Nanotechnology*, 16:2606, 2005.

[171] H. Ehrenreich and H. R. Philipp. Optical properties of ag and cu. *Phys. Rev.*, 128:1622, 1962.

[172] U. Kreibig and C. v. Fragstein. The limitation of electron mean free path in small silver particles. *Zeitschrift fuer Physik*, 224:307, 1969.

[173] U. Kreibig. Kramers kronig analysis of the optical properties of small silver particles. *Zeitschrift fuer Physik*, 234:307, 1970.

[174] U Kreibig and L. Genzel. Optical absorption of small metallic particles. *Surf. Sci.*, 156:678, 1985.

[175] E. D. Palik. *Handbook of optical constants of solids*. Academic Press, 1997.

[176] G. Mie. Beiträge zur optik trüber medien, speziell kolloidaler metallösungen. *Annalen der Physik*, 3:25, 1908.

[177] V. Bonacic-Koutecky, P. Fantucci, and J. Koutecky. Quantum chemistry of small clusters of elements of groups ia, ib, and iia: fundamental concepts, predictions, and interpretation of experiments. *Chem. Rev.*, 91:1035, 1991.

[178] K. P. Charlé, F. Frank, and W. Schulze. The optical properties of silver microcrystallites in dependence on size and the influence of the matrix environment. *Ber. Bunsenges. Phys. Chem.*, 88:350, 1984.

[179] J. M. Gerárdy and M. Ausloos. Absorption spectrum of clusters of spheres from the general solution of maxwell's equations. iv. proximity, bulk, surface, and shadow effects (in binary clusters). *Phys. Rev. B*, 27:6446, 1983.

[180] T. Härtling, Y. Alaverdyan, A. Hille, M. T. Wenzel, M. Käll, and L. M. Eng. Optically controlled interparticle distance tuning and welding of single gold nanoparticle pairs by photochemical metal deposition. *Opt. Express*, 16:12362, 2008.

[181] J. C. Maxwell Garnett. Colours in metal glasses and in metallic films. *Phil. Trans. R. Soc. Lond. A*, 203:385, 1904.

[182] L. L. Zhao, K. L. Kelly, and G. C. Shatz. The extinction spectra of silver nanoparticle arrays: Influence of array structure on plasmon resonance wavelength and width.

J. Phys. Chem. B, 107:7343, 2003.

[183] Sylgard 184 silicone elastomer datasheet. Technical report, Dow Corning, 2013.

[184] A. Jacab, C. Rosman, Y. Khalavka, J. Becker, A. Tügler, U. Hohenester, and C. Sönnichsen. Highly sensitive plasmonic silver nanorods. *ACS Nano*, 5:6880, 2011.

[185] P. Winsemius. *Temperature dependence of the optical properties of Au and Ag*. PhD thesis, University of Leiden, 1972.

[186] W. Cai, H. Zhong, and L. Zhang. Optical measurements of oxidation behavior of silver nanometer particle within pores of silica host. *J. Appl. Phys.*, 83:1705, 1998.

[187] H. Shiku, T. Saito, C. C. Wu, T. Yasukawa, M. Yokoo, H. Abe, T. Matsue, and H. Yamada. Oxygen permeability of surface-modified poly(dimethylsiloxane) characterized by scanning electrochemical microscopy. *Chem. Lett.*, 35:234, 2006.

[188] H. Over and A. P. Seitsonen. Oxidation of metal surfaces. *Science*, 297:2003, 2002.

[189] C. I. Carlisle, T. Fujimoto, W. S. Sim, and D. A. King. Atomic imaging of the transition between oxygen chemisorption and oxide growth on ag{111}. *Surf. Sci.*, 470:15, 2000.

[190] V. Myroshnychenko, J. Rodríguez-Fernández, I. Pastoriza-Santos, A. M. Funston, C. Novo, P. Mulvaney, L. M. Liz-Marzán, and F. J. García de Abajo. Modelling the optical response of gold nanoparticles. *Chem. Soc. Rev.*, 37:1792, 2008.

[191] K. Chatterjee, S. Banerjee, and D. Chakravorty. Plasmon resonance shifts in oxide-coated silver nanoparticles. *Phys. Rev. B*, 66:085421, 2002.

[192] A. Kuzma, M. Weis, S. Flickyngerova, J. Jakabovic, A. Satka, E. Dobrocka J. Chlpik, J. Cirak, M. Donoval, P. Telek, F. Uherek, and D. Donoval. Influence of surface oxidation on plasmon resonance in monolayer of gold and silver nanoparticles. *J. Appl. Phys.*, 112:103531, 2012.

[193] W. Rechberger, A. Hohenau, A. Leitner, J. R. Krenn, B. Lamprecht, and F. R. Aussenegg. Optical properties of two interacting gold nanoparticles. *Opt. Commun.*, 220:137, 2003.

[194] D. J. Bergman. The dielectric constant of a composite material - a problem in classical physics. *Phys. Rep.*, 9:377, 1978.

[195] B. U. Felderhof and R. B. Jones. Effective dielectric constant of dilute suspensions of spheres. *Phys. Rev. B*, 39:5669, 1989.

[196] D. J. Campbell, K. J. Beckman, C. E. Calderon, P. W. Doolan, R. M. Ottosen, A. B. Ellis, and G. C. Lisensky. Replication and compression of bulk and surface structures with polydimethylsiloxane elastomer. *J. Chem. Ed.*, 75:537, 1999.

[197] A. C. C. Esteves, J. Brokken-Zijp, J. Laven, H. P. Huinink, N. J. W. Reuvers, M. P. Van, and G. de With. Influence of cross-linker concentration on the cross-linking of pdms and the network structures formed. *Polymer*, 50:3955, 2009.

[198] B. Prathab, V. Subramanian, and T. M. Aminabhavi. Molecular dynamics simulations to investigate polymer-polymer and polymer-metal oxide interactions. *Polymer*, 48:409, 2007.

[199] M. Tsige, T. Soddemann, S. B. Rempe, G. S. Grest, J. D. Kress, M. O. Robbins, S. W. Sides, M. J. Stevens, and E. Webb III. Interactions and structure of poly(dimethylsiloxane) at silicon dioxide surfaces: Electronic structure and molecular dynamics studies. *J. Chem. Phys.*, 118:5132, 2003.

[200] J. E. Mark, editor. *Polymer Data Handbook*. Oxford University Press, 1998.

[201] V. Amendola, O. M. Bakr, and F. Stellacci. A study of the surface plasmon resonance of silver nanoparticles by the discrete dipole approximation method: Effect

of shape, size, structure, and assembly. *Plasmonics*, 5:85, 2010.

[202] Y. Kim, J. Zhu, B. Yeom, M. D. Prima, X. Su, J. G. Kim, S. J. Yoo, C. Uher, and N. A. Kotov. Stretchable nanoparticle conductors with self-organized conductive pathways. *Nature*, 500:59, 2013.

[203] R. O. Green, M. L. Eastwood, C. M. Sarture, T. G. Chrien, M. Aronsson, B. J. Chippendale, J. A. Faust, B. E. Pavri, C. J. Chovit, M. Solis, M. R. Olah, and O. Williams. Imaging spectroscopy and the airborne visible/infrared imaging spectrometer (aviris). *Remote Sens. Environ.*, 65:227, 1998.

[204] F. A. Kruse and S. L. Perry. Mineral mapping using simulated worldview-3 short-wave-infrared imagery. *Remote Sens.*, 5:2688, 2013.

List of Publications

As of 20-12-2013

Refereed publications

- C. Ghisleri, F. Borghi, L. Ravagnan, A. Podestá, C. Melis, L. Colombo and P. Milani - Patterning og gold-polydimethylsiloxane (Au-PDMS) nanocomposites by supersonic cluster beam implantation, *J. Phys. D: Appl. Phys.* **47** (2014) 015301.

- C. Ghisleri, M. Siano, L. Ravagnan, M. A. C. Potenza, and P. Milani - Nanocomposite-based stretchable optics, *Laser & Photon. Rev.* **7** (2013) 1020.

- G. Corbelli, C. Ghisleri, M. Marelli, P. Milani and L. Ravagnan - Highly Deformable Nanostructured Elastomeric Electrodes With Improving Conductivity Upon Cyclical Stretching, *Adv. Mater.* **23** (2011) 4504.

- M. Marelli, G. Divitini, C. Collini, L. Ravagnan, G. Corbelli, C. Ghisleri, A. Gianfelice, C. Lenardi, P. Milani and L. Lorenzelli - Flexible and biocompatible microelectrode arrays fabricated by supersonic cluster beam deposition on SU-8, *J. Micromech. Microeng.* **21** (2011) 045013.

Conference proceedings

- G. Corbelli, C. Ghisleri, P. Milani and L. Ravagnan - Supersonic Cluster Beam Implantation: a novel process for biocompatible and stretchable metallization of elastomers, *NanotecIT newsletter* **177** (2012) 31.

Publications under review

- C. Ghisleri, M. A. C. Potenza, L. Ravagnan, A. Bellacicca and P. Milani - Stretchable grating based spectrophotometer, *submitted to Appl. Phys. Lett.* (2013).

Publications in preparation

- C. Ghisleri, M. Ghioni, L. Ravagnan and P. Milani - Surface Plasmon Resonance of metal-polymer nanocomposites synthesized with Supersonic Cluster Beam Implantation.

- C. Ghisleri, F. Borghi, L. Ravagnan, A. Podestá, C. Melis, L. Colombo and P. Milani - Mechanical properties of metal-polymer nanocomposites synthesized by Supersonic Cluster Beam Implantation.

Oral contributions to conferences and workshops

- Supersonic cluster beam implantation: a novel approach for the fabrication of highly stretchable and patternable elastomeric electrodes. - EuroEAP, Dübendorf (CH) - 25th-26th June 2013.
- Nanocomposite based stretchable optics - 6th International Workshop on Polymer / Metal Nanocomposites, Toulouse (FR) - 16th-18th September 2013.
- Supersonic Cluster Beam Implantation: a novel approach for producing metal-polymer nanocomposites based microcircuits for stretchable biomedical devices. - Joint Workshop COST Actions MP1005 MP0903, S. Margherita Ligure (IT) - 7th-8th October 2013 - Invited oral presentation.

Poster presented in conferences and workshops

- Synthesis of soft metal-polymer nanocomposites for biomedical devices - Swiss Nanoconvention 2012, Lausanne (CH) - 22nd-24th May 2012.
- Synthesis of soft metal-polymer nanocomposites for biomedical devices - 6th European Summer School of Neuroengineering Massimo Grattarola, Genova (IT) - 11th-15th June 2012.
- Supersonic cluster beam implantation: a novel approach for the fabrication of highly stretchable and patternable elastomeric electrodes - EuroEAP 2013, Dübendorf (CH) - 25th-26th June 2013.

Participation to Summer Schools

- 6th European Summer School of Neuroengineering Massimo Grattarola, Genova (IT) - 11th-15th June 2012.

Patents submitted

- Method for the production of functionalized elastomeric manufactured articles and manufactured articles thus obtained - Patent number: WO2011121017, Filling date: March 30th, 2011.
- Method for the production of stretchable and deformable optical elements, and elements thus obtained - Patent number: WO2013083624, Filling date: December 5th, 2012.

Acknowledgments

This work can be considered as the end of an entire and important period of my life, projecting me in the real work world. The last three years in particular have been demanding and unforgettable as well. They gave me the possibility to considerably grow both professionally and personally. Only now I realize how many people I worked with, I knew in the last ten years, since the first year of university in the so far 2004, and I have to acknowledge. The main acknowledgement is addressed to Prof. Paolo Milani, who made this PhD thesis possible and greatly supported me since the bachelor thesis. His reproaches and discussions gave me the possibility to meditate and to grow up.

A thanks to all the staff of our group: Marco Potenza, Alessandro Podestá, Paolo Piseri, Cristina Lenardi for their helpful discussions, Claudio Piazzoni who shared with me the troubles during the work in the laboratory, and all the secretaries, in particular Nunzia Tramontano, who born all the boring administrative stuffs. A great thanks to Francesco Cavaliere and, especially, to Daniele Viganó of the Physics Department workshop, who built all the mechanical mounts, stands and sample holders used throughout the entire work. A special thanks to the PhD students and post-docs who helped me to relieve the heavy working days. First of all the new mom Francesca Borghi, with who I s̈haredẗhe tiny desk for the last two years, Massimiliano Galluzzi and Tommaso Santaniello who shared the efforts in the writing the PhD thesis. In these years they became excellent friends other than colleagues. Simone Bovio and Marco Indrieri first wecolmed and introduced me in the community and in this great laboratory during the bachelor thesis: thank you. And at the end a list of all the people I had the privilege to work with (sorry if someone is missing): Luca Puricelli, Luca Bettini, Flavio Della Foglia, Michele Devetta, Carsten Schulte, Yunsong Yan, Gero Bongiorno, Pasquale Scopelliti, Giorgio Bardizza, Tommaso Mazza. A particular acknowledgement for Andrea Bellacicca, arrived in the last half of this work, from who I learnt a lot and who became a good colleague and, mainly, a confidant and friend. All the best for your next three years!

A mention to all the students who made their bachelor or master theses on stretchable electronics and optics, essential for the results of this PhD work: Mattia Marelli, Giulia Pacchioni, Marco Turolla Turati, Marco Milesi, Andrea Barbaglia, Stefano Villa, Giacomo Viganó, Mirko Siano, Alberto Annoni, Matteo Ghioni, Federico Motti.

WISE srl has been an important step of my life in the last years: it allowed me to access the challenging and (for me) new world of entrepreneurship and to open new ways for my future. A huge thanks to Luca Ravagnan, CEO, co-founder, mentor and first person that introduced me to the world of metal-polymer nanocomposites many years ago, fundamental for the results discussed in this PhD work. I also want to gladly

thanks Marta Ferri, Sandro Ferrari, Giulia Salzano and Alessandro Antonini for the hard work they daily perform for the success of our company.

A personal acknowledgement to my best "out-of-the-work" friends: Paolo Ferrari above all for sharing the bike adventures, Roberto Cuozzo and Davide Iannone, who it is always a pleasure to share a pizza and a have a walk in Bergamo with. I also remind an important person who was intermittently next to me in the last six years and I feel I must acknowledge for her patience and comprehension.

Last but not the least a special, huge and unique thanks to my parents. There are no particular motivations, they supported me from all the points of view and gave me the strength to continue even in the most difficult moments. I apologize if sometimes (actually many times) I did not behave respectfully or as expected because of the weariness or stress after a heavy working day.

I keep my last acknowledgement for the person to which I am most grateful both professionally and personally who began with me the work on PDMS metallization, suggested and oriented me during my master thesis and shared with me the successes and the difficulties of the first stages of WISE. You became an excellent friend and I really miss you a lot. Thank you Gabriele.